Propriétés physiques des astéroïdes cibles de la mission spatiale Rosetta, et des petits corps du système solaire externe

Davide Perna

Università degli Studi di Roma Tor Vergata
Facoltà di Scienze MM. FF. NN.
Dottorato di Ricerca in Astronomia (XXII ciclo)

Observatoire de Paris
École Doctorale "Astronomie et Astrophysique d'Ile-de-France"
Doctorat: Astronomie et Astrophysique

Physical properties of asteroid targets of the Rosetta space mission, and of minor bodies of the outer Solar System

Propriétés physiques des astéroïdes cibles de la mission spatiale Rosetta, et des petits corps du Système Solaire externe

PhD thesis presented by
Davide PERNA

Supervisor:
Dr. Elisabetta DOTTO
Supervisor:
Dr. Maria Antonietta BARUCCI
Internal supervisor:
Prof. Roberto BUONANNO
Coordinator:
Prof. Pasquale MAZZOTTA

Evaluation commission members:

Prof. Bruno SICARDY
Prof. Giuseppe BONO
Dr. Giovanni Battista VALSECCHI
Dr. Laurent JORDA
Dr. Elisabetta DOTTO
Dr. Maria Antonietta BARUCCI

8 March 2010
Academic year 2009-2010

If on a winter's night a reader...

Acknowledgements

First of all I would like to thank my supervisors, Roberto Buonanno, Elisabetta Dotto, and Antonella Barucci, who have supported and guided me through these years. I will not be a student anymore, but I will always have to learn from them.

I wish to thank all of the "Planetos" in Meudon, for their expertise, help, and friendship. In particular I have to thank Sonia Fornasier and Marcello Fulchignoni, for their precious collaboration and useful discussions (as well as for their "logistic" help).

Many thanks to all of the friends and colleagues in Rome and Monte Porzio Catone, who accompanied me for a long part of my PhD. I am particularly grateful to Fiore De Luise, for his help, suggestions, and friendship; and to Elisa Nichelli, for her encouragement and to have read a late draft of my thesis (!).

I would like to thank all of the other colleagues and collaborators who made this thesis possible, please don't be angry with me if I do not cite all of you!

I thank my few close friends, they represent a fundamental part of my life, and I felt their nearness even when we have been far away from each other.

Last but not least, a very special thank to my family, who always supported and encouraged me. To my parents Clelia and Valentino, my brother Simone, and my grandparents Giulia and Franco (who both died during my PhD, this thesis is dedicated to them). And I should probably include my kitten Molly, by now she's an important member of the family!

Dankon al ĉiuj vi!

Abstract

The minor bodies of the Solar System are the remnants of the primordial planetesimal population. Their investigation can hence help us to improve our knowledge about the environment conditions in the solar nebula, and to understand the thermal and physical processes that took place in the early phases of the Solar System.

During my PhD, I focused on the physical characterization of the asteroids (2867) Steins and (21) Lutetia, targets of the ESA-Rosetta space mission, and of the minor bodies of the outer Solar System (Centaurs and Trans-Neptunian Objects, TNOs).

The knowledge of the physical properties of asteroids to be visited by spacecrafts is fundamental to optimize the observing procedure during the mission, and to plan specific observations of the most interesting regions of the asteroid surface. Moreover, the comparison of the results obtained from the Earth and those obtained in situ will provide the *ground truth* for standard ground-based investigations of the asteroids which will be never reached by a space mission.

In the framework of my research I hence performed a ground-based investigation of Steins and Lutetia, carrying out visible photometric and spectroscopic observations of these two bodies using the Telescopio Nazionale Galileo (TNG, La Palma, Spain). From the reduction, the analysis, and the interpretation of the obtained data, I improved the physical knowledge of both the objects prior to the Rosetta fly-by.

As for the outer minor bodies, their science is very young (after Pluto, the first object having a trans-Neptunian orbit was found only in 1992), and there is still a lack of fundamental data about them. Nowadays they probably represent the most investigated objects in planetary research, since these minor bodies accreted at large heliocentric distances: they contain the most pristine material presently available for our studies, and preserve records of the processes occurred during the early history of the Solar System.

In this thesis I present the results I obtained as part of a Large Programme performed at the European Southern Observatory (ESO, Chile) on Centaurs and Trans-Neptunian Objects: I carried out four of the several observing runs, I reduced and analysed visible and near-infrared photometric and spectroscopic data, I contributed to the interpretation of the obtained spectra using radiative transfer models, and, in particular, I took in charge the analysis and interpretation of the visible and near-infrared photometric dataset (color indices and light curves). On the basis of the obtained colors, I derived the taxonomic classification of the observed TNOs and Centaurs, and I performed a statistical analysis using also the whole available literature looking for correlations between taxonomy and dynamics. From the interpretation of the light curves I gathered information about the rotation, shape and density of the objects under analysis, and I investigated the density statistics of the small bodies of the outer Solar System combining these new results with literature data.

This thesis is structured in four main chapters.

The first chapter presents an overview of the minor bodies of the Solar System. It deals with their dynamical classification and physical characterization, describing in particular the observing techniques (photometry and reflectance spectroscopy) which have been adopted to develop my PhD research.

The second chapter describes the procedures I adopted to acquire and reduce the visible and near-infrared, photometric and spectroscopic data analysed in the framework of the present work.

In the third chapter I present the results obtained from the investigation of the surface of the asteroid targets of the Rosetta mission, (2867) Steins and (21) Lutetia. For Steins, the information retrieved on its size, shape and rotation are also discussed.

The fourth chapter deals with the results I obtained within the ESO Large Programme on Centaurs and Trans-Neptunian Objects, from the analysis of their spectra, photometric color indices, and light curves.

Keywords: Solar System – Asteroids – Steins – Lutetia – Space mission – Rosetta – Trans-Neptunian Objects – Centaurs – Photometry – Spectroscopy

Résumé

Les petits corps du Système Solaire sont les vestiges des planétésimaux du disque primordial. Leur étude peut donc améliorer notre connaissance des conditions présentes dans la nébuleuse solaire, et des processus thermiques et physiques qui ont eu lieu pendant les premières phases de vie du Système Solaire.

Pendant mon doctorat, je me suis concentré sur la caractérisation physique des astéroïdes (2867) Steins et (21) Lutetia, cibles de la mission spatiale ESA-ROSETTA, et des petits corps du Système Solaire externe : Centaures et Objets transneptuniens (TNOs, acronyme anglais de Trans-Neptunian Objects).

La connaissance des propriétés physiques des astéroïdes qui doivent être visités par des sondes est fondamentale que ce soit pour optimiser la procédure d'observation pendant la mission, ou bien pour planifier des observations spécifiques des régions les plus intéressantes de la surface de l'astéroïde. De plus, la comparaison des résultats obtenus de la Terre et ceux obtenus "in situ", fournira l'étalonnage (*ground truth*) pour les données sol des astéroïdes qui ne seront jamais atteints par une mission spatiale.

J'ai donc effectué des observations photométriques et spectroscopiques dans le domaine du visible de Steins et Lutetia, en utilisant le Telescopio Nazionale Galileo (TNG, La Palma, Espagne). A la suite de la réduction, l'analyse, et l'interprétation des données obtenues, j'ai amélioré la connaissance physique des deux objets avant le survol de Rosetta.

Pour ce qui concerne les petits corps du Système Solaire externe, leur étude est relativement récent (après Pluton, le premier objet ayant une orbite transneptunienne a été trouvé seulement en 1992) et le manque de données fondamentales demeure. De nos jours ils représentent un sujet d'actualité de la recherche planétaire, puisque ces petits corps se sont accretés aux grandes distances héliocentriques : ils contiennent le matériel le plus vierge actuellement disponible pour nos études, et conservent des informations sur les processus qui ont eu lieu pendant la première partie de la vie du Système Solaire.

Dans cette thèse je présente les résultats que j'ai obtenu en partecipant à un programme d'observation conduit à l'Observatoire européen austral (European Southern Observatory, ESO, Chili) sur les Objets transneptuniens et les Centaures : j'ai effectué des observations, j'ai réduit et analysé des données photométriques et spectroscopiques dans les domaines du visible et de l'infrarouge proche, j'ai participé à l'interprétation des spectres obtenus en utilisant des modèles de transfert radiatif et, particulièrement, j'ai pris la responsabilité de l'analyse et l'interprétation de l'ensemble des données photométriques (indices de couleur et courbes de lumière). J'ai obtenu la classification taxonomique des objets observés sur la base des couleurs photométriques, et j'ai fait une analyse statistique utilisant la littérature disponible, à la recherce de corrélations entre la taxonomie et la dynamique. A la suite de l'interprétation des courbes de lumière, j'ai rassemblé des informations sur la rotation, la forme, et la densité des objets analysés, et j'ai etudié la statistique de densité des petits corps du Système Solaire externe en combinant ces nouveaux résultats avec des données de littérature.

Cette thèse est structurée en quatre chapitres principaux. Le premier chapitre présente une vue d'ensemble des petits corps du Système Solaire, avec leur classification dynamique et leur caractérisation physique, décrivant en particulier les techniques d'observation (la photométrie et la spectroscopie de réflectance) utilisées pour développer mes recherches.

Le deuxième chapitre décrit les procédures que j'ai utilisées pour acquérir et réduire les données photométriques et spectroscopiques, dans les domaines du visible et de l'infrarouge proche, analysées dans le cadre mon doctorat.

Dans le troisième chapitre je présente les résultats obtenus de l'étude de la surface des astéroïdes cibles de la mission Rosetta, (2867) Steins et (21) Lutetia. Pour Steins, les informations obtenues sur sa taille, forme, et rotation sont aussi discutées.

Le quatrième chapitre traite avec les résultats que j'ai obtenu sur les Centaures et les Objets transneptuniens, de l'analyse de leurs spectres, indices de couleur, et courbes de lumière.

Mots clés : Système Solaire – Astéroïdes – Steins – Lutetia – Mission spatiale – Rosetta – Objets transneptuniens – Centaures – Photométrie – Spectroscopie

Contents

List of Figures

List of Tables

Chapter 1

The minor bodies of the Solar System

The study of the minor bodies allows us to cast light on the origin and early evolution of the Solar System, since, according to the most generally accepted theory (Safronov 1979), they represent the "vestiges" of the left-over planetesimals from the early accretional phases of the proto-planetary disk. Even though minor bodies have been affected by thermal, dynamical, and collisional evolution, they contain a record of the initial conditions that existed in the solar nebula some 4.6 Gy ago. Thus, interpreting their present-day physical and orbital properties can tell us a lot about the compositional gradient of the nebula and the processes which governed the first phases of the Solar System at different heliocentric distances.

According to the most recent theories, commonly labeled as "Nice model" (Gomes et al. 2005; Morbidelli et al. 2005; Tsiganis et al. 2005), the current distribution of minor bodies is largely due to planetary migration occurred in the early history of the Solar System. Within this model, the four giant planets (Jupiter, Saturn, Uranus and Neptune) were originally found on near-circular orbits between $\sim$ 5.5 and $\sim$ 17 AU. Following the interactions with the planetesimals in a dense disk originally extended from the orbit of the outermost planet to some 35 AU, Saturn, Uranus and Neptune moved outwards, Jupiter moved slightly inward, while the outer primordial disk was almost entirely scattered, losing $\sim$ 99% of its mass and producing the various populations of objects nowadays observable in the Solar System.

Moreover, during their history minor bodies have been subject to different transport mechanisms, as collisions, close approaches (mutual or with planets), and orbital resonances. The latter can lead to either long term stabilization of the orbits or be the cause of their destabilization, and are in general classified as secular resonances and mean motion resonances (e.g.,

Froeschle & Morbidelli 1994; Nesvorný & Morbidelli 1998). A mean motion orbital resonance occurs when two bodies (in this case, the minor body and a giant planet) have periods of revolution that are a simple integer ratio of each other (hereafter I adopt the convention that the p:q resonance denotes the resonance of p orbits of the inner object to q orbits of the outer object). A secular resonance occurs when the precession rate of the perihelion or ascending node of the minor body coincides with that of a giant planet.

Minor planets are divided into "groups" based on their current orbital and physical properties.

1.1 Dynamical classification

- **Trans-Neptunian Objects (TNOs):** after Pluto's discovery, the first object having an orbit that is completely trans-Neptunian was found in September 1992 (Jewitt et al. 1992; Jewitt & Luu 1993). Nowadays more than 1350 Trans-Neptunian Objects are known, and their investigation represents one of the most outstanding topics in contemporary planetary science, since these distant and icy bodies are considered to be the remnants of the planetesimals in the outer Solar System and to retain the most pristine (least altered) material that can presently be observed.

  From a dynamical point of view, they are in turn classified as (Gladman et al. 2008, see Fig. 1.1):

  Resonant objects: they lie in the about twenty identified mean motion resonances with Neptune, the most populated being the 3:2 resonance ($a = 39.4$ AU) which hosts Pluto among other bodies ("Plutinos").

  Scatter(ing/ed) Disk Objects (SDOs): Gladman et al. (2008) consider SDOs as those objects that are *currently* scattering actively off Neptune, without any assumption about their origin. With this nomenclature they exist down to $a = 30$ AU. At very large a (~ 2000 AU), where external influences become important, the inner Oort cloud begins.

  Detached objects: the term "detached", adopted from Delsanti & Jewitt (2006), indicates that these objects are essentially unaffected by the gravitational influence of Neptune, but not so far away that external influences are important to their current dynamics ($a \sim 2000$ AU).

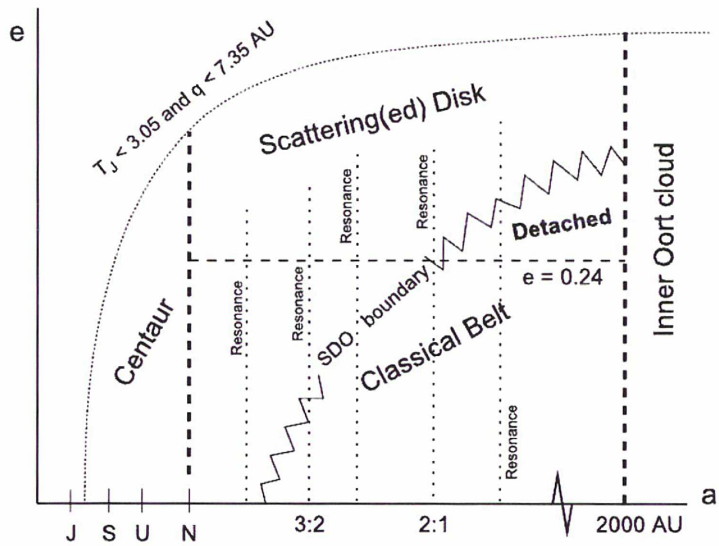

Figure 1.1 – Schematic illustration (not in scale) of the nomenclature for the outer minor bodies. From Gladman et al. (2008).

According to Gladman et al. (2008) they are nonscattering TNOs with large eccentricities ($e > 0.24$).

Classical objects: they are the remaining nonresonant, nonscattering, low-e TNOs. Gladman et al. (2008) divide this *classical belt* into an inner classical belt ($a < 39.4$ AU, nonresonant), an outer classical belt ($a > 48.4$ AU, nonresonant, and $e < 0.24$), and a main classical belt (or Cubewanos, after the first such object that was discovered, 1992 QB_1). Even if the current situation is not sufficiently clear to draw an arbitrary division, as stated by Gladman et al. (2008), many authors refer to two distinct populations in the classical belt based on orbital inclination (Levison & Stern 2001; Brown 2001): dynamically "hot" (high-inclination) objects, and dynamically "cold" (low-inclination) objects. In general, the latter present very red colors while the former have preferentially gray colors (Doressoundiram et al. 2002). On the basis of the fact that largest bodies in the hot population are bigger than those in the cold population, Levison & Stern (2001) suggested that the hot population formed closer to the Sun and was transported outward during the final stages of planet formation. Numerical simulations by Gomes (2003) showed that the hot population could find its origin in the migration of Neptune, which scattered the planetesimals originally

formed inside $\sim$ 30 AU. The current classical belt would hence be the superposition of these bodies with the local population, formed beyond 30 AU, which stayed dynamically cold. Assuming that the maximum size of the objects was a decreasing function of their initial heliocentric distance, this scenario explains why the biggest objects are all in the hot population. Moreover it explains the color difference between hot and cold objects, assuming that the color of bodies in the primordial disk varied with heliocentric distance (Morbidelli et al. 2008).

- **Centaurs:** according to the Minor Planet Center[1] (MPC) definition, a Centaur is an object with semimajor axis less than that of Neptune (30.1 AU) and perihelion distance larger than Jupiter's semimajor axis (5.2 AU). Gladman et al. (2008) classify them as having perihelion $q >$ 7.35 AU (halfway between the orbits of Jupiter and Saturn), semimajor axis less than that of Neptune, and Tisserand parameter[2] $T_J > 3.05$. The intent of this definition is that the evolution of Centaurs is not currently controlled by Jupiter. Objects (60558) Echeclus and (52782) Okyrhoe, defined as Centaurs by the MPC, are accordingly reclassified as Jupiter coupled objects. The orbits of Centaurs are unstable, with lifetimes $\sim 10^6 - 10^7$ years, after which they can be ejected from the Solar System, impact the giant planets, or evolve into Jupiter Family Comets or Near Earth Objects (NEOs) (Horner et al. 2004). Centaurs are widely believed to come from the trans-Neptunian regions (Levison & Duncan 1997; Durda & Stern 2000) and to have been scattered into their present orbits by gravitational instabilities and collisions. Like Trans-Neptunian Objects, Centaurs accreted at low temperature and large solar distances, and must still contain relative pristine material. It has been suggested (e.g., Peixinho et al. 2003; Tegler et al. 2008) the presence of two distinct groups among Centaurs, one very red (Pholus-like) and one with neutral colors (Chiron-like). In this scenario very red Centaurs would have old surfaces, covered by an irradiation mantle, while blue objects might have younger surfaces rejuvenated by collisions and/or cometary-like activity.

- **Satellites of planets:** the *irregular* satellites of the outer planets,

[1] http://www.cfa.harvard.edu/iau/mpc.html

[2] The Tisserand parameter with Jupiter is defined as:

$$T_J = \frac{a_J}{a} + 2\sqrt{\frac{a}{a_J}(1-e^2)}\cos i \tag{1.1}$$

where a, e, i are the orbital semimajor axis, eccentricity, and inclination of the object and a_J is the semimajor axis of Jupiter.

generally orbiting on distant, inclined, eccentric, retrograde orbits, are believed to have been captured from heliocentric orbit during the early Solar System history (e.g., Nicholson et al. 2008). Conversely, *regular* satellites generally follow a close and prograde orbit, with low inclination and eccentricity, and are believed to have formed *in situ* (e.g., Magni et al. 1990). Neptune's satellite Triton represents an important exception, because despite of its close and circular orbit it is widely considered to be a captured body (e.g., Farinella et al. 1980; McKinnon 1991).

- **Trojans:** asteroids that are in a 1:1 mean motion resonance with a planet, around one of the two Lagrangian points of stability, L4 and L5, which lie 60° ahead of and behind the larger body. Until 1990 only Jupiter Trojans were known, with asteroids in the L4 group originally named Greeks, and those at the L5 point named Trojans. Nowadays, we refer to both groups as Trojans, and other than about 3700 Jupiter Trojans, four Mars Trojans and six Neptune Trojans are known.

- **Main Belt Asteroids (MBAs):** most of the $\sim$ 460000 known asteroids orbit the Sun between Mars and Jupiter, within the *main belt* (MB) which extends approximately from 2.06 AU (4:1 resonance with Jupiter) to 3.28 AU (2:1 resonance with Jupiter). In this region the last phases of the accretion of planetesimals into planets during the formative period of the Solar System were prevented by large gravitational perturbations by Jupiter. These perturbations caused too high relative velocities for the planetesimals to form planet-sized bodies. Moreover, strong Jupiter's gravity, through the mechanism of mean motion resonances (3:1, 5:2, 7:3), was responsible for the formation of the *Kirkwood gaps* in the distribution of main belt asteroids with semi-major axis (see Fig. 1.2). Wisdom (1983; 1987) looked for an analytical solution for the effect of resonances, and found chaotic orbits within the 3:1 and 2:1 Jovian mean motion resonances, and quasi-periodic orbits within the 3:2 resonance (where the so-called *Hilda* asteroids lie).

  The MB is widely believed to have suffered a strong collisional evolution, yielding a fragmentation of the original population in smaller and smaller bodies (Farinella et al. 1982). A major outcome of this process is the production of *dynamical families* among asteroids, with the parent body shattered or craterized to create a swarm of smaller asteroids sharing similar orbital elements (a, e, i). Current properties of families have been extensively studied to infer information on the physical processes that were responsible for their formation, and on the physical

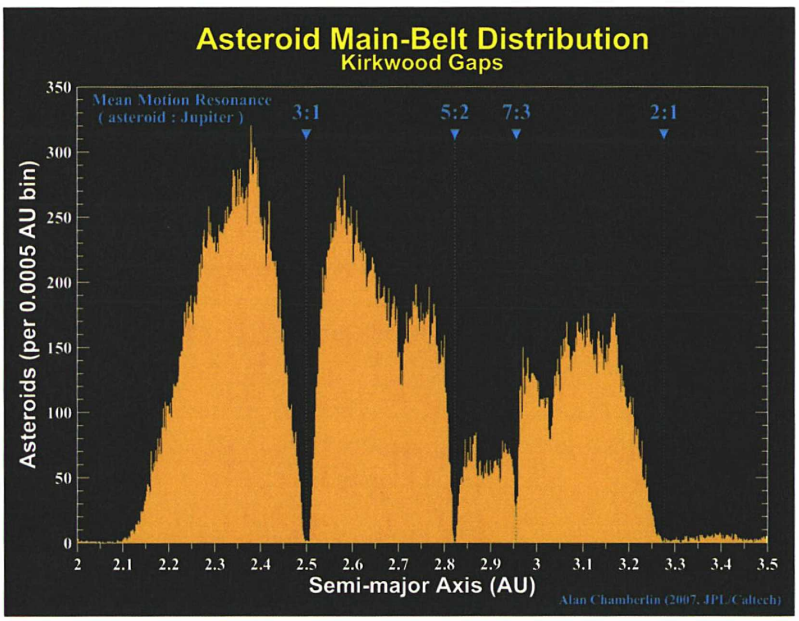

Figure 1.2 – Distribution of semimajor axis for asteroids. This graph was created in June 2007 using all asteroids with "well-determined" orbits (specifically, 156929 numbered asteroids).

properties of their parent bodies. From the current locations of the fragments in proper element space, interpreted in terms of differences in ejection velocities according to the classical Gauss equations, the kinematical properties of family-forming events can be derived (Cellino et al. 1999b). Moreover, spectroscopic investigations of family members can produce possible evidence of thermal differentiation of the original parent body (Cellino et al. 2002).

Recently (Hsieh et al. 2004; Hsieh & Jewitt 2006; Jewitt et al. 2009), the classical distinction between (inert, rocky) asteroids and (active, icy) comets has been complicated significantly with the discovery of the class of Main Belt Comets (MBCs). There are currently four known MBCs (Fig. 1.3), which orbit completely within the main asteroid belt: 133P/Elst-Pizarro, P/2005 U1 (Read), 176P/LINEAR (1999 RE_{70}), and P/2008 R1 (Garradd). Unlike all other comets, which originated in the outer Solar System, MBCs appear to have formed where we see them today. Hence, it is supposed that they have been dormant until very recently (otherwise they would have exhausted their ice supplies long ago), and that their activity has been triggered by impacts excavating buried volatiles. The discovery of MBCs demonstrates that

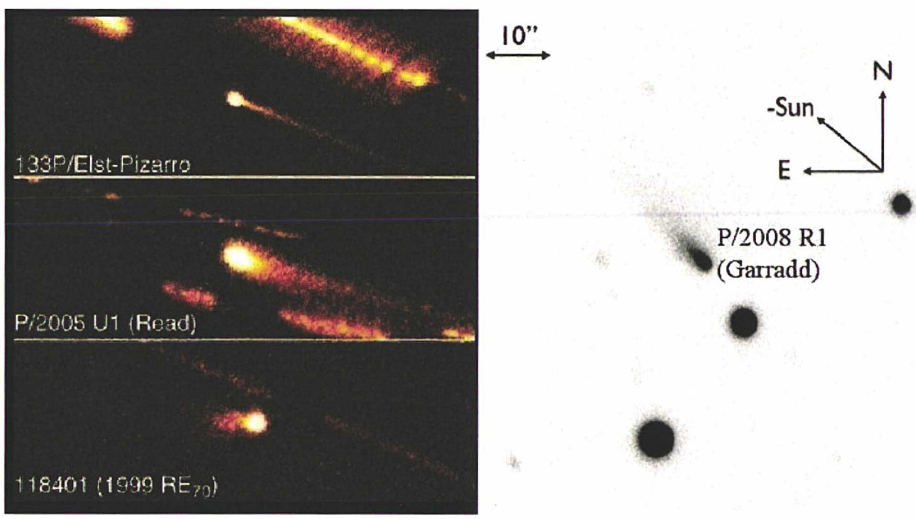

Figure 1.3 – Pictures of the four known MBCs (Hsieh & Jewitt 2006; Jewitt et al. 2009).

ice exists and may be quite common in the MB, and supports the theory that outer main belt could be a likely source of terrestrial water (Morbidelli et al. 2000; Albarède 2009).

- **Near Earth Objects (NEOs):** Near Earth Objects are asteroids (NEAs) and comets (NECs) with perihelion less than 1.3 AU. At the present time more than 6500 NEOs are known, less than 100 being comets (probably coming mostly from Jupiter Family Comets, as suggested by DeMeo & Binzel 2008). Their lifetimes are $\sim 10^6 - 10^8$ years, after which either they impact the Sun or a planet, or are ejected from the Solar System. The NEO population is replenished from particular zones in the main belt, which provide NEOs via powerful and diffusive resonances (Morbidelli et al. 2002).

1.2 Physical characterization and observing techniques

The differences presented by minor bodies at varying distances from the Sun are directly due to the compositional gradient of the primordial nebula with heliocentric distance. In the inner protoplanetary disk, heated by the

Sun, ices and gases could not condense, leaving mainly rocky and metallic minerals. Conversely, in the cold outer disk, ices and gases, as well as silicates and metallic compounds, could condense.

The understanding of the physical (as well as dynamical) properties of the minor body populations can therefore provide crucial information to investigate the structure and the early evolution of the Solar System at different distances from the Sun.

Different observing techniques can be adopted to characterize the physical nature of minor bodies. Among them the most widely used are *photometry* and *reflectance spectroscopy*.

1.2.1 Photometry

Colors: The investigation of photometric colors represents the best technique to study a large number of (eventually faint) objects (e.g., TNOs, see section 4.2). Even if photometric colors cannot provide firm constraints on the surface composition, since they depend also on scattering effects in particulate regoliths and viewing geometry, they nevertheless bring important information and they can be used to classify the observed objects in different groups that reasonably indicate different composition and/or evolutional history. For example, on the basis of photometric colors, taxonomies were firstly created for asteroids a few decades ago, and recently also for Centaurs and TNOs (see sections 1.3.1 and 1.4.1).

Phase curves: Bowell et al. (1989) have found a relationship (*phase curve*) between the observed magnitude of asteroids and the phase angle α, which can be written as:

$$H(\alpha) = H - 2.5log[(1-G)\varphi_1(\alpha) + G\varphi_2(\alpha)] \tag{1.2}$$

where

- $H(\alpha)$ is the asteroid's V magnitude reduced to unit heliocentric (r) and geocentric (Δ) distances, $H(\alpha) = V - 5log(r\Delta)$, function of the phase angle of observation;
- H is the *absolute magnitude*, i.e. at $\alpha = 0°$;
- G is the angular coefficient of the phase curve, the so-called *slope parameter*;

- $\varphi_1(\alpha)$ and $\varphi_2(\alpha)$ are two functions of α defined as:

$$\varphi_1(\alpha) = exp\Big[-3.33\Big(tan\frac{\alpha}{2}\Big)^{0.63}\Big] \tag{1.3}$$

$$\varphi_2(\alpha) = exp\Big[-1.87\Big(tan\frac{\alpha}{2}\Big)^{1.22}\Big] \tag{1.4}$$

Absolute magnitude H and slope parameter G represent two very important photometric parameters, which can be determined by:

$$H = -2.5log(a_1 + a_2) \tag{1.5}$$

$$G = \frac{a_1}{(a_1 + a_2)} \tag{1.6}$$

where a_1 and a_2 are two auxiliary variables, constant for each asteroid, which can be set with a least squares fit of $H(\alpha)$ and α to the relation:

$$H(\alpha) = -2.5\log[a_1\varphi_1(\alpha) + a_2\varphi_2(\alpha)] \tag{1.7}$$

Slope parameter G relates to the surface's albedo (Tedesco 1989; more recently, Carvano 2008), which is in turn related to the so-called *opposition effect*, a surge in brightness observed when the object is near opposition. The amplitude and width of opposition effect depend on surface albedo in a non-monotonic way with maximum for the moderate albedo bodies which is impossible to explain neither by coherent-backscatter effect (a preferential tendency for light scattered along conjugate paths in the regolith to constructively interfere at small phase angles) nor shadow-hiding effect (regolith particles progressively occult their own shadows as the phase angle decreases to zero) alone. Attempts to derive a physically motivated photometric model that incorporates both these effects, so far have not yielded a widely accepted model (Belskaya & Shevchenko 1999; Shkuratov & Helfenstein 2001).

From the absolute magnitude, once also the geometric (visual) albedo p_v is known, an estimation of the object's diameter D is possible, through the relation (Tedesco et al. 1992):

$$D = \frac{1329 \times 10^{-H/5}}{\sqrt{p_v}} \tag{1.8}$$

Light curves: A very powerful tool for retrieving information about the minor bodies is the analysis of their photometric light curves, which are

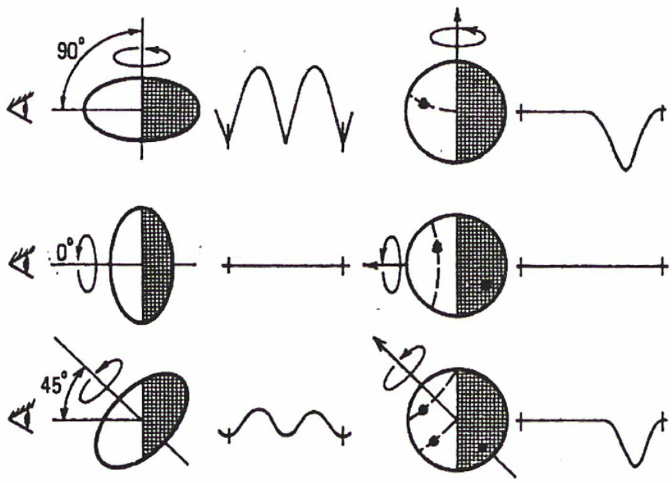

Figure 1.4 – Examples of body profiles with corresponding light curves.

functions of the rotational period, spin axis orientation, shape, and large-scale surface structure of the observed objects (Fig. 1.4).

To retrieve the rotational periods of the investigated bodies, in this work I followed the method developed by Harris et al. (1989a), performing a Fourier analysis of the *composite* (i.e. combining data from different observing nights) light curves. These latter are described as:

$$V(\alpha, t) = \overline{V}(\alpha) + \sum_{k=1}^{n} \left[A_k \sin \frac{2\pi k}{P}(t - t_0) + B_k \cos \frac{2\pi k}{P}(t - t_0) \right] \qquad (1.9)$$

where

- $V(\alpha, t)$ is the computed reduced magnitude at phase angle α and time t;
- $\overline{V}(\alpha)$ is the mean magnitude at phase angle α;
- A_k and B_k are Fourier coefficients;
- P is the rotational period;
- t_0 is a zero-point time, chosen near the middle of the time span of the observations.

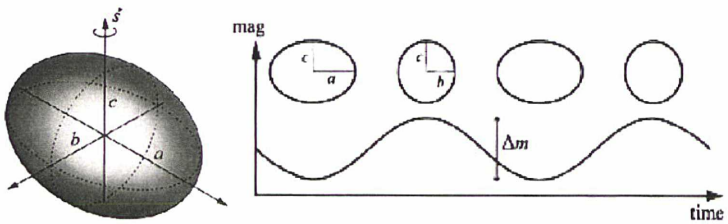

Figure 1.5 – Light curve produced by a triaxial ellipsoid.

A least squares fit of the data to the function 1.9 is performed to find the rotational period which minimizes the errors. Of course, the above procedure works only for short-arc solutions, spanning only a few days. Differently, errors due to uncertainty of the period and changing structure of the light curve (because of different viewing geometry of the observations) could be significant.

Assuming that the observed light curve amplitudes are due only to the bodies' shapes, with negligible albedo variations on their surfaces, a lower limit to the axis ratio a/b comes from the relation:

$$\Delta V = 2.5 \log \left(\frac{a}{b} \right) \tag{1.10}$$

where ΔV is the maximum light curve amplitude (reached in equatorial view, i.e., at an aspect angle $\xi = 90°$) produced by a triaxial ellipsoid with axes $a > b > c$ rotating about the c axis (Fig. 1.5; e.g., Binzel et al. 1989).

1.2.2 Reflectance spectroscopy

Visible and near-infrared (NIR) spectroscopy constitutes the most sensitive and broadly applied technique for characterizing the surfaces of the minor bodies. At these wavelengths thermal emission from the surface is negligible (except low-albedo NEOs which are warm enough to emit detectable thermal flux at 2.5 μm, see Rivkin et al. 2005), while reflected sunlight presents absorption features due to the interaction between incident photons and the surface materials, via electronic and vibrational transitions which are diagnostic of specific mineral or molecular species. The spectral parameters (e.g., band position, depth, shape) of these absorption features are related to the specific composition of the individual material. Nevertheless, the interpretation of the observed reflectance spectra is far from being unambiguous, since spectral features of the different materials combine in a nonlinear way. Hence the most straightforward way to indentify materials on minor bodies'

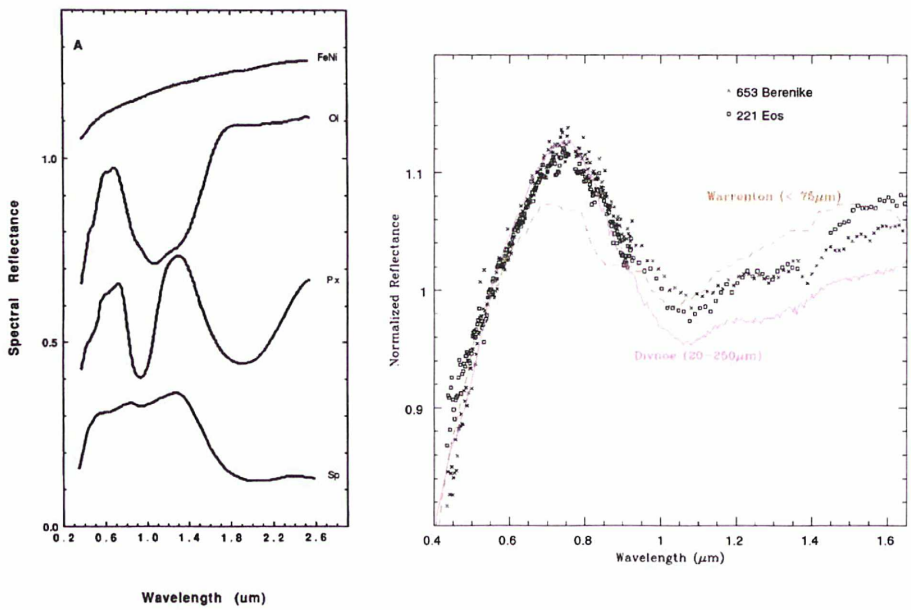

Figure 1.6 – *(left)* Reflectance spectra of several minerals which are important for asteroid spectra interpretation: olivine (Ol), pyroxene (Px), iron-nichel metal (FeNi), spinel (Sp). From Gaffey et al. (1993). *(right)* Reflectance spectra of (221) Eos (squares) and (653) Berenike (crosses) versus spectra of the CO3 chondrite Warrenton and the anomalous stone Divnoe. In parenthesis it is indicated the grain size of the sample. From Mothé-Diniz & Carvano (2005).

surfaces is by comparison with laboratory spectra of meteorites, minerals and ices (Fig. 1.6). In particular, rather than the overall spectrum, it is important to well fit those spectral parameters that are diagnostic of the presence and composition of particular mineral species. For example, the wavelength positions of the 1 and 2 μm features in pyroxene spectra are a function of the Ca and Fe contents of the individual mineral samples, while the ratio of 2 μm band area to 1 μm band area in olivine-orthopyroxene mixtures is directly related to the ratio of pyroxene to olivine abundances (e.g., Gaffey et al. 2002).

Starting from this, a more detailed picture of the surface compositions can be obtained with *spectral modeling*, i.e. calculating synthetic spectra based on radiative transfer formulations and laboratory measurements of optical constants (Fig. 1.7).

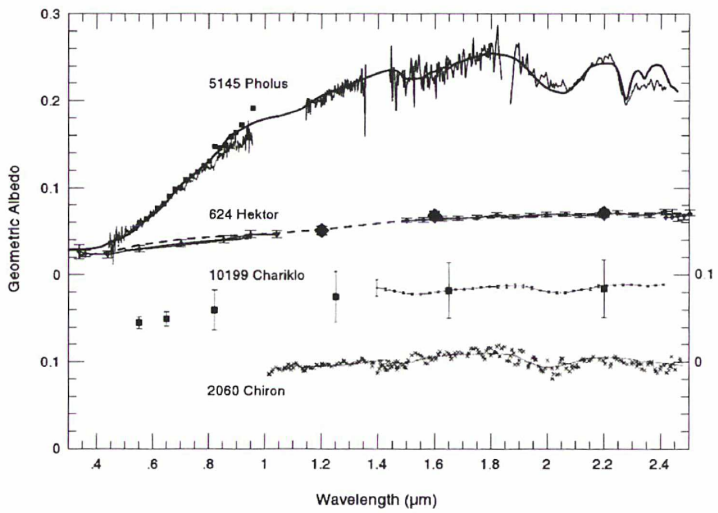

Figure 1.7 – Reflectance spectra of three Centaurs and Jupiter Trojan (624) Hektor, with superimposed models. For example, the model for (2060) Chiron consists of H_2O ice and olivine. All three Centaurs show the prominent 2 μm H_2O ice band, with also indications of the weaker 1.5 μm band. There is no spectral evidence for ice on Hektor. For Chiron the scaling to geometric albedo is approximate, the ordinate for the spectrum of (10199) Chariklo is given on the right side of the figure, while the ordinate for both Hektor and (5145) Pholus is given on the left side of the figure. From Barucci et al. (2002) and references therein.

The optical constants of a material are the real and imaginary components of the complex refractive index, $\tilde{n} = n + ik$, which describes the interaction of electromagnetic radiation with that material. In this representation, n is the "real" index of refraction, and k is the extinction coefficient, which describes the damping of an electromagnetic wave in the material. Both n and k are wavelength dependent. As electromagnetic radiation passes through the material, some fraction is absorbed per unit distance it travels, according to the Beer-Lambert law, which allows the calculation of the absorption coefficient α. If λ is the (vacuum) wavelength of the electromagnetic radiation of interest, then the imaginary index is $k = \lambda\alpha/4\pi$.

For atmosphereless bodies, the two major points of the theory of radiative transfer are solving the integral equation and developing a statistical representation of the regolith individual particles to relate particle properties to scatterer properties. The integral equation and statistical approaches are generally combined to perform spectral modelings of particulate regolith

surfaces. The local mean properties of scattering and absorption are determined by the statistical method, while the integral equation method gives the bidirectional reflectance of a medium composed of such particles. Such a combined technique allows the measured brightness to be related to the microscopic quantities.

The two major theories which are used to model minor bodies' surfaces have been developed by Hapke (1981, 1993) and Shkuratov et al. (1999). Through them it is possible to determine the reflectance spectra or the albedo of a medium from individual physical properties of the different chemical components (with known optical constants). The main differences between the approaches of Shkuratov and Hapke are the treatment of the phase function (which is calculated rather than assigned as an explicit parameter, respectively) and the number of free input parameters (relative amounts, grain size and optical constants of the selected components in Shkuratov, much more in Hapke). Both formulations allow mixing of materials in a variety of ways that include molecular as well as intimate mixtures. Molecular mixtures consist of inclusions in a medium of contaminant particles. Intimate mixtures are the so-called "salt and pepper" mixtures.

A comparison between Hapke and Shkuratov models can be found in Poulet et al. (2002).

1.2.2.1 Aqueous alteration

"Aqueous alteration" is a chemical alteration of a material by the interaction of that material with liquid water. Its action has been inferred for many asteroids, especially in the middle main belt, based on reflectance spectroscopy which shows absorption features (mainly in the 0.4-0.9 and 2.4-3.6 μm regions) diagnostic of or associated with hydrated minerals (for a review, see Rivkin et al. 2002).

Aqueous alteration in asteroids is supposed to be connected to some early heating event either due to the decay of ^{26}Al, a now extinct short-lived isotope, or to electrical induction heating due to a strong early (T-Tauri phase) solar wind (Jones et al. 1990), and hydrated silicates (*phyllosilicates*) can be used as very sensitive tracers of thermal history (Hiroi et al. 1996). In addition to altering olivine and pyroxene to form hydrated silicates (e.g. serpentine), the aqueous alteration process produces oxidized Fe that has absorption bands in the visible and UV spectral regions. Moderate subsequent heating can alter the depth or eliminate some or all of these bands. Hence the study of hydrated minerals on asteroids, and of their distribution with heliocentric distance, provides insight on important issues as the homogeneity of the solar nebula, the heat sources present, and how much mixing

of planetesimals occurred.

Studies of dark, volatile-rich asteroids with orbits beyond 3.5 AU have shown that only a few of them contain in their spectra features typical of aqueous alteration (Rivkin et al. 2002). The prevalent explanation is that induction heating is much less efficient further away from the Sun (e.g., Jones et al. 1990). If this interpretation is correct, aqueous alteration would not be expected for TNOs. One should note, however, that Cruikshank et al. (2001) have suggested that the lack of hydration features in asteroid spectra at large distances from the Sun might be due instead to an increasing amount of spectrally opaque material on their surfaces.

Actually, some features detected in the visible spectra of some TNOs have been interpreted in terms of the presence of aqueously altered minerals on their surfaces (de Bergh et al. 2004; Fornasier et al. 2009). How aqueous alteration processes could have occurred in the outer solar System is not well understood, and it is also possible that some hydrated minerals formed directly in the solar nebula. Large TNOs may have been subjected to significant radiogenic heating (Luu & Jewitt 2002), but it remains to be seen if this would have been sufficient for aqueous alteration of the anhydrous material inside the TNOs, and also a mechanism capable of transporting enough heat to the surface would be required. Another way to heat a TNO is by impacts, which could have provided a transient heat source. However, the heat generated and the duration of the heating episode(s) may not have been sufficient for aqueous alteration of minerals (e.g., Kerridge & Bunch 1979).

1.2.2.2 Space weathering

Solar radiation, cosmic rays, and micro-impacts are inferred to alter the surface of atmosphereless bodies and progressively to change their reflectance spectra. "Space weathering" was first studied for the Moon, since lunar soils returned from Apollo missions have optical properties that differ significantly from those of pristine lunar rocks (Conel & Nash 1970). After that, time-related space weathering processes have often been invoked to interpret spectra of Solar System atmosphereless bodies.

In the laboratory it is possible to reproduce space weathering processes on relevant materials (analogues), such as silicates, ices, and carbons, and in a few cases on materials directly coming from space, i.e. meteorites, interplanetary dust particles (IDPs), and grains collected on Earth or from sample return missions. Solar wind and cosmic ion irradiation can be correctly simulated by keV-MeV ion irradiation, while micro-meteorite bombardment can be simulated by impact experiments (Brunetto 2009).

The effects of space weathering are different according to the heliocentric

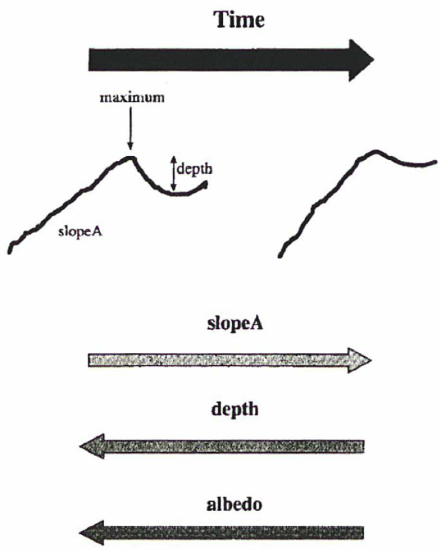

Figure 1.8 – Behavior of space weathering and spectral parameters. From Doressoundiram et al. (1998).

distances of the bodies and their surface composition. In the inner Solar System, silicate surfaces grow darker in time, while their reflectance becomes redder than the spectra of their constituting rocks (Fig. 1.8), as suggested by many authors (e.g., Doressoundiram et al. 1998; Chapman 2004), and confirmed by recent laboratory experiments on ordinary chondrites and silicates, irradiated with heavy ions at keV energies (Strazzulla et al. 2005; Brunetto & Strazzulla 2005).

As an example of how the knowledge of the mechanisms which determine surface evolution can help the interpretation of asteroids' observations, Binzel et al. (2004) invoked space weathering processes to explain the trend of the spectral slopes of NEOs as a function of size. These authors noticed that the visible spectral slope of NEOs have a high dispersion for the smallest objects, and are less dispersed for larger sizes. A possible cause of that could be the effect of space weathering processes: since smaller NEOs have shorter collisional lifetimes than larger ones, they could have younger (less reddened) surfaces, which explains why the dispersion of spectral slopes among them can be expected to be higher than among larger NEOs.

In the outer Solar System cosmic rays should lead to the selective loss of hydrogen in surface materials, and promote the formation of chemically complex polymers, many of which are dark in colour and spectrally red, due to their high carbon abundance (e.g., Andronico et al. 1987). Natural bitu-

mens (e.g. asphaltite, kerite) appear to be reasonably good reference analogs for refractory extraterrestrial organic matter, in terms of spectral properties and chemical structure, especially for TNOs and comets. Their visible and near-infrared spectra flatten after ion irradiation (Moroz et al. 2004). The same weathering process on originally low absorbing ices induces color variations that can reproduce the observed spectral variety of outer Solar System objects (Brunetto et al. 2006). The obtained organic refractories are generally characterized by low albedo and red spectral slope. Thus, the space weathering color trend is not yet well established, due to a strong dependence on the unknown original composition.

1.3 Inner Solar System: up to Jupiter

In the Inner Solar System we find asteroids belonging to different populations: NEAs, MBAs, Jupiter Trojans. As already said, their surfaces mainly present rocky and metallic non-volatile minerals.

1.3.1 Taxonomy

From the seventies of last century, many authors tried to define taxonomic schemes based on observational properties (spectrum, colors, albedo, etc.) of the asteroids. The common intent of these taxonomies is to group asteroids in different classes which are thought to correspond to similar surface composition and/or thermal evolution. It is worth noting that, while the membership to different classes is probably a sign of a substantial difference in the composition, the opposite is not necessarily true, as two bodies belonging to the same taxon may not have the same mineralogical composition. Nevertheless groups' members are supposed to be composed by a limited number of "assemblages".

A very robust taxonomy is that proposed by Tholen (1984, 1989) based on broad band spectrophotometric colors obtained during the Eight-Color Asteroid Survey (ECAS, Zellner et al. 1985), which observed 589 asteroids in the wavelength range 0.3 - 1.1 μm. Tholen identified 14 classes, each denoted by a single letter. In addition to the two "classical", already recognized classes (Chapman et al. 1975), the C (carbonaceous) and S (silicaceous) types, Tholen identified six other spectrally distinct groups of objects, labeling them A, B, D, F, G, and T. Three further classes, labeled as E, M, and P, had featureless ECAS spectra and could only be separated based on their albedos (Barucci et al. 1987 were the first to consider the albedo as a parameter for the classification, in addition to ECAS colors, adding more physical

interpretation to their taxonomic scheme). A generic X-class designation was assigned whenever albedo information was not available for objects belonging to these spectral classes (Tholen 1989). Three asteroids did not fall into any of the above classes and were assigned unique designations: Apollo (Q-type), Dembowska (R-type), and Vesta (V-type). When the classification was uncertain, multiple letter designations were assigned.

A most recent classification is the taxonomy based on the second phase of the Small Main-Belt Asteroid Spectroscopic Survey (SMASSII, Bus & Binzel 2002b,a), which defines 26 different classes attempting to keep to the Tholen taxonomy as much as possible. Three major groupings (the S-, C-, and X-complexes) are introduced, as well as a new L-class. Asteroids with intermediate spectral characteristics are assigned multiletter designations. In 2009, the Bus & Binzel taxonomy has been extended to consider also near-infrared data by DeMeo et al. (2009a).

As discussed above, the taxonomic classification is not directly based on composition or mineralogy. Nevertheless, the members of the same taxon have similar spectra and hence would present a limited suite of constituents. Table 1.1 reports the inferred associations of each Tholen taxonomic class with different mineral assemblages.

Gradie et al. (1989) showed that the distribution of the asteroid taxonomic classes is a function of heliocentric distance. For example, the silicaceous, volatile-poor S-types dominate the inner main belt; low-albedo, carbonaceous C-types are concentrated in the middle/outer main belt; dark, ultra-carbonaceous, volatile-rich D-types are more abundant at larger distances from the Sun (Fig. 1.9). This suggests that a compositional gradient was present in the solar nebula, and that asteroid surfaces have undergone different degrees of thermal processing, in function of their heliocentric distance.

This guess is strengthened by the many associations that have been established (on the basis of their spectra and albedos) between different asteroid taxonomic classes and petrologic types of meteorites.

1.3.2 Relationships among asteroids and meteorites

Meteorites belonging to the same compositional group are believed to come from the same parent body or several similar parent bodies, and meteorite analogues have been assessed for different asteroid taxonomic classes (Table 1.1). Different thermal histories are supposed to have produced the different petrologic types (Fig. 1.10): ordinary chondrites (similar to Q-type asteroids) have undergone modest thermal evolution over the age of the So-

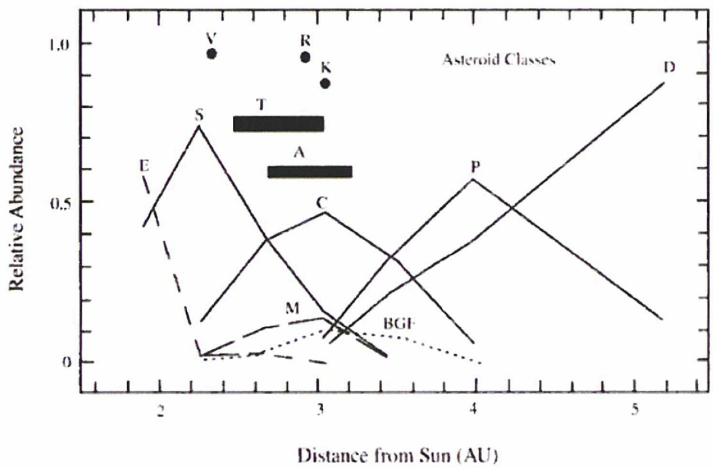

Figure 1.9 – The distribution of classes in the asteroid belt. From Bell et al. (1989).

lar System, while carbonaceous chondrites (similar to C-type asteroids) are inferred to be more primitive. In some cases a strong relation has been found between a group of meteorites and a specific object candidate to be the parent body. For example, from dynamical and spectroscopic constraints, it has been suggested that (6) Hebe may be a significant source of the ordinary chondrites (Migliorini et al. 1997; Gaffey & Gilbert 1998).

Nevertheless, the link between asteroids and meteorite types is not completely understood. It has been noticed that there is a significantly greater apparent mineralogical diversity among asteroids than among meteorites (Gaffey 1999), hence meteorites would be an incomplete sample of the mineralogy present among asteroids. Also the study of the cosmic ray exposure ages of meteorites indicates the presence of discrete groups at different ages (Perron & Zanda 2005). This seems to suggest that the delivery of meteorites is not a continuous flux: it should be due to a few events and would be drawn by some selection effects, e.g. the proximity of the parent body to a chaotic zone in the asteroid main belt and/or the structure and nature of the parent body itself.

A problem known as the "S-type conundrum" has persisted for nearly two decades, but nowadays appears to have found a solution. Stated very simply, the conundrum is that 80% of all meteorites that fall to Earth are ordinary chondrites, whose spectral analogues (Q-type objects) are instead quite rare among the asteroids. Binzel et al. (1996) suggested a possible solution of this conundrum. They showed that NEOs have spectral features which span

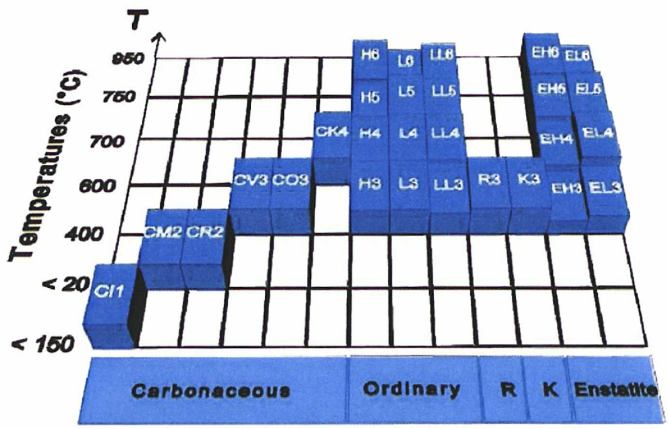

Figure 1.10 – Chondrite meteorites classification as a function of the estimated temperature required for producing the petrologic types. R and K on the bottom indicate Rumuruti and Kakangari, respectively. The level of each box in the third dimension gives the relative proportions of the various types for each chondrite group.

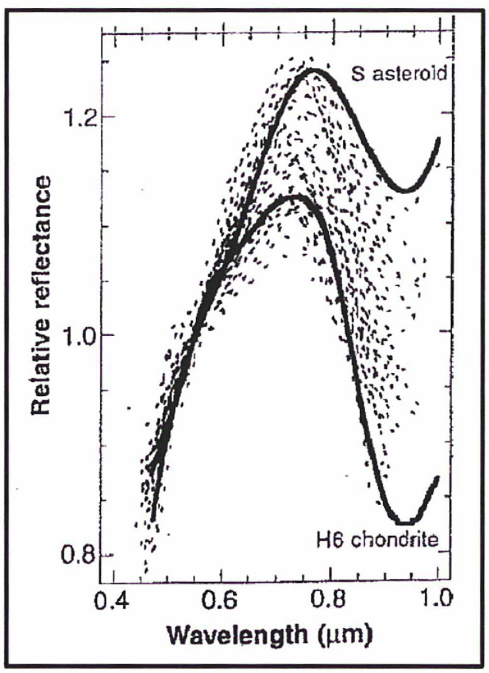

Figure 1.11 – Reflectance spectra of NEOs fill the interval between those of main belt S-types and ordinary chondrites. From Binzel et al. (1996).

Table 1.1 – Mineral assemblages and meteorite analogues inferred for each asteroid taxonomic type.

Tax. type	Minerals	Possible meteorite analogues
A	Olivine, Fe-Ni	Olivine achondrites, pallasites, olivine-metal partial melt residues
V	Pyroxene, feldspar	Basaltic achondrites (eucrites, howardites, diogenites)
R	Olivine, orthopyroxene	Olivine-pyroxene cumulates, olivine-pyroxene partial melt residues
E	Enstatite (Fe-free pyroxene)	Enstatite achondrites (aubrites), Fe-bearing enstatites, Fe-bearing aubrites
M	Fe-Ni, enstatite	Iron meteorites, enstatite chondrites
S	Fe-Ni, olivine, pyroxene	Pallasites, olivine-dominated stony-iron, ordinary chondrites
Q	Olivine, pyroxene, Fe-Ni	Ordinary chondrites
C, B, G, F	Fe-bearing hydrated silicates, C	Carbonaceous chondrites
P	Anhydrous silicates, organics	none
D	Organics, anhydrous silicates	none
T	?	?

the range between the domains of ordinary chondrite meteorites and the most common S-type MBAs (Fig 1.11). They concluded that this range could arise through a diversity of mineralogies and regolith particle sizes, as well as through a time-dependent surface alteration mechanism (space weathering, see section 1.2.2.2). In this last case, asteroids most closely resembling ordinary chondrite meteorites would be those with the youngest surfaces.

1.3.3 Asteroids seen by space missions

To date several asteroids have been investigated by space missions. *In situ* study of asteroids provided critical information unavailable from ground-based observations, and gave us a big improvement to our knowledge about the nature of these bodies.

Visited objects have been studied in detail, obtaining data about their size, shape, rotation, and surface properties. Fly-bys can also give us the asteroid mass, with a subsequent determination of the mean density after a reliable estimate of volume. All of this information can lead to important hints about the physics of the investigated body, and the comparison with ground-based observations can provide the *ground truth* for studies of the asteroids which will be never visited by a space mission.

On October 1991 the Galileo spacecraft, during its travel towards Jupiter, carried out the first ever fly-by of an asteroid, (951) Gaspra (Fig. 1.12, left).

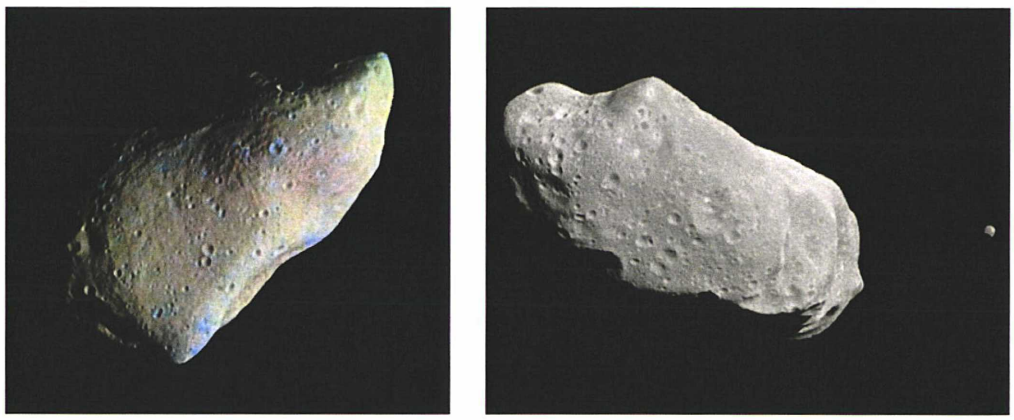

Figure 1.12 – *(letf)* Asteroid (951) Gaspra in a mosaic of two images taken by the Galileo spacecraft from a range of 5300 km, some 10 minutes before closest approach on October 29, 1991. *(right)* Asteroid (243) Ida and its moon Dactyl, the first discovered orbiting an asteroid. From http://solarsystem.nasa.gov.

Gaspra resulted to be a higly irregular, cratered body with principal diameters of 18.2 x 10.5 x 8.9 km. Flat surfaces, ridges, and prominent grooves suggested that this asteroid has a monolithic structure (Stooke 1996). Albedo and color variations observed in correlation with morphological features suggested that Gaspra is covered with a thin regolith which has migrated downslope in some areas (Belton et al. 1992). The low rate and size distribution of impact craters allowed an estimation of the surface age of only 200 million years, possibly suggesting a recent break-up event for the birth of this asteroid (Chapman et al. 1996).

On August 1993, Galileo encountered a second MBA, (243) Ida (with dimensions of 56 x 24 x 21 km). Especially noteworthy was the discovery of a small ($\sim$ 1 km) natural satellite, Dactyl, in orbit around Ida at a distance of $\sim$ 100 km (Fig. 1.12, right). This represented the first observation of a binary system among asteroids. Ida presents a high craterized surface, with an estimated upper limit for the age of $\sim$ 1 Gyr (Belton et al. 1996), while the age of Dactyl should be in the 100-200 Myr range. Moreover, Dactyl's collisional disruption lifetime is very short compared with Ida's age, hence it must be a re-accumulated satellite from previous ejecta (Davis et al. 1996).

Both Gaspra and Ida are S-type asteroids.

On June 1997, the NEAR (Near Earth Asteroid Rendezvous, later renamed Shoemaker) spacecraft flew-by the more primitive C-type MBA (253) Mathilde. Its mass was well determined, with a resulting value of 1.033 $\pm$

0.044×10^{20} g (Yeomans et al. 1997). Coupled with a volume estimate from the imaging data, this value yielded a bulk density for Mathilde of only 1.3 g/cm^3, probably indicating a "rubble pile" structure for this asteroid. Nevertheless structures as a 20-km long scarp (on a body of diameter $\sim$ 53 km) and polygonal craters indicate that Mathilde is not completely strengthless (Cheng 2004).

On February 2000, NEAR Shoemaker was placed in orbit around (433) Eros, the main target of the mission. For the first time ever a "rendezvous" mission with a minor body was performed. Eros is a S-type NEA with an elongated shape (33 x 13 x 13 km). Collected images showed a high quantity of boulders and big craters, but only a few of small craters. A possible explanation is that the small size and low gravity of Eros may result in redistribution or loss of ejecta due to seismic shaking, thus preferentially destroying small craters formed in such regolith (Chapman et al. 2002). On 12 February 2001 the mission was ended with a controlled descent on Eros. Data with the X-ray/Gamma-Ray Spectrometer (XGRS) were collected, to study the surface composition. It resulted that low aluminum abundances for all regions argue against global differentiation of Eros. From element abundances it has been derived a relatively primitive, chondritic composition, with possible signatures of limited partial melting or impact volatilization (Trombka et al. 2000).

Hayabusa (formerly known as MUSES-C), the first sample return mission from an asteroid, reached on September 2005 its target, the NEA (25143) Itokawa (Fig 1.13). After a complete topographic and spectroscopic analysis of the surface, in November 2005 it landed on the asteroid and attempted to collect samples. Because of some technical problems, it is not sure if the collection of material in the storage capsule succeeded. The spacecraft is scheduled to return to Earth by June 2010. Nevertheless, in situ analysis already brought many results. Itokawa appears to be a contact binary *rubble pile* asteroid, with a lack of impact craters. Its surface is divided in two parts: the first, rough and characterized by boulders; the second, smooth and covered by regolith. A minimum in the gravitational potential has been observed in correspondence of the limit between these two parts. It has been suggested a correlation between this minimum and the high quantity of regolith present in this region, caused either by seismic movements due to impacts or by gravitational effects induced by the close passages to the Earth (Fujiwara et al. 2006, and references therein). Some color difference is present over the surface but no mineralogical differences have been found (Ishiguro et al. 2007).

Two further missions planned to visit asteroids are currently flying: Dawn,

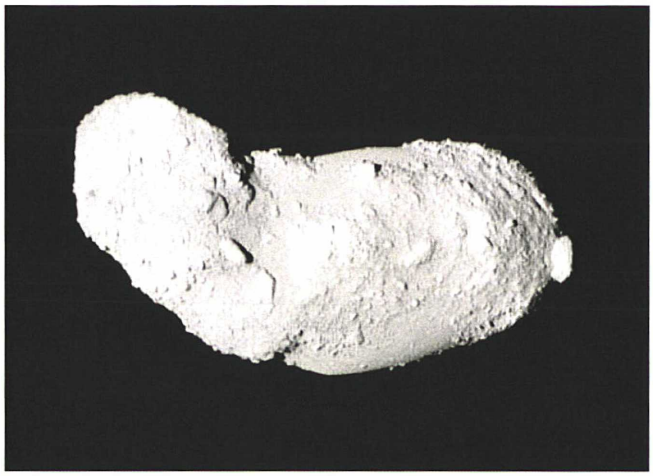

Figure 1.13 – Asteroid (25143) Itokawa taken by the Hayabusa probe.

which will orbit Vesta (arrival in 2011) and Ceres (arrival in 2015), the two largest bodies in the main belt; and Rosetta (see chapter 3), which flew-by asteroid (2867) Steins in September 2008 and will fly-by (21) Lutetia in July 2010, on its way to comet 67P/Churyumov-Gerasimenko.

1.4 Outer Solar System: far from the Sun

In the outer regions of the Solar System, far from the Sun, formation temperatures were sufficiently cold to let ices to condense and remain stable, allowing the Centaurs and TNOs nowadays observable to be a mixture of rocks and ices.

1.4.1 Taxonomy

A taxonomic scheme based on color indices has recently been developed for TNOs and Centaurs by Barucci et al. (2005a), using G-mode analysis (Coradini et al. 1977, see appendix A).

As already did in the past for the asteroids (see section 1.3.1), the investigation of broadband colors of the far (faint) minor bodies in the outer Solar System provides a first hint on their possible different composition and/or evolutionay history. Such an approach to studying the physical properties of asteroids has resulted in a taxonomy scheme based mostly on surface colors and albedos, and has become an efficient tool in asteroid science.

A two-letter designation for the identified groups is introduced to distinguish TNO taxonomy from asteroid taxonomy (Fig. 1.14):

The RR ("red") group contains the reddest objects of the Solar System. This behavior could be explained by the presence of large amounts of tholins on the surface (tholins are complex organics produced by the irradiation of mixtures of cosmically abundant reducing gases and ices, Roush & Cruikshank 2004), as it results from composition models available for some of them (Barucci et al. 2005a, and references therein).

Objects having neutral colors with respect to the Sun are classified as the BB ("blue") group. Typically their spectra are flat and slightly bluish in the near-infrared. The H_2O absorption bands seem generally stronger than in the other groups (Barucci et al. 2005a, and references therein).

The IR group includes moderately red objects, while the BR group is an intermediate group between BB and IR, with its colors closer to those of the IR group.

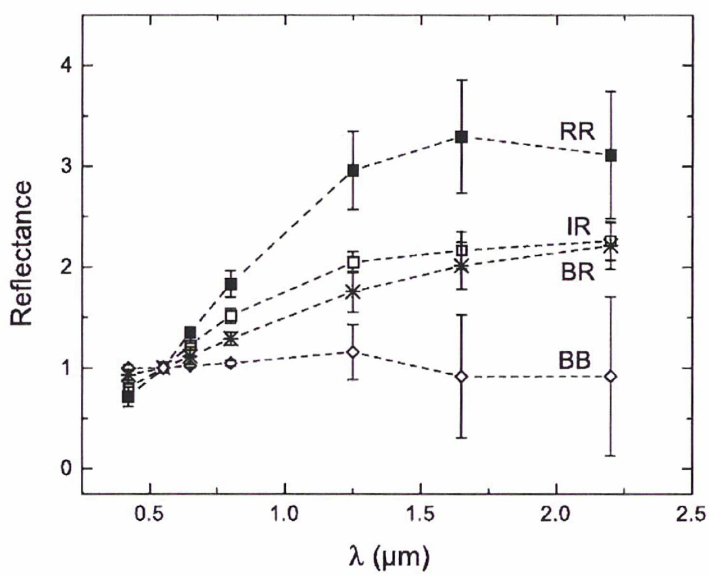

Figure 1.14 – Average reflectance values for each TNO taxon, normalized to the Sun and to the V colors. From Fulchignoni et al. (2008).

1.4.2 Surface composition

Even if only the brightest TNOs have been spectroscopically investigated, because of the faintness of these bodies, interesting results have been obtained regarding their surface composition.

A remarkable variety appears, with the presence of several ices on objects belonging to all of the four taxonomic classes discussed in the previous section. Barucci et al. (2006), using available literature, searched for correlations between the taxonomic group and the presence of ice, but none were found. Nevertheless the authors suggested that non-icy bodies seem to be concentrated in the RR group, as the probable presence of organic compounds (see previous section) on these bodies could hide the present ices. Moreover, it seems that ices are generally more abundant on BB-types than in the other taxa.

A relationship between the size of the objects and the presence of ice was also found by Barucci et al. (2006): all the larger bodies present signatures of ices on their surfaces, while limited or no detections emerged for the smaller objects. This has been interpreted as a natural consequence of different gravity fields, as the large majority of TNOs are too small to retain many volatile species.

Barucci et al. (2008a) identified four different spectral types among TNOs:

- *Methane-dominated:* the very largest TNOs belong to this group, e.g. Pluto, Eris, and Sedna (2003 EL_{61} is the largest TNO that does not show CH_4 signatures). Some objects present both CH_4 and N_2, with methane often dissolved in molecular nitrogen (e.g., Pluto and Sedna). In other objects the CH_4 ice is instead pure (as in the case of 2005 FY_9).

- *Water-ice-dominated:* a second group of TNOs presents spectra with strong H_2O absorptions (Fig. 1.15). The strongest signatures of water ice have been found in objects belonging to the dynamical family of (136108) Haumea. A giant impact on this body is supposed to have generated its dynamical family, as well as its multiple satellite system and its rapid rotation (Brown et al. 2007). Noteworthy, several "water-ice-dominated" TNOs show the 1.65 μm absorption due to crystalline water ice, which implies that during their lifes they have been heated to temperatures above 100/110 K. Since crystalline water ice should be unstable against energetic particle irradiation on timescales of $\sim 10^7$ years, cryovolcanic outgassing has been suggested to explain its detection (Jewitt & Luu 2004).

- *Water-ice spectra with methanol features:* some objects (2002 VE_{95}, 1998 GQ_{21}, and the Centaur Pholus) present a band at 2.27 μm, which is diagnostic of CH_3OH. This suggests a primitive nature of these bodies, since methanol, as other light hydrocarbons, is easily removed by heating in favor of macromolecular carbon.

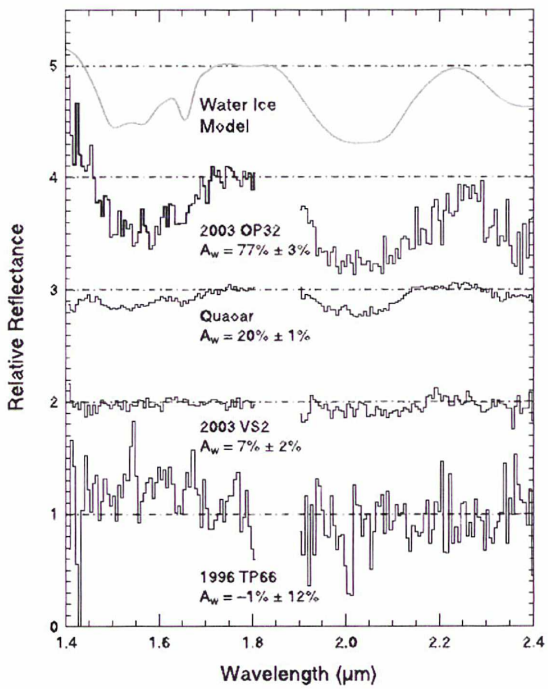

Figure 1.15 – Infrared reflectance spectra of four TNOs. A model spectrum of pure water ice (smooth, gray line) created using a Hapke model and an ice temperature of 40 K with a grain size of 50 μm, is presented for comparison. Quaoar and 2003 OP_{32} show the water ice absorptions at 1.5, 1.65, and 2.0 μm. The quantity Aw, quantifying the amount of water ice absorption at 2.0 μm, is reported next to each spectrum. From Barucci et al. (2008a).

- *Featureless spectra:* many TNOs have featureless spectra, independently of their taxonomic classification (BB to RR). They could have organic-rich surface mantles that cover interior ice.

1.4.3 Rotational properties and densities

The current spin properties of TNOs are supposed to have been strongly affected by the mutual collisions experienced by these bodies. The majority of larger TNOs should rotate with quite primordial angular momentums, while most of the smaller ones are probably fragments generated by disruptive collisions (Davis & Farinella 1997). Sheppard et al. (2008) suggested that an intermediate population of radii $50 \lesssim R \lesssim 100$ km should have been grav-

itationally stable to catastrophic break-up, but with spin properties highly altered over the age of the Solar System.

The largest TNOs have also probably relaxed to equilibrium shapes as a consequence of high internal pressures (Rabinowitz et al. 2006). Assuming a TNO as a cohesionless and strengthless body, i.e. a body with no tensile nor pressure-dependent strength (i.e. a fluid body), its density can be constrained by rotational stability considerations. Hence the analysis of its light curve allows to obtain hints about its internal structure. Indeed, a lower limit to the density of each observed object, below which centrifugal break-up would occur, can be derived by means of the equation:

$$\rho_{min} = \left(\frac{3.3}{P}\right)^2 (1 + \Delta m) \tag{1.11}$$

where P is the rotational period (expressed in hours), Δm is the maximum light curve amplitude, and the resulting density is expressed in g cm^{-3}. This formula is obtained by equating the centrifugal acceleration at the equator of a rotating prolate spheroid with its acceleration of gravity at the surface Pravec & Harris (2000).

Furthermore, possible density ranges can be estimated using the Chandrasekhar (1987) table for rotationally stable Jacobi ellipsoids. Minimum and maximum values of the density are obtained by inputting into the above-mentioned table the computed a/b lower limit (from Eq. 1.10) and $a/b = 2.31$ (more elongated ellipsoids are unstable to rotational fission, Jeans 1919), respectively.

It has been shown that while cohesion does not play a role in determining the permissible spin (for objects of diameter larger than about 10 km), any granular material (e.g., dry sand) can withstand considerable shear stress depending on the confining pressure, as a consequence of the interlocking of the granular particles (Holsapple 2001, 2004, 2007). This shear stress can be parameterized by the so-called angle of friction (ϕ). Typical values of the angle of friction in solid bodies are around 30°, while the fluid assumption implies that $\phi = 0$. Ice acts as a viscous fluid over timescales of years, so an icy body would relax to a fluid shape as described by Chandrasekhar (1987). Hence TNO density estimations through the above procedures are reasonable given the current knowledge and understanding of the physical nature of these bodies. Nonetheless, it should be emphasized that Holsapple showed how a "granular model", with non-zero ϕ, could describe such a body without constraining its shape to be a Maclaurin or Jacobi ellipsoid. This should be taken into account, especially in cases where extremely low (e.g., $\rho \leq 0.5$ g cm^{-3}) or extremely high (e.g., $\rho \geq 2.5$ g cm^{-3}) densities are derived

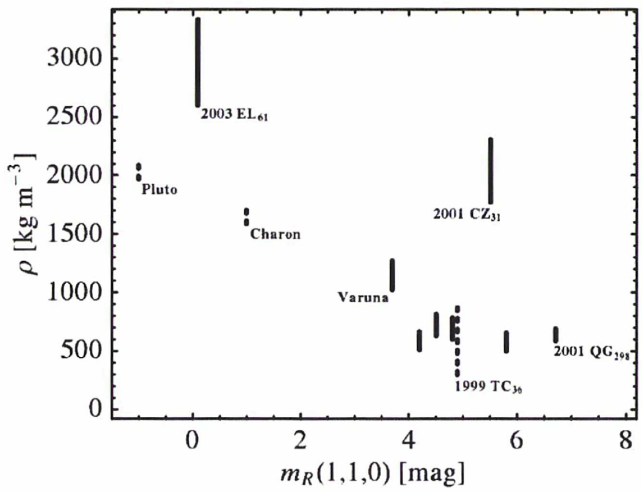

Figure 1.16 – Estimated density ranges of TNOs as a function of their absolute magnitude, before this work. Dashed lines correspond to densities of binary TNOs, estimated based on the satellite orbital properties. Solid lines indicate density ranges estimated from light curves. Figure adapted from Sheppard et al. (2008).

within a strenghtless scenario.

Using available data before this thesis, Sheppard et al. (2008) proposed the existence of a dimension/density trend, with larger (brighter) TNOs being denser than smaller (fainter) ones, suggesting that it could be caused by different porosity and/or rock/ice mass fraction for bodies of different sizes (Fig. 1.16).

Chapter 2

Data acquisition and reduction

In the framework of my PhD I mainly investigated the asteroid targets of the Rosetta space mission (Steins and Lutetia) and the minor bodies of the outer Solar System (Centaurs and Trans-Neptunian Objects). I carried out several observing runs, with the New Technology Telescope (NTT) and the Very Large Telescope (VLT) of the European Southern Observatory (ESO), and with the Telescopio Nazionale Galileo (TNG). I reduced and analysed these and other data in order to characterize the observed objects.

In particular:

- I acquired, reduced and analysed visible photometric and spectroscopic data on (2867) Steins, the first asteroid target of the Rosetta space mission. The observations were carried out at the TNG on April 2008, using the DOLORES instrument. Further data from Ukrainian collaborators have been combined in the analysis. All the details about the Steins observational campaign, as well as the obtained results, are given in section 3.1.

- I acquired, reduced and analysed visible spectroscopic data on (21) Lutetia, the second asteroid target of the Rosetta space mission. The observations were carried out at the Telescopio Nazionale Galileo (TNG) on November 2008, using the DOLORES instrument. This work is presented in section 3.2.

- I have been (and still I am) deeply involved in a Large Programme at ESO on Centaurs and Trans-Neptunian Objects (ESO-LP hereafter), during which data on 50 Centaurs and TNOs have been obtained for a total of 500 hours of observation spanning the years 2006-2008. I carried out two observing runs at the VLT, with the instruments FORS2 and ISAAC, and two runs at the NTT using the EMMI instrument.

I reduced and analysed all of the EMMI data and most part of the ISAAC data obtained in the framework of the ESO-LP. I contributed to the interpretation of the spectroscopic data, and, in particular, I took in charge the analysis and interpretation of the visible and NIR photometric data. The obtained results are presented in chapter 4.

Hereafter I will describe the procedures I adopted to acquire and reduce the data analysed in the framework of this thesis work.

2.1 Photometry

2.1.1 Visible

All of the visible photometric data presented in this thesis were reduced using the ESO-MIDAS software package. First of all CCD (*charge-coupled device*) images were pre-reduced with subtraction of the *bias* from the raw data and *flat-field* correction. A bias frame is an image obtained with zero exposure time and closed shutter. The image so obtained only contains noise due to the electronics that elaborate the sensor data, and not noise from charge accumulation within the sensor itself. Flat-field correction is used to remove artifacts that are caused by variations in the pixel-to-pixel sensitivity of the detector. A flat-field frame is obtained by observing a screen on the inside of the dome of the telescope, which is illuminated by dedicated lights (*dome* flat-fields), or by observing the sky during evening and/or morning twilight (*twilight* flat-fields), which better approximates uniform illumination than possible with dome flat-fields. Once a detector has been appropriately flat-fielded, a uniform signal will create a uniform output. Scientific frames are hence obtained from raw frames by subtracting the median bias image and dividing the result by the median (bias-subtracted, normalized) flat-field image.

Instrumental magnitudes were then measured via aperture photometry, with an integrating radius determined by growth curves (typically about three times the average seeing) and sky subtraction performed using a 5-10 pixel wide annulus around each object (Fig. 2.1).

Hence:

$$m_I = -2.5 \log(N) \tag{2.1}$$

where m_I is the instrumental magnitude and N is the obtained count rate (counts per second).

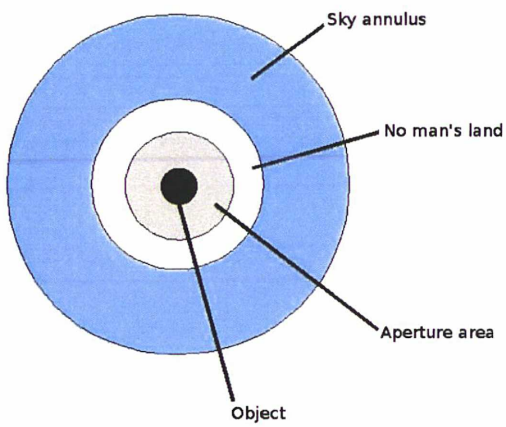

Figure 2.1 – Schematic illustration of the aperture photometry measurement.

For a few cases the *aperture correction* method was used to determine the object flux. Indeed, for faint objects (i.e., V $\gtrsim$ 22) a small aperture is needed to reduce the sky background contribution and the probability of contamination by a background source. The aperture correction also greatly helps when measuring the object flux in case of nearby stars. This method consists of measuring bright field stars with both a "small" aperture ($\sim$ 1 FWHM) and a bigger aperture to get all the light from the sources. From the ratio of light in the small to large aperture, which is of course expressed as a magnitude difference, it is possible to determine the correction to apply to the object magnitude, measured through the "small" aperture.

In this case:

$$m_I = -2.5 \log(N) + \Delta \tag{2.2}$$

where N is the count rate in the "small" aperture and Δ is the computed aperture correction.

Atmospheric extinction is taken into account correcting the magnitudes as:

$$m_0 = m_I - K(\lambda) \times X \tag{2.3}$$

where m_0 is the "zero airmass" magnitude (i.e., what it would be outside the atmosphere), $K(\lambda)$ is the wavelength dependent extinction coefficient and X is the *airmass*, defined as (in a plane-parallel atmosphere approximation):

$$X \sim \sec z = \frac{1}{\sin\phi \sin\delta + \cos\phi cos\delta \cos h} \tag{2.4}$$

where z is the zenith angle, ϕ is the latitude of the observatory, and δ and h are the declination and the hour angle of the observed object, respectively.

The atmospheric extinction depends by the wavelength because of several physical effects: Rayleigh scattering, ozone or H_2O molecular absorption and aerosol scattering. For example, the amount of Rayleigh scattering off of atoms and molecules, much smaller than the wavelength of light, goes as λ^{-4}, so drops rapidly towards longer wavelength, while ozone has extinction that sharply rises blueward of about 0.32 μm, plus another small bump at about 0.6 μm. Hence, a color dependence was taken into account through a second order correction:

$$K(\lambda) = K' + K'' \times CI \tag{2.5}$$

where K' and K'' are the main (or first order) extinction coefficient and the color correction (or second order) extinction coefficient, respectively, and CI is a color index, defined as the difference between magnitudes in two different bands.

Finally, adding the *zero point* (ZP), instrumental magnitudes were converted in standard system magnitudes:

$$M = m_0 + ZP \tag{2.6}$$

The above descripted calibration of the magnitudes was obtained by means of the observation of several Landolt (1992) standard fields, at different airmasses, throughout each observing night.

2.1.2 Near-infrared

At NIR wavelengths the brightness and rapid variability ($\sim$ 5-10 minutes) of the sky requires total exposure times to be splitted in short exposures of 2-3 minutes at most (Detector Integration Time, DIT); being NDIT the number of DIT exposures averaged out within the same frame and NINT the number of frames, the total exposure time is therefore DIT $\times$ NDIT $\times$ NINT.

Jitter imaging is used to take care of sky background issues: giving small (i.e., no larger than a reasonably small fraction of the detector size) offsets between the different exposures, it is possible to deduce the sky background variations directly by filtering the images, and to separate the astronomical and the sky signals.

Also, unlike optical CCDs, the dark current correction is important for infrared arrays. Hence, an average of several (exposure time dependent) *dark frames* have to be subtracted from subsequent images.

The data were pre-reduced (dark subtraction, flat-field correction, bad pixel cleaning, sky subtraction, recombination of the images) by using the ESO ISAAC pipeline (which runs through EsoRex, the "ESO Recipe Execution Tool"). Then, as for the visible images, target fluxes were mostly measured (with ESO-MIDAS) using classical photometry methods with apertures determined by the seeing and growth curves of the objects, reserving the aperture correction method to a few cases (faint target and/or nearby field stars).

To calibrate the instrumental magnitudes (using the same procedure described in the previous section for visible images), standard stars from different catalogues (Persson et al. 1998; Hawarden et al. 2001) were observed.

2.2 Spectroscopy

2.2.1 Visible

All of the spectra were acquired through a slit oriented along the parallactic angle in order to minimize the effects of atmospheric differential refraction.

The data were reduced using ESO-MIDAS. The basic procedure for converting raw spectral flux measurements to reflectance spectra, as for photometric data, started with median bias subtraction and flat-field correction. After that, the 2-D spectra were transformed in monodimensional spectra integrating the flux along the spatial axis (with aperture radius usually around 1.5 FWHM) and subtracting the sky contribution. Then, wavelength calibration was performed through spectral lines from different (He, Ar, Ne) calibration lamps and atmospheric extinction correction was taken into account according to the extinction law for each observing site. At this point spectra were normalized usually at 0.55 μm and the reflectivity of the objects was obtained by dividing their spectra by the spectrum of a solar analog star which had been acquired close in time and airmass (to have the atmospheric conditions the most similar as possible). Finally, the spectra were smoothed with a median filter technique. This means that, using a box of about 30-

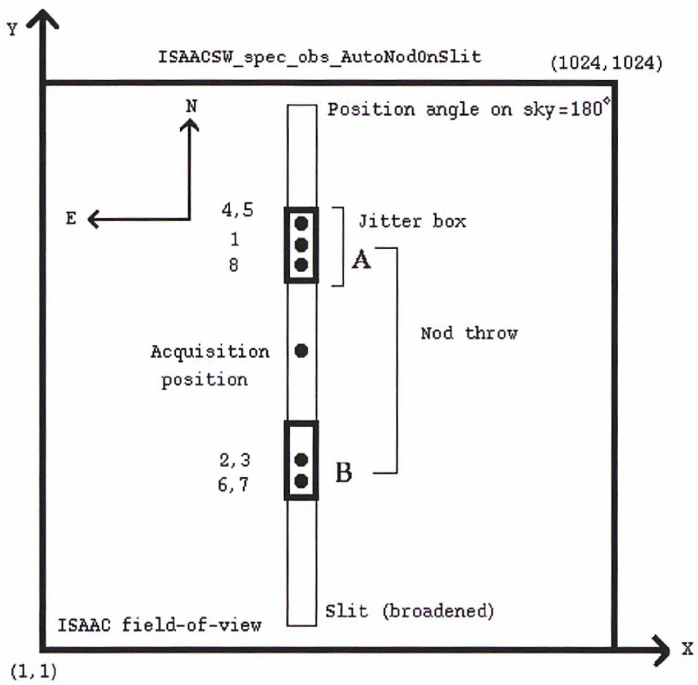

Figure 2.2 – Illustration of the ISAACSW_spec_obs_AutoNodOnSlit template, used in NIR spectroscopy with the ISAAC instrument at the VLT. The black dots represent the different positions of an object originally at the center of the slit. From the ISAAC user manual.

40 Å in the spectral direction for each point of the spectrum and a threshold around 10-15%, the original value has been replaced by the median value when this latter differed from the former by more than the threshold.

2.2.2 Near-infrared

Because of the high luminosity and variability of the sky in the NIR, the observations were carried out by moving (usually by 10 arcseconds) the object along the slit between two positions A and B (the classical *nodding* technique used in NIR spectroscopy). Cycles are repeated on ABBA sequences, until the total exposure time is reached. In addition to nodding, random offsets are added to the positions A_i and B_i. The random offsets, much smaller than the "nod throw", are generated inside a "jitter box" (Fig. 2.2). This way the sky contribution, including the random fluctuations, is effectively removed by subtracting one frame from the other.

First steps of the reduction procedure were performed using the ISAAC pipeline: flat-fielding, wavelength calibration (through atmospheric OH lines or Xe-Ar lamp lines), A-B (or B-A) subtraction for each pair of frames (the subtracted frames hence contain positive and negative spectra), correction for spatial and spectral axes distortion, shifting and adding of the frames. The resulting combined spectrum of the object was then extracted using ESO-MIDAS. Because of the rapid changes of the absorption at NIR wavelengths, the atmospheric extinction correction cannot be done as in the visible: it is hence fundamental to get the reflectivity of the object by dividing its spectrum by that of a solar analog star observed just before or after the object, at airmass as similar as possible. As for visible data, the spectra were finally smoothed with a median filter technique (with a box of $\sim$ 10 Å in the spectral direction and a threshold around 10-25%).

Chapter 3

Rosetta asteroid targets

Rosetta is a space mission led by the European Space Agency (ESA) which takes its name from the Rosetta Stone, a stele of black basalt which provided the key to deciphering Egyptian hieroglyphs. It was originally set to rendezvous with the comet 46P/Wirtanen in 2011, but the original launch date was postponed because of the failure of the Ariane V launcher (December 2002). A new mission baseline was formed (Fig. 3.1), and Rosetta was successfully launched on March 2004 with the main objective to enter orbit around the comet 67P/Churyumov-Gerasimenko and to perform observations of its nucleus and coma.

During its 10 years journey to the comet, the spacecraft performs also the fly-by of two main belt asteroids, (2867) Steins and (21) Lutetia. The fly-by with Steins took place on September 2008, while the one with Lutetia is scheduled on July 2010. An ESA Science Working Group selected these two bodies based on the results by Barucci et al. (2005c), which studied all the candidates of all the possible mission scenarios: Lutetia emerged as the most interesting target for both its large size ($\sim$ 100 km), which makes radio science experiments feasible, and its puzzling nature with a possible primitive composition, which could provide insight into the early Solar System conditions; after the choice of the first target, Steins was the best candidate for a second fly-by, with its relatively unusual (E-type) spectral properties.

As already stated, the physical characterization of the asteroid targets of space missions is fundamental for both the optimization of the mission operations and the "calibration" of standard ground-based observations of asteroids (*ground truth*). Keeping this in mind, in the framework of my PhD I performed a ground-based investigation of asteroids (2867) Steins and (21) Lutetia, as described in sections 3.1 and 3.2 respectively.

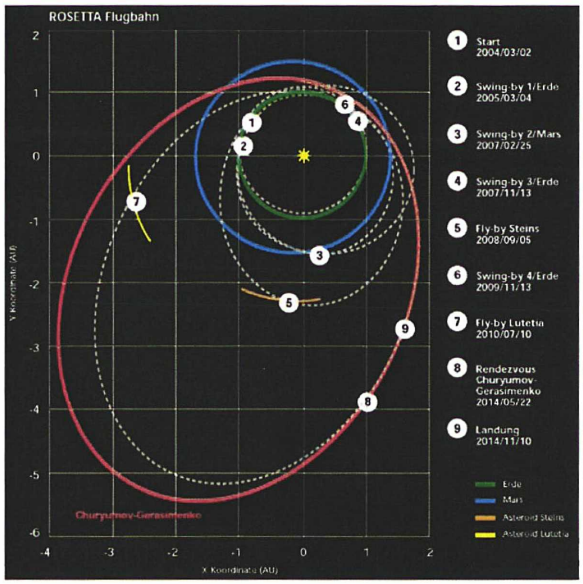

Figure 3.1 – Rosetta's flight plan.

3.1 (2867) Steins

Steins is a small (few km) main belt asteroid and its ground-based investigation started only in early 2004, when it was included in the list of possible asteroid targets of Rosetta.

In March 2004 Steins was observed photometrically by both Warner (2004) and Hicks et al. (2004), who measured synodic periods of 6.05±0.01 hours and 6.06±0.05 hours, respectively. A full analysis of the latter set of observations was reported by Weissman et al. (2007), who obtained a revised synodic period of 6.048±0.007 hours. Imaging performed during the cruise phase of Rosetta by the Narrow Angle Camera (NAC) of the Optical Spectroscopic and Infrared Remote Imaging System (OSIRIS), allowed Küppers et al. (2007) and Jorda et al. (2008) to derive P_{syn}=6.052±0.007 hours and P_{syn}=6.054±0.003 hours, respectively. Moreover, by compiling a set of 26 visible light curves belonging to 6 data sets obtained by ground-based observatories and one by the spacecraft, Lamy et al. (2008b) computed a sidereal period of 6.04681±0.00002 hours.

Visible and near-infrared spectroscopic observations of Steins obtained by Barucci et al. (2005c) revealed a spectral behavior similar to that of E-type asteroids (thought to be differentiated bodies which experienced significant heating). In particular, its spectrum resembles those of the E[II] subtype (or "Angelina-like", from (64) Angelina) within the classification by Gaffey &

Kelley (2004) and Clark et al. (2004), with the presence of a strong feature at about 0.5 μm, a weaker feature at about 0.96 μm, and a flat and featureless behavior beyond 1 μm. These absorption features are characteristic of oldhamite, a calcium sulfide mineral which is present only in highly reduced assemblages such as aubrites (enstatite achondrite meteorites). The absorption features probably arise from the presence of a trace of bivalent iron in the sulfide. Although the geochemical behavior of oldhamite in highly reduced igneous systems is not completely understood (oldhamite is an extremely unstable element in terrestrial atmospheric conditions), it seems likely that it will be significantly enriched in early partial melts from enstatite chondrite source materials. Hence, the E[II] asteroids may be composed of basalt equivalents from E-chondrite-like parent bodies which underwent at least partial melting (e.g., Gaffey & Kelley 2004, and references therein). Burbine et al. (1998) proposed that the feature at 0.49 μm is due to troilite, but this is problematic because E-types are by definition very high albedo objects and troilite is naturally a very dark mineral component. It has been shown that even minute amounts of a spectrally dark component can nonlinearly darken a mineral mixture (Clark & Lucey 1984), making it very unlikely that troilite is a major component of the surfaces of these bright objects. Nevertheless, troilite is a component found in minor amounts in aubrite meteorites (Clark et al. 2004, and references therein).

Steins' albedo was derived by Fornasier et al. (2006) on the basis of polarimetric observations carried out at ESO-VLT in 2005. Using the well-known (e.g., Cellino et al. 1999a, 2005) empirical relationship between the albedo and the slope of the polarimetric curve (polarization degree versus phase angle), the authors determined an albedo of 0.45±0.10, a high value consistent with the E-type classification suggested by the spectroscopic behavior. A new determination of the geometric albedo, obtained by thermal modeling of data from the Spitzer Space Telescope, inferred a value of p_V=0.34±0.06 (Lamy et al. 2008a). This value appeared to be slightly low for an E-type object, although the Spitzer emissivity spectrum between 5.2 and 38 μm was consistent with that of aubrite meteorites and enstatite minerals (Barucci et al. 2008b), and confirmed the E-type classification.

3.1.1 Observational campaign

Until April 2008, neither photometric observations nor light curves of Steins were available for phase angles $\alpha < 7°$, while this region is particularly important for the determination of the asteroid absolute magnitude H and slope parameter G (see section 1.2.1).

To investigate and assess the physical properties of Steins before the

Rosetta encounter, I participated to an observational campaign (Spring 2008) during which low phase angle visible spectroscopy and visible photometry of the asteroid were performed. These observations were important to complete the ground-based data set, and to compute the physical parameters of Steins that are fundamental for properly calibrating the imaging and spectroscopic data acquired by instruments onboard Rosetta.

Photometric observations were carried out at the Institute of Astronomy of the Kharkiv Karazin National University (70 cm reflector), the Simeiz Department of the Crimean Astrophysical Observatory (1 m reflector), and the 3.6 m Telescopio Nazionale Galileo (TNG, La Palma, Spain). The observational circumstances are reported in Table 3.1.

At TNG visible spectra were also acquired using the DOLORES (Device Optimized for the LOw RESolution) instrument with the low resolution blue (LR-B) and red (LR-R) grisms. Table 3.2 reports, for each spectrum, the starting time of acquisition, the used grism, the exposure length, the airmass, and the solar analog star (with its airmass) used to obtain the Steins' reflectivity.

Data reduction was performed as described in chapter 2 for both photometry and spectroscopy, and the calibrated data were corrected for light-time.

Table 3.1 – Observational circumstances for Steins (r, Δ, and α are the heliocentric distance, the topocentric distance, and the phase angle, respectively).

Date	r (AU)	Δ (AU)	α (deg)	Filters	Observatory
31 Mar 08	2.387	1.442	10.05	vr	Kharkiv
10 Apr 08	2.370	1.385	5.77	vr	Kharkiv
12 Apr 08	2.368	1.378	5.03	VR	Kharkiv
17 Apr 08	2.359	1.361	3.50	VR	TNG
18 Apr 08	2.358	1.359	3.36	VR	TNG
19 Apr 08	2.356	1.357	3.29	VR	TNG
20 Apr 08	2.354	1.355	3.30	VR	TNG
02 May 08	2.335	1.353	7.34	VR	Kharkiv
04 May 08	2.331	1.356	8.27	BVR	Kharkiv
10 May 08	2.322	1.372	11.01	VR	Kharkiv
11 May 08	2.320	1.375	11.46	VR	Kharkiv
31 May 08	2.287	1.485	19.38	VR	Simeiz
02 Jun 08	2.284	1.499	20.01	VR	Kharkiv
03 Jun 08	2.282	1.507	20.33	VR	Kharkiv

Table 3.2 – Visible spectroscopy of Steins performed at TNG.

#	Date	UT_{start} (hh:mm)	Grism	T_{exp} (s)	Airmass	Solar analog (airmass)
1	17 Apr	23:56	LR-B	900	1.27	Landolt 102-1081 (1.16)
2	18 Apr	23:56	LR-B	900	1.25	HD 144873 (1.14)
3	19 Apr	03:04	LR-B	900	1.36	HD 144873 (1.14)
4	20 Apr	00:03	LR-B	600	1.23	Landolt 102-1081 (1.19)
5	20 Apr	00:15	LR-R	900	1.22	Landolt 102-1081 (1.19)
6	20 Apr	00:34	LR-B	900	1.20	Landolt 102-1081 (1.19)
7	20 Apr	01:29	LR-B	900	1.19	Landolt 102-1081 (1.19)
8	20 Apr	01:50	LR-R	900	1.21	Landolt 102-1081 (1.19)

3.1.2 Light curves

Figure 3.2 shows the composite light curves derived for the V and R bands. They are consistent within the error bars and characterized by rather symmetrical shape.

A rotational synodic period of $P_{syn} = 6.057 \pm 0.003$ was computed by applying the method developed by Harris et al. (1989a) based on Fourier analysis of light curves, as described in section 1.2.1. The light curve amplitude is 0.20 ± 0.02 mag in both bands, which provides (from Eq. 1.10) a lower limit to the axis ratio, $a/b \geq 1.20 \pm 0.02$ assuming that Steins does not have considerable albedo variations and that the observed amplitude is only affected by the asteroid shape.

The composite light curves were used to convert all measured magnitudes into those corresponding to the light curve maximum, which is less affected by the asteroid shape. This was possible with a good accuracy, since most of the observations covered one or both maxima. Adding half of the light curve amplitude, mean R and V magnitudes for each night were derived. The obtained values are reported in Table 3.3, with a resulting color of $V - R = 0.51 \pm 0.03$ mag.

3.1.3 Phase curve

Fig. 3.3 presents the magnitude-phase dependence of Steins in R band, where also previously published observations obtained in 2004 - 2008 by Hicks et al. (2004), Weissman et al. (2007), Jorda et al. (2008), and Lamy et al. (2008b) have been used. These measurements were corrected for the light curve amplitude in the same way as described above. A good agreement between the data obtained at different oppositions emerges, confirming that the ro-

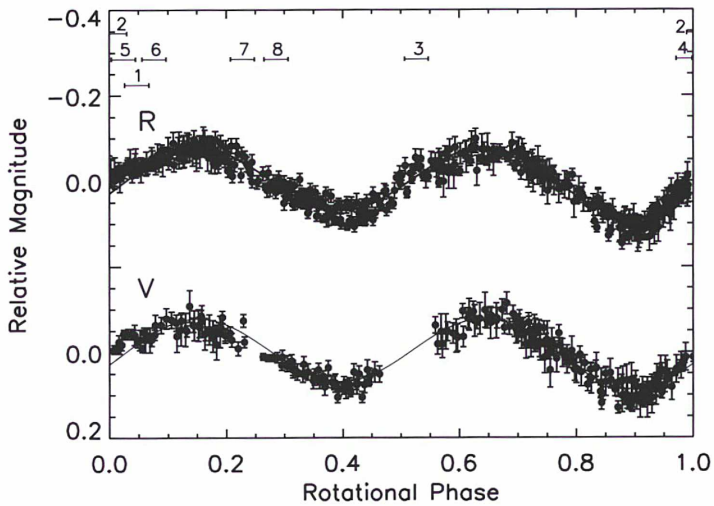

Figure 3.2 – Composite R and V light curves of Steins. The coverage of the obtained spectra is shown on the top of the data. The light curve zero-point is at 0 UT on 19 April 2008. From Dotto et al. (2009).

Table 3.3 – V and R magnitudes of Steins.

Date	α (deg)	R (mag)	V (mag)
12 Apr 08	5.03	13.14±0.02	13.67±0.02
17 Apr 08	3.50	13.13±0.02	13.65±0.02
18 Apr 08	3.36	13.11±0.03	13.64±0.03
19 Apr 08	3.29	13.12±0.02	13.64±0.02
20 Apr 08	3.30	13.12±0.04	13.66±0.04
02 May 08	7.34	13.22±0.02	13.72±0.02
04 May 08	8.27	13.26±0.02	13.75±0.02
10 May 08	11.01	13.33±0.03	13.81±0.03
11 May 08	11.46	13.35±0.02	13.83±0.02
31 May 08	19.38	13.55±0.02	–
02 Jun 08	20.01	13.52±0.03	14.02±0.03
03 Jun 08	20.33	13.53±0.02	14.04±0.03

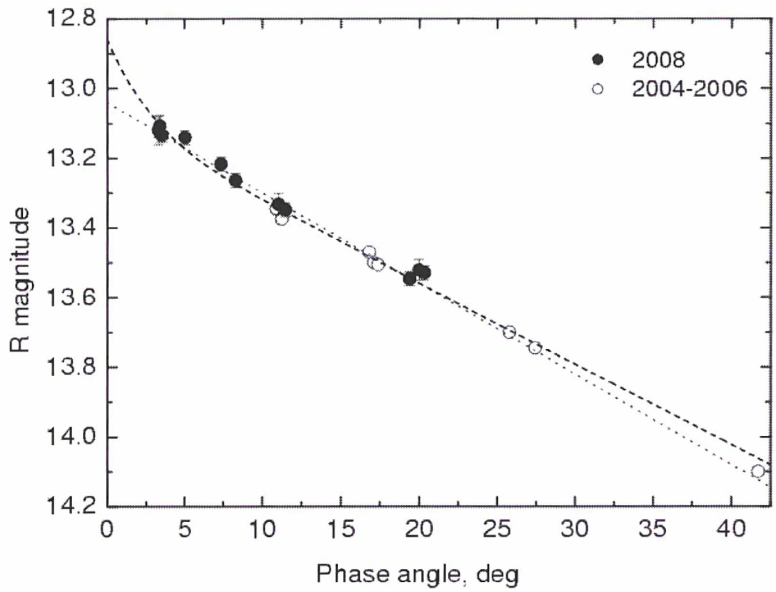

Figure 3.3 – Phase curve of Steins in the R band fitted by linear (dotted line) and H-G fit (dashed line). From Dotto et al. (2009).

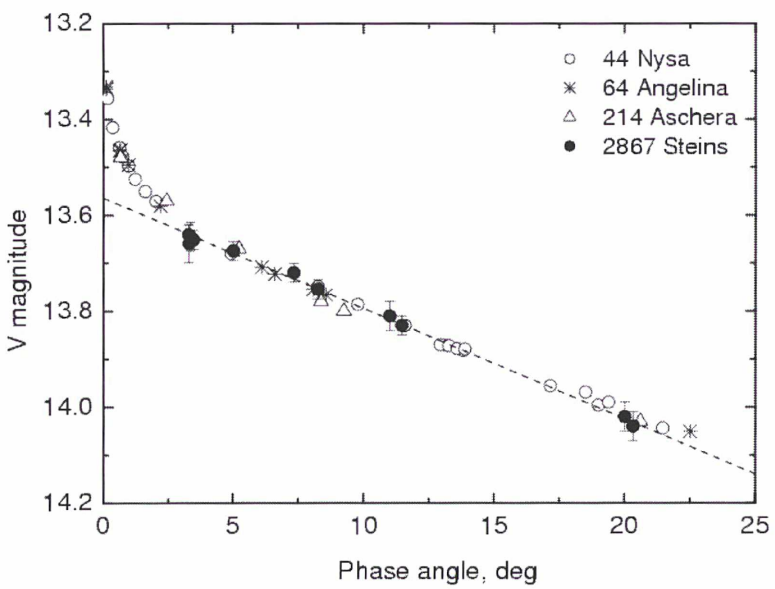

Figure 3.4 – Magnitude-phase dependence in the V band of Steins and other E-type asteroids. From Dotto et al. (2009).

tation axis of Steins is almost perpendicular to the ecliptic plane (Lamy et al. 2008b), thus that Steins is observed at almost the same aspect angle ($\xi \sim 86°$) in different apparitions. According to the Bowell et al. (1989) formalism (see section 1.2.1), all of these data were used to compute the R band absolute magnitude and slope parameter (V band phase parameters would be less accurate because of the smaller dataset), with resulting values of $H_R = 12.86 \pm 0.02$ and $G_R = 0.42 \pm 0.02$. The G_R here obtained is higher than in previous works, but this discrepancy could be due to a lack of observations at phase angle lower than 7° in previously analyzed samples. The obtained "H-G fit" is consistent with a linear fit for the observed range of phase angles with slope $\beta_R = 0.026 \pm 0.001$ and y-intercept $R(0) = 13.04 \pm 0.02$ (see Fig. 3.3). The shallow slope observed for Steins is typical of E-type asteroids (e.g., Belskaya et al. 2003), and strongly supports its classification in this taxon.

A comparison of the magnitude-phase dependence of Steins and other E-types is shown in Fig. 3.4. All of these data (from Harris et al. 1989b; Belskaya et al. 2003) were obtained in the V-band and shifted in magnitude to match the Steins data. By assuming that the amplitude of the opposition effect of Steins is similar to that of the other E-type asteroids (0.23 ± 0.03, Belskaya & Shevchenko 2000), it is possible to calculate the Steins' R absolute magnitude by adding the value of the opposition effect to $R(0)$, obtaining a value of $H_R = 12.81 \pm 0.03$.

3.1.4 Spectral properties and modelling

Eight spectra of Steins have been obtained during the observations at TNG (Fig. 3.5), exhibiting the typical behavior of E[II] asteroids: all of them are almost flat and featureless between 0.55 and 0.9 μm, and present the before discussed absorption signature at 0.49 μm. The spectral slopes, computed between 0.56 and 0.79 μm, are reported in Table 3.4.

The coverage of the Steins' light curve by the eight spectra is shown in Fig. 3.2. Since the same spectral behavior is found for $\sim 30\%$ of the rotational light curve, it is possible to argue that Steins has a quite homogeneous surface composition.

In Fig. 3.6, the spectrum #2 (LR-B grism) and the spectrum #5 (LR-R grism), which cover almost the same surface region, are plotted together. Using a radiative transfer model (based on the Hapke theory), that had already been used to model the surface composition of Jupiter Trojans, Trans-Neptunian Objects, and Centaurs (e.g., Dotto et al. 2003, 2006), an attempt to reproduce the spectral behavior of Steins has been perfomed using geographical mixtures of different components (i.e., distributed as different

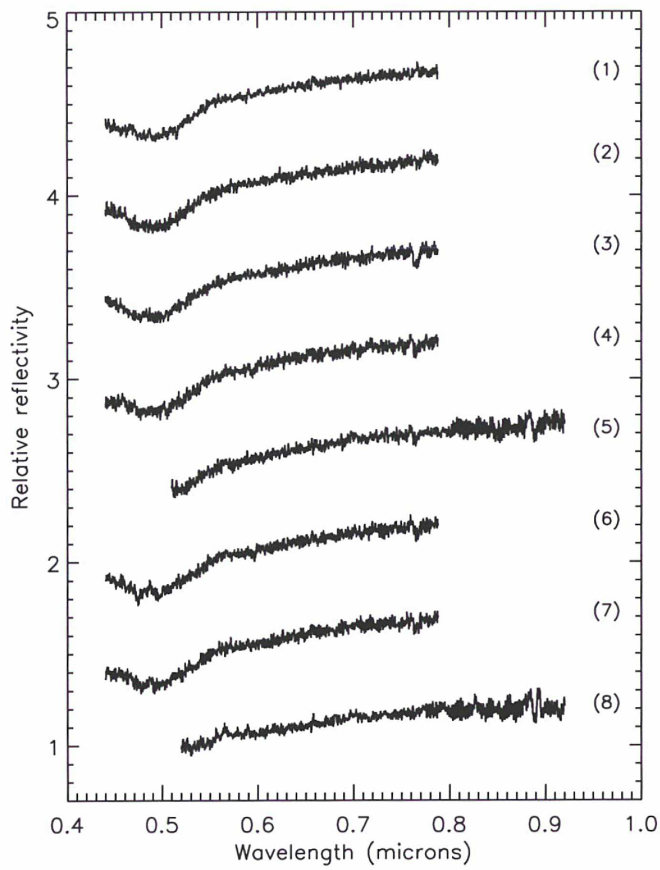

Figure 3.5 – Visible spectra of Steins normalized at 0.55 μm and shifted by 0.5 in reflectivity for clarity. From Dotto et al. (2009).

patches on the surface) selected from enstatite meteorites and correlated minerals included in the RELAB[1] (KECK/NASA Reflectance Experiment Laboratory) catalog. The continuous line in Fig. 3.6 shows the synthetic spectrum of a mixture consisting of 55% enstatite achondrite meteorite (aubrite) Mayo Belwa and 45% oldhamite (this mixture has an albedo of 0.35).

On the basis of these results the surface of Steins appears to be homogeneous, and its composition, as already suggested by both Barucci et al. (2005c) and Fornasier et al. (2007, 2008), resembles the enstatite meteorites, in particular the aubrites, enriched in oldhamite.

[1] http://www.planetary.brown.edu/relab/

Table 3.4 – Spectral slopes of Steins' spectra.

#	Spectral slope (% / 10^3Å)
1	6.88±0.65
2	7.09±0.65
3	7.12±0.65
4	7.48±0.65
5	8.26±0.65
6	7.75±0.65
7	7.25±0.65
8	6.48±0.65

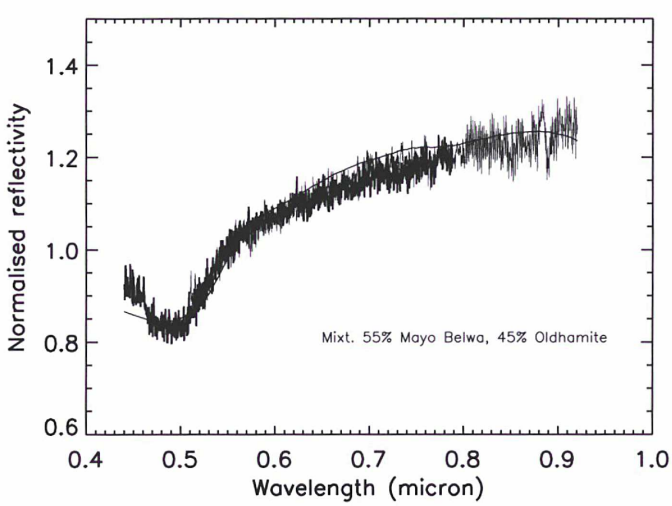

Figure 3.6 – Spectra #2 and #5, normalized at 0.55 μm. The continuous line shows the tentative model of the Steins surface composition. From Dotto et al. (2009).

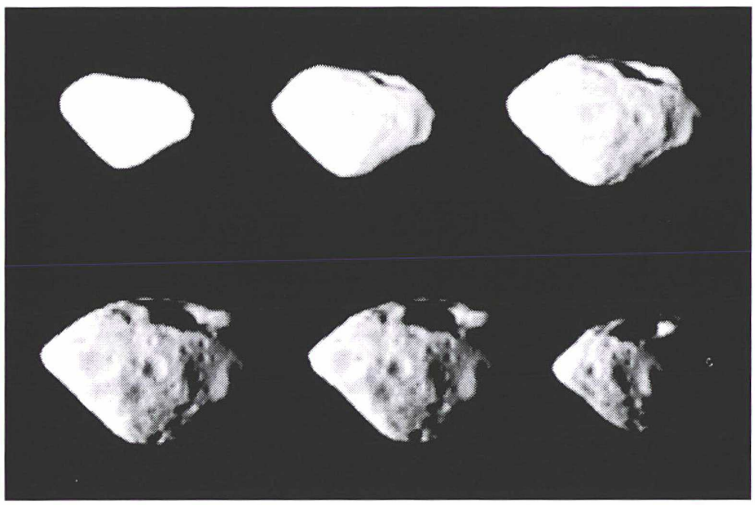

Figure 3.7 – Asteroid Steins taken by the OSIRIS instrument. The large crater at the southern (according to IAU rules, see text) pole can be seen. Images from ESA - OSIRIS Team.

3.1.5 Steins seen by Rosetta

On 5 September 2008 Rosetta successfully made a close ($\sim$ 800 km) fly-by of Steins (Fig. 3.7). Altogether 14 instruments were switched on during the fly-by, providing spatially resolved multi-wavelength observations of the asteroid and in-situ measurements of its dust, plasma, magnetic, and radiation environment.

Among the first obtained results, Steins resulted to be a diamond-shaped asteroid with dimensions of 4.0 $\times$ 5.9 km, dominated by a large ($\sim$ 2 km) crater at the southern pole (Steins's rotation is retrograde, therefore its north pole points toward the celestial south according to the rules of the International Astronomical Union). From there a chain of 7 craters extends across the surface visible during the fly-by. More than 20 craters with diameters > 0.2 km can be counted (Keller et al. 2009). The geometric albedo resulted to be 0.40 $\pm$ 0.01 and the slope parameter G is 0.45, both typical values for E-type asteroids. The visible spectrum is slightly reddish, with a sharp drop-off in reflectance towards the near-ultraviolet region, in agreement with ground-based observations (Küppers et al. 2009).

The results presented in this thesis, deriving from the last ground-based dataset obtained before the Rosetta fly-by, are particularly important for the calibration and interpretation of the data acquired by the spacecraft. The analysis of the latter is still ongoing, but in general it seems that the Rosetta data are well comparable with those obtained from ground-based investigations, strengthening the *ground truth*.

3.2 (21) Lutetia

Although several observations of (21) Lutetia are available since a couple of decades, the nature of this asteroid is still controversial. Its rotational period was firstly measured by Zappala et al. (1984), who found $P = 8.17 \pm 0.01$ hours, and later refined by Torppa et al. (2003), who found $P = 8.165455$ hours and also computed the pole coordinates obtaining a model with axis ratios $a/b = 1.2$ and $b/c = 1.2$. IRAS (InfraRed Astronomical Satellite) observations of Lutetia gave a diameter of about 96 km and an albedo of 0.22. Because of the latter high value, later confirmed by Mueller et al. (2006) who found a value of 0.208 ± 0.025, Lutetia was classified as a M-type asteroid by Barucci et al. (1987) and Tholen (1989). Considering that M-types have spectral properties and albedo values consistent with Fe-Ni metal and are generally thought to be the metallic cores of differentiated asteroids exposed after catastrophic disruptions, Lutetia was supposed to be an evolved object which suffered a strong heating and alteration. Nevertheless, further observations did not confirm the metallic nature of Lutetia, suggesting rather a primitive surface composition. Howell et al. (1994) and Burbine & Binzel (2002) showed that the infrared spectrum of Lutetia is unusually flat compared to other M-type asteroids. Moreover, observations obtained by Barucci et al. (2005c) and Birlan et al. (2004) suggested a similarity with carbonaceous chondrite spectra which characterize the C-type asteroids. Lazzarin et al. (2004) obtained several visible spectra showing variations with the rotational phase, and the possible presence of features at 0.43 and 0.51 μm probably associated to hydrated silicates. In a single spectrum the authors also found two minor absorptions at $\sim$ 0.6 μm and 0.80-0.85 μm, which have been already detected in the spectra of aqueously altered meteorites and several hydrated asteroid classes. Lazzarin et al. (2009) presented a wide mineralogical assessment of Lutetia, found broad complex features between 0.45 and 0.55 μm, and two narrower features around 0.47 and 0.52 μm. Some more, the polarimetric properties of Lutetia are better explained by a carbonaceous chondritic composition than by metallic composition (Belskaya & Lagerkvist 1996), its radar albedo would be the lowest measured for any M-class MBA (Magri et al. 1999), and recent ground-based infrared observations allowed Carvano et al. (2008) to obtain a geometric albedo of 0.129, significantly lower than all the previous estimations. The latter authors explained the wide range of computed albedo values as the evidence of inhomogeneities on the surface of Lutetia, suggesting the presence of one or more large craters on the northern hemisphere.

Rivkin et al. (2000) detected an absorption feature at 3 μm, diagnostic of water of hydratation and further evidence that Lutetia is largely non-

metallic. Birlan et al. (2006) confirmed the presence of the 3 μm band and defined an upper limit of 0.5% concerning a possible absorption band at about 3.1 μm. Spitzer observations carried out by Barucci et al. (2008b) between 5.2 and 38 μm revealed a clear analogy to carbonaceous chondrite meteorites, in particular the CO-CV types.

More recently, Vernazza et al. (2009) obtained spectra of Lutetia which seem to indicate that the surface composition of this object could have some genetic link with more evolved enstatite chondrite meteorites.

Hence, even if most of the authors agree about the primitive composition of Lutetia, on the basis of the observational evidence this asteroid appears to be an atypical puzzling object, whose nature is still far to be fully understood.

3.2.1 Observations

In order to enhance the view of Lutetia prior to the Rosetta fly-by, I contributed to a spectroscopic investigation of this intriguing object. Observations have been carried out in November 2008 at the TNG, using the DOLORES instrument with the low resolution blue (LR-B) grism. Table 3.5 reports, for each obtained spectrum, the starting time of acquisition, the exposure length, the airmass, and the airmass of the spectrum of solar analog Hyades 64 used to obtain the Lutetia's reflectivity.

Data reduction followed the procedures described in chapter 2 (acquisition times were corrected for light-time). The resulting spectra are cut at 0.45 μm, since at lower wavelengths their behavior is strongly affected by the spectra of the solar analogs.

3.2.2 Results and discussion

The obtained spectra are shown in Fig. 3.8. Table 3.6 reports the coverage of the rotational phase and the spectral slope (computed between 0.6 and 0.75 μm) for each of them.

The general spectral behaviour is similar in all the spectra, but some differences are evident. All of them exhibit two spectral features at about 0.47-0.48 μm and around 0.6 μm. Both these spectral features have been already seen on the spectra of (21) Lutetia (see above). The signature at $\sim$ 0.47-0.48 μm was already detected on spectra of Lutetia by Lazzarin et al. (2009), who interpreted them as due to spin-allowed crystal field transitions in Ti^{3+} in pyroxene Y sites (pyroxenes have the general formula $XY(Si,Al)_2O_6$), although Hazen et al. (1978) suggested that in lunar pyroxenes such a band could be due to the superimposition of Ti^{3+} and Fe^{2+} effects.

Table 3.5 – Visible spectroscopy of Lutetia performed at TNG.

#	Date	UT_{start} (hh:mm)	T_{exp} (s)	Lutetia airm.	Hyades 64 airm.
1	27 Nov	23:39	8	1.07	1.04
2	27 Nov	23:53	30	1.05	1.04
3	28 Nov	00:49	40	1.01	1.04
4	28 Nov	01:33	40	1.02	1.04
5	28 Nov	02:23	40	1.07	1.04
6	28 Nov	03:05	40	1.14	1.04
7	28 Nov	03:54	40	1.30	1.04
8	28 Nov	04:32	40	1.50	1.04
9	29 Nov	22:18	40	1.23	1.02
10	29 Nov	23:12	40	1.09	1.02
11	29 Nov	23:13	30	1.09	1.02
12	30 Nov	00:07	30	1.03	1.02
13	30 Nov	00:57	40	1.01	1.02

Table 3.6 – Coverage of the rotational phase and slope of each obtained spectrum of Lutetia.

#	Rotational phase	Spectral slope (% / 10^3Å)
1	0.018	1.5±0.5
2	0.046	1.0±0.5
3	0.161	1.4±0.5
4	0.251	1.8±0.5
5	0.353	2.2±0.5
6	0.438	2.0±0.5
7	0.538	2.1±0.5
8	0.616	1.7±0.5
9	0.731	0.7±0.5
10	0.841	1.4±0.5
11	0.843	1.6±0.5
12	0.953	1.7±0.5
13	0.056	1.7±0.5

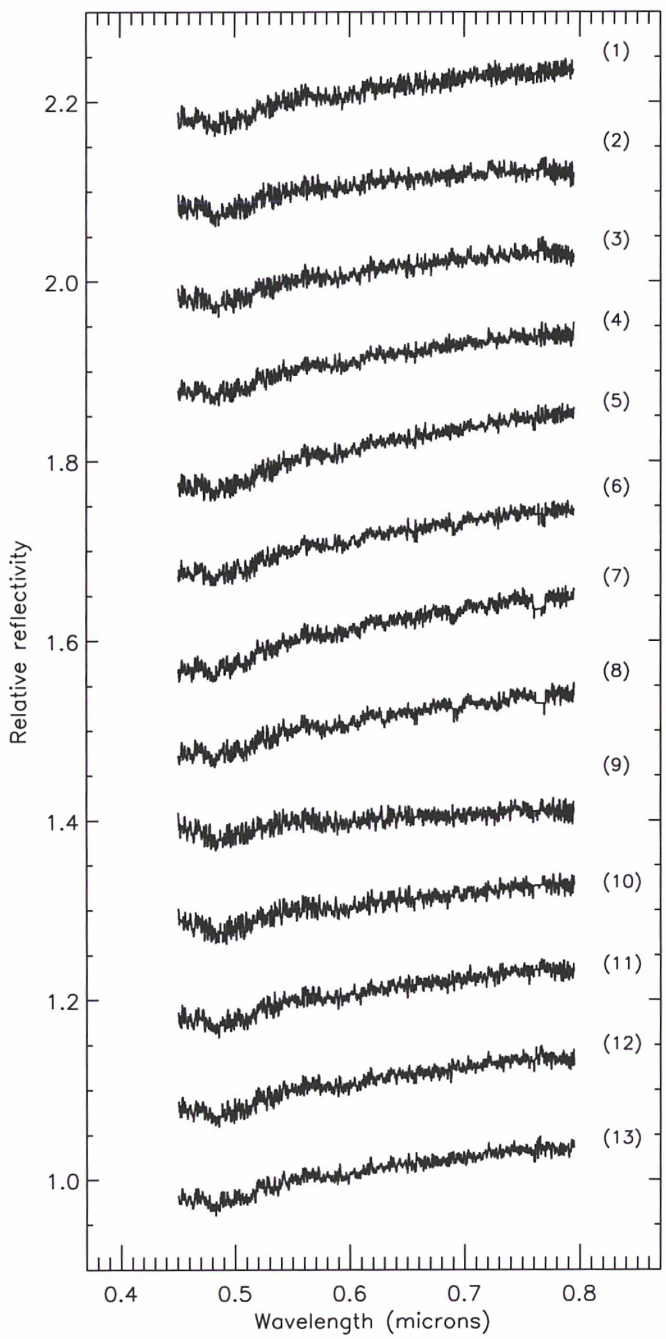

Figure 3.8 – Visible spectra of Lutetia normalized at 0.55 μm and shifted of 0.1 in reflectivity for clarity. From Perna et al. (2010b).

The band at ~ 0.6 μm was seen in one of the spectra published by Lazzarin et al. (2004) and it is generally attributed to charge transfer transitions in minerals produced by aqueous alteration of anhydrous silicates (Vilas et al. 1994), but can be also present on pyroxenes (e.g., Burns et al. 1976). The depth of the spectral features, relative to the continuum reflectance, is of about 1% in all the spectra, not exhibiting any evident variation. Conversely, as reported in Table 3.6 and shown in Fig. 3.9, the spectral slopes computed between 0.6 and 0.75 μm exhibit a periodic variation (in particular, a clear inhomogeneity emerges in correspondence with the spectrum # 9). This variation of the spectral slope of Lutetia through the rotational phase, can be interpreted as due to the presence of inhomogeneities on the observed portion of the asteroid surface. These inhomogeneities could be related to the chemical/mineralogical composition, as well as to the structure of the surface as the possible result of the presence of craters on the surface of Lutetia.

Considering the pole solution ($\lambda = 39°$, $\beta = 3°$) found by Torppa et al. (2003) and the cartesian coordinates vector of Lutetia with respect to the TNG site (retrieved from the JPL/HORIZONS system[2]), the aspect angle (Fig. 3.10) during the observations was measured as:

$$\xi = \arccos(|\vec{V}| \bullet |\vec{C}|) \tag{3.1}$$

where $|\vec{V}|$ is the unit vector of the pole of Lutetia, $|\vec{C}|$ is the unit vector of its cartesian position, and the symbol $\bullet$ indicates the dot product operation.

All the spectra were obtained at an aspect angle $\xi \sim 30°$, and are therefore referred to the same asteroid emisphere. On the basis of these results, it is possible to support the hypothesis formuled by Carvano et al. (2008) that one or more craters/inhomogeneities can be present on the surface of Lutetia (as shown in Fig. 3.9, these inhomogeneities could cover up to 20% of the surface of Lutetia).

These data are useful in the assessment of the physical nature of Lutetia, and will constitute a fundamental start up for the calibration, analysis and interpretation of the data acquired by the instruments onboard the Rosetta spacecraft.

[2]http://ssd.jpl.nasa.gov/horizons.cgi

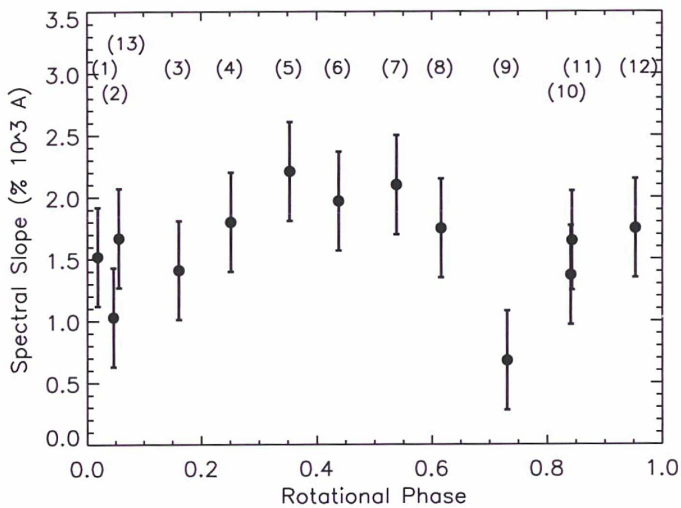

Figure 3.9 – Spectral slope vs. rotational phase of Lutetia, computed considering a rotational period of 8.165455 hours (Torppa et al. 2003). From Perna et al. (2010b).

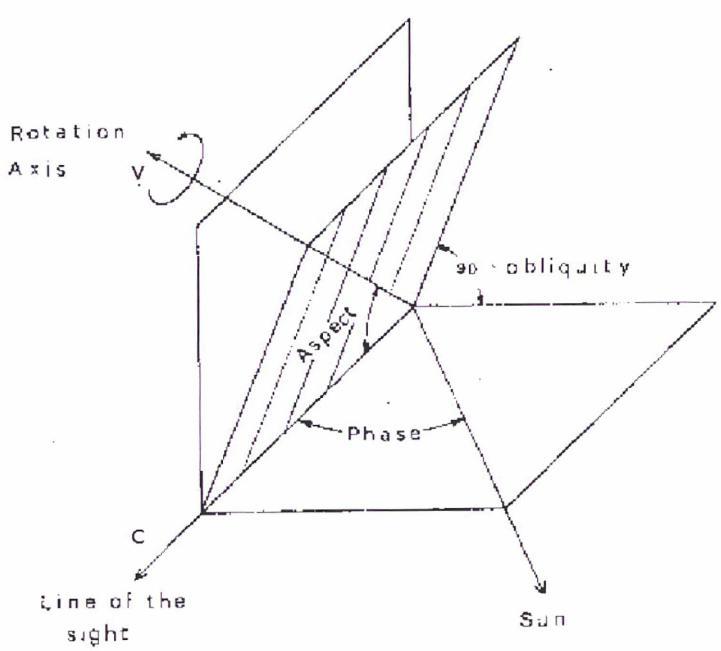

Figure 3.10 – Schematic illustration of viewing geometry for a Solar System body.

Chapter 4

Centaurs and TNOs

As already stated, Trans-Neptunian Objects and Centaurs are the most pristine remnants of the proto-planetary disk in which the accretion of the planetesimals occurred. Hence, their study is fundamental in the understanding of the conditions existing in the early Solar System, and of the accretion processes which governed the planetary formation at large heliocentric distances.

In October 2006, a two-year Large Programme started at ESO to study these bodies. During 500 hours of observation, data on 50 objects have been obtained using different techniques (spectroscopy, photometry, polarimetry).

As part of my PhD work, I contributed to the ESO-LP with:

- **Spectroscopy and modelling:** I carried out two observing runs (1 night each) at the VLT, acquiring 8 visible and 3 J-band spectra with the instruments FORS2 and ISAAC, respectively. I reduced most part of the ISAAC spectroscopic data obtained within the ESO-LP, and I contributed to the analysis and interpretation of the spectra.

- **Colors and taxonomy:** During the above-mentioned observing runs with FORS2 and ISAAC, I also acquired visible (8 objects, VRI filters) and NIR (6 objects, JHK_s filters) photometric data. I reduced most part of the NIR photometric data obtained in the framework of the ESO-LP, and I took in charge the analysis and interpretation of the whole V-NIR photometric dataset.

- **Light curves and densities:** I carried out two observing runs (3 nights each) at the NTT, acquiring the light curves of 12 Centaurs and TNOs with the EMMI instrument. I took in charge the reduction, the analysis, and the interpretation of the whole dataset.

4.1 Spectroscopy and modelling

As stated in section 1.2.2, the spectroscopic technique provides the most detailed information on the compositions of TNOs. In the visible and NIR spectral ranges, diagnostic features of silicate minerals, feldspar, carbonaceous assemblages, organics, and water-bearing minerals are present. Signatures of water ice are present at 1.5, 1.65, 2.0 μm, and signatures of other ices include those due to CH_4 around 1.7 and 2.3 μm, CH_3OH at 2.27 μm, and NH_3 at 2 and 2.25 μm, as well as solid C-N bearing material at 2.2 μm.

4.1.1 Observations and data reduction

During the ESO-LP, visible and NIR spectroscopy has been performed at the ESO-VLT (Paranal, Chile) within several runs between October 2006 and November 2008.

Low resolution ($\sim$ 200) visible spectroscopy was performed with the two FORS (FOcal Reducer and low dispersion Spectrograph) instruments (FORS1 until September 2007, FORS2 later on), and the obtained data were reduced according to the procedures described in section 2.2.1.

J-band (1.1-1.4 μm) spectroscopy was performed using ISAAC (Infrared Spectrometer And Array Camera) with a spectral resolution of about 500, while the $H + K$ grating of SINFONI (Spectrograph for INtegral Field Observations in the Near Infrared) was used to yield a spectral resolution of about 1500 over the 1.45-2.45 μm range. NIR spectra have been reduced as explained in section 2.2.2; each of them has been smoothed with a median filter technique to increase the signal-to-noise ratio, yielding a final resolution of 100-250 for both ISAAC and SINFONI data.

To combine visible and NIR spectra, photometric data are used. First, visible spectra are normalized at the V filter wavelength. Then the NIR spectra are scaled to the J, H, K_s magnitudes, transformed in reflectance using the following relation:

$$R_\lambda = 10^{-0.4[(M_\lambda - V) - (M_\lambda - V)_\odot]} \tag{4.1}$$

where $(M_\lambda - V)$ and $(M_\lambda - V)_\odot$ are the colors of the object and the Sun, respectively (λ is the central wavelength of the filter used to measure M_λ).

4.1.2 Visible spectra: features and slopes

Thirty-one spectra (Fig. 4.1) have been obtained for 28 bodies (6 classical, 5 resonant, 5 scattered and 2 detached TNOs, and 10 Centaurs), 15 of which were spectroscopically observed for the first time ever (Fornasier et al. 2009).

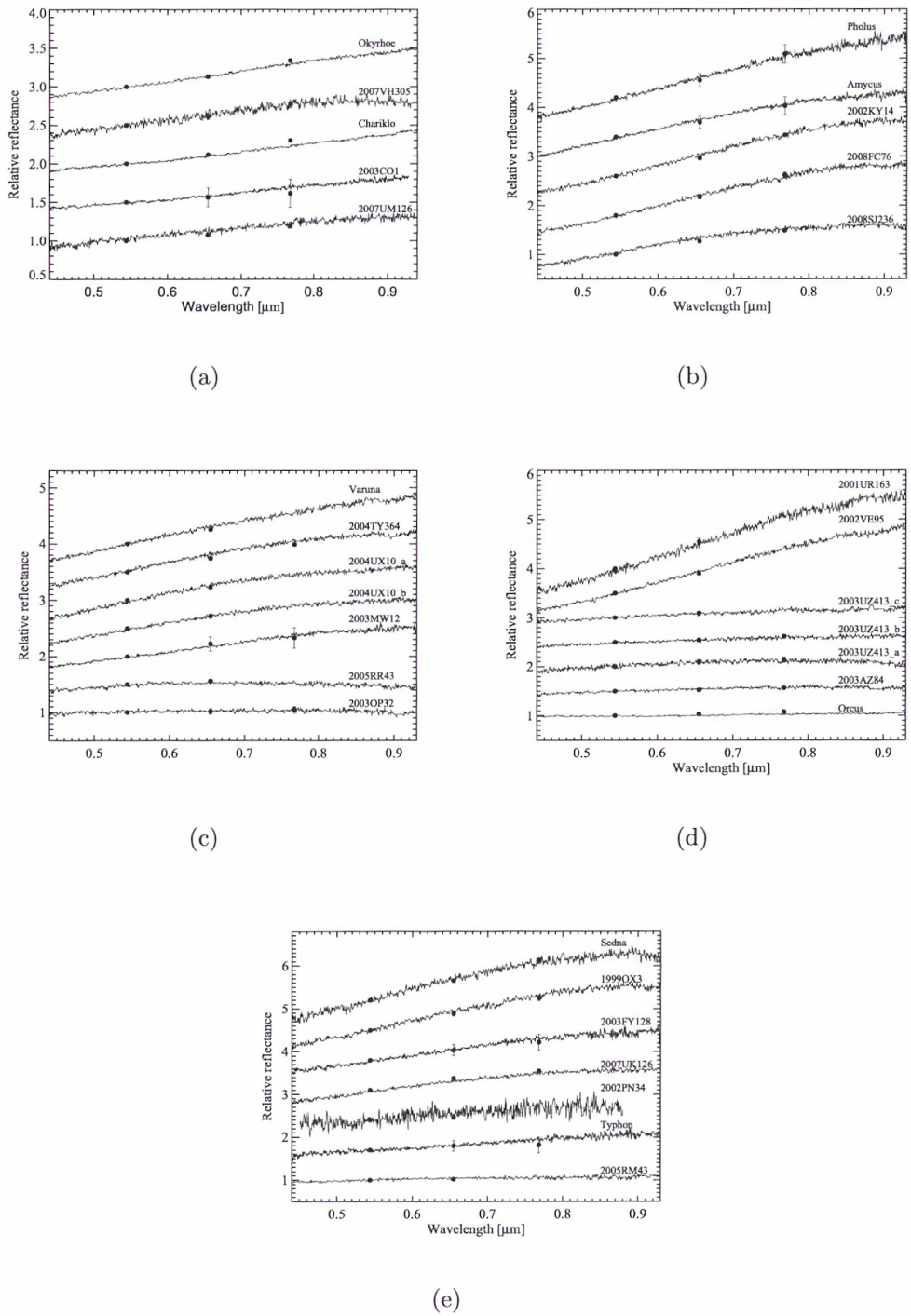

Figure 4.1 – Visible spectra of Centaurs (*a* and *b*), classical TNOs (*c*), resonant TNOs (*d*), and scattered and detached TNOs (*e*). Spectra are shifted for clarity. Color indices converted to spectral reflectance are also shown on each spectrum. From Fornasier et al. (2009).

The spectrum of the resonant TNO (208996) 2003 AZ_{84}, acquired in November 2008, appears featureless, while a weak band attributed to the presence of hydrated silicates, centered around 0.7 μm with a depth of about 3% and a width of more than 0.3 μm, was seen both on a spectrum acquired in January 2007 (Alvarez-Candal et al. 2008) and in a previous work by Fornasier et al. (2004). The three spectra after the continuum removal are plotted in Fig. 4.2: the November 2008 data do not show any absorption band, except for some residuals of the background removal (in particular the O_2 band around 0.76 μm and the water telluric bands around 0.72 μm and 0.83 μm). It is hence possible that 2003 AZ_{84} has an heterogeneous surface composition.

Also all of the other objects have featureless spectra, with the exceptions of (10199) Chariklo and (42355) Typhon, which show faint absorptions at 0.62-0.65 μm attributed to the presence of phyllosilicates (aqueously altered material) on their surfaces.

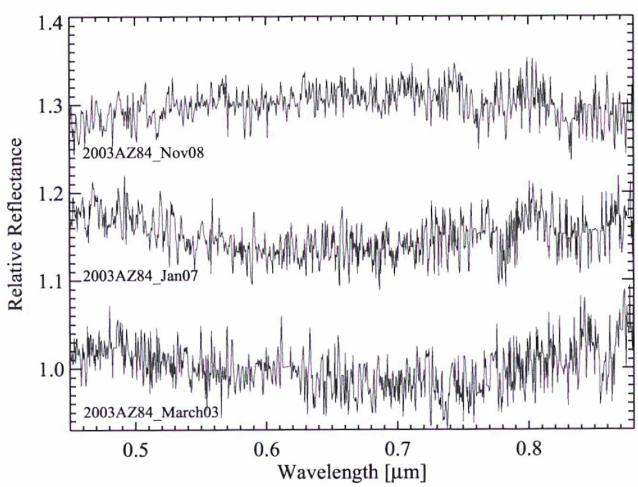

Figure 4.2 – Visible spectra of 2003 AZ_{84} taken during 3 different observing runs, after continuum slope removal. No indication of the band seen in the March 2003 and January 2007 data appears in the spectrum obtained on November 2008. From Fornasier et al. (2009).

Within the obtained results, the large variety in the spectral behaviour of both the Centaur and TNO populations emerged, since the spectral slopes span a wide range of colors, from gray to very red ($\sim$ 1 to 51 % / 10^3 Å).

For a better analysis of the visible spectral slope distribution, all the measurements available in the literature have been taken into account (Fornasier

et al. 2009, and references therein), for a total sample of 20 Centaurs and 53 TNOs (14 resonants, 29 classicals, 6 scattered, and 4 detached objects).

Resonant, scattered and detached TNOs, as well as Centaurs, have very similar spectral slopes, while it is evident that there is a lack of very red objects in the investigated classical TNOs (Fig. 4.3 and Table 4.1). Nevertheless, this lack could be due to an observational bias, since the red objects belong principally to the cold population, which presents smaller sizes than the bluer hot population (see section 1.1).

The bimodal distribution (Pholus-like and Chiron-like) suggested for Centaurs based on visible photometric colors (see section 1.1), does not clearly appear in the obtained spectral slope distribution, probably because of the limited dataset.

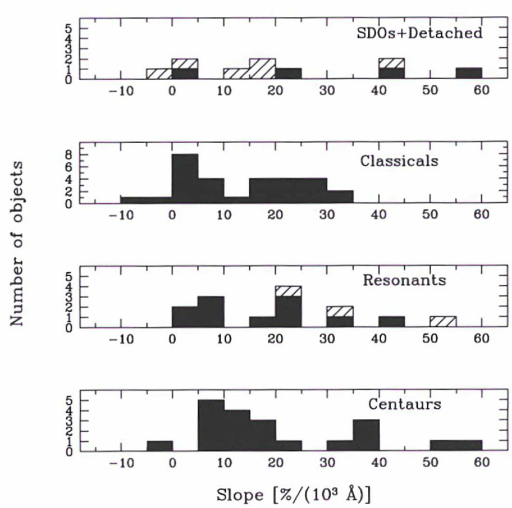

Figure 4.3 – Distribution of TNOs and Centaurs as a function of the spectral slope. From Fornasier et al. (2009).

Possible correlations have been searched between spectral slope values (S) and orbital elements (inclination i, eccentricity e, semimajor axis a, and perihelion q) or absolute magnitude H for the different dynamical classes (Fig. 4.4), computing the Spearman's (1904) rank correlation coefficient (ρ) and the two-sided significance (P_r) of its deviation from zero. The Spearman correlation coefficient is defined as the Pearson correlation coefficient between the ranked (i.e., magnitude-sorted) variables. The Pearson correlation coefficient between two variables is, in turn, defined as the covariance of the two variables divided by the product of their standard deviations. Hence:

Table 4.1 – Mean spectral slope values and standand deviation of TNOs and Centaurs.

Class	Mean slope (% / 10^3Å)	Std deviation (% / 10^3Å)
Centaurs	20.5	15.1
Classicals	13.8	12.1
Resonants	20.8	15.6
SDOs & Detached	21.1	18.3
All TNOs & Centaurs	17.9	14.8

$$\rho = \frac{\sum_{i=1}^{n}(x_i - \bar{x})(y_i - \bar{y})}{\sqrt{\sum_{i=1}^{n}(x_i - \bar{x})^2 \sum_{i=1}^{n}(y_i - \bar{y})^2}} \tag{4.2}$$

where x_i and y_i represent the magnitude-based ranks among slope and the other quantity, respectively. Elements of identical magnitude are ranked using a rank equal to the mean of the ranks that would otherwise be assigned. The value of ρ varies between -1 and 1: if it is close to zero this means no correlation, if $|\rho|$ is close to 1 then a correlation exists. To test whether an observed value of ρ is significantly different from zero, it is possible to calculate the probability that it would be greater than or equal to the observed value, given the null hypothesis, by using a permutation test. The significance is hence a value in the interval $0 < P_r < 1$, and a small value indicates a significant correlation. Correlations with $|\rho| > 0.5$ and $P_r < 0.02$ are considered particularly important. The results are summarized in Table 4.2.

Classical TNOs present an anticorrelation between S and i, with lower slope values with increasing inclination (as expected, because of the mentioned cold and hot populations, see section 1.1) is found. Nevertheless, considering only the 7 objects with $i < 10.4°$, there is no correlation between S and i ($\rho = 0.198206$ and $P_r = 0.993299$), in agreement with the result by Peixinho et al. (2008), who found that the optical colors of classical objects are independent of inclination below $i \sim 12°$. A weaker anticorrelation between S and e is also found for classical TNOs.

Resonant TNOs present a correlation between S and e, with high-e objects redder than those with low eccentricities. Excluding the 3 "non-plutinos" objects, the correlation becomes weaker ($\rho = 0.681818$ and $P_r = 0.020843$).

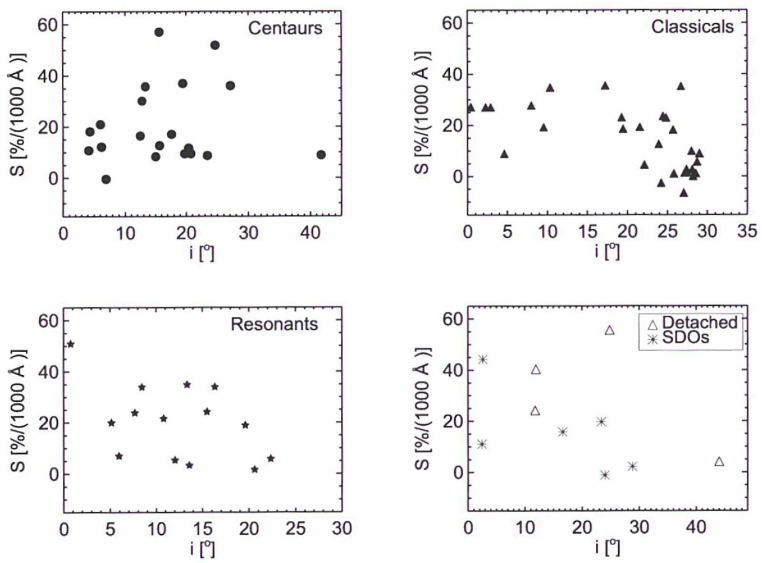

(a)

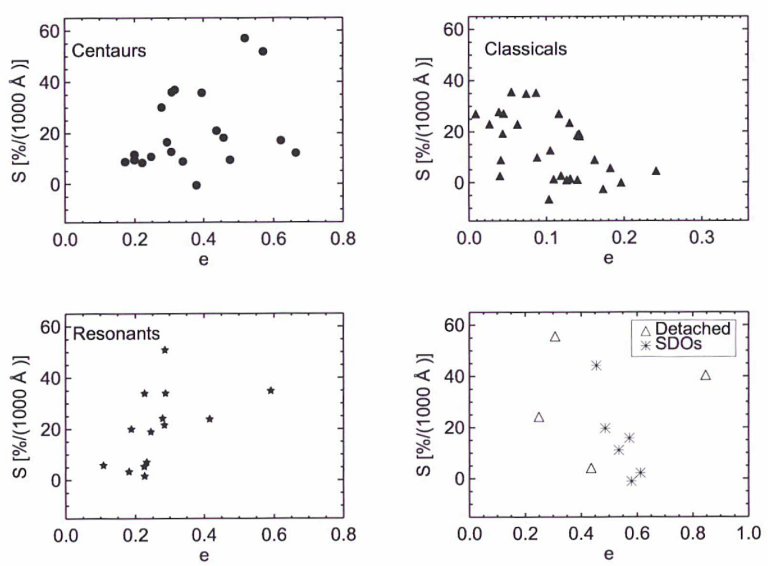

(b)

Figure 4.4 – *(a)* Spectral slope versus orbital inclination for Centaurs and TNOs. *(b)* Spectral slope versus orbital eccentricity for Centaurs and TNOs. From Fornasier et al. (2009).

Table 4.2 – Computed Spearman correlations between spectral slope and orbital elements (i, e, a, q) or absolute magnitude H of Centaurs and TNOs. From Fornasier et al. (2009).

Class	ρ	P_r	n
Centaurs			
S vs i	-0.00451293	0.98495	20
S vs e	0.430989	0.0578041	20
S vs a	0.0691989	0.771903	20
S vs H	0.398494	0.0818076	20
S vs q	-0.0910117	0.702757	20
Classicals			
S vs i	**-0.641537**	**0.000176407**	**29**
S vs e	**-0.510963**	**0.00461781**	**29**
S vs a	-0.109633	0.571303	29
S vs H	-0.0892836	0.64510	29
S vs q	0.430648	0.0196961	29
Resonants			
S vs i	-0.393407	0.164032	14
S vs e	**0.767033**	**0.00136768**	**14**
S vs a	0.560440	0.0371045	14
S vs H	0.382838	0.176678	14
S vs q	0.142857	0.626118	14
SDOs			
S vs i	-0.542857	0.265703	6
S vs e	**-0.885714**	**0.0188455**	**6**
S vs a	-0.657143	0.156175	6
S vs H	0.0857143	0.871743	6
S vs q	-0.0857143	0.871743	6
Detached Objs			
S vs i	-0.200000	0.800000	4
S vs e	0.00000	1.00000	4
S vs a	-0.400000	0.600000	4
S vs H	0.800000	0.200000	4
S vs q	-0.400000	0.600000	4

NOTE: n is the number of objects used in the statistical analysis. Strongest correlations are in bold.

The stronger trend is found for scattered TNOs, which show an anticorrelation between S and e, with lower slope values with increasing eccentricity. The sample (6 objects) is too small to be statistically significant, nevertheless this strong correlation was also found by Santos-Sanz et al. (2009) on a larger sample (25) of SDOs, on the basis of $BVRI$ photometry.

Interestingly, in opposition to this $S - e$ anticorrelation for SDOs, Centaurs and Plutinos present both a positive $S - e$ correlation. This could strengthen the results by Peixinho et al. (2004), who found, using $BVRI$ photometric data, that color-color correlations for Centaurs show some resemblance to those of Plutinos, in opposition to those of SDOs. As stated by the same authors, transfer mechanisms of Centaurs from the trans-Neptunian regions are not well understood, with SDOs and Plutinos as the best candidates for such expulsions. However the verification of these color similarities might suggest that Centaurs are in effect mainly originated from the Plutino population, and that surface changing agents do not differ significantly between Centaurs and Plutinos.

4.1.3 Modelling: the case of (50000) Quaoar

After connecting J and $H + K$ spectra to visible data through the contextually obtained V-NIR photometry, the surface properties of the observed objects have been investigated using the radiative transfer models of Hapke (1981, 1993) and Shkuratov et al. (1999). Part of the data are still under analysis, and detailed modelling of (26375) 1999 DE_9, (28978) Ixion, (55565) 2002 AW_{197}, (60558) Echeclus, (120132) 2003 FY_{128}, and (208996) 2003 AZ_{84} is presently ongoing (Merlin et al. 2010).

Hereafter I will describe the case of (50000) Quaoar as an example of the results which can be obtained with this approach (Dalle Ore et al. 2009).

Observational data

The ground-based $VRJHK_s$ photometry and visible, J, $H+K$ spectroscopy obtained in the framework of the ESO-LP have been complemented and extended to longer wavelengths with broadband photometric measurements (3.6 and 4.5 μm, two exposures each) from the InfraRed Array Camera (IRAC) onboard the Spitzer Space Telescope.

Initial constraints

The spectrum of Quaoar is rich of absorption bands which constitute a strong basis to model its surface.

H_2O presence is clearly indicated by its bands at 1.5 and 2.0 μm (Jewitt & Luu 2004; Schaller & Brown 2007a), with also the distinctive feature at

1.65 μm revealing that at least a significant portion of the H_2O is in the crystalline (as opposed to amorphous) phase (Grundy & Schmitt 1998).

Several weaker absorptions at 1.72, 2.32, and 2.38 μm strongly suggest the presence of CH_4 ice (Schaller & Brown 2007a).

The red (up to $\simeq$ 1.3 μm) spectrum of Quaoar (Jewitt & Luu 2004, and references therein), can be explained only by the presence of complex organic material (Cruikshank et al. 2005, and references therein).

Weak features between 2.3 and 2.35μm have been tentatively attributed to ethane or other light hydrocarbons by Schaller & Brown (2007a), while NH_4OH has been suggested by Jewitt & Luu (2004) to explain a weak feature at 2.2 μm.

Modelling

The combined spectrum of Quaoar has been scaled to the visual geometric albedo of $19.86^{+13.17}_{-7.04}$% measured by Stansberry et al. (2008), then modeled by means of a code based on the Shkuratov et al. (1999) radiative transfer formulation.

Input parameters are the relative amounts, grain size and optical constants of each candidate component, which are listed in Table 4.3 (where the laboratory sources of the used optical constants are also reported).

Beside those listed, a few further materials were tested, including minerals (olivine, pyroxene, NaCl) as well as alternative reddening materials (polyHCN) and ices (NH_3), but their presence did not reflect a better fit of the observational data.

For what concerns grain sizes, an initial assumption was made based on the strength of features at visible wavelengths for those materials that have some, and estimated to be comparable for the other components (N_2 represented the only exception, since this ice requires very long path lengths to produce detectable absorptions).

Multidimensional minimization of the root mean squared (RMS) difference between tentative models and observed data has been performed using the Nelder-Mead (1965) technique. The used routine allowed to assign weights (in the range 0 - 1) to different parts of the spectrum. The best fit and its variations were all computed giving higher weight to the $\lambda < 2.5\mu$m region, therefore forcing the program to converge to a good fit where bands as well as albedo height both contributed to constrain the solution. When equal weight was given to the entire wavelength range, the overall fit resulted poorer but still maintained the same components, confirming the need for the fairly large number of materials that constitute the best-fit model.

It is noteworthy to remember that such models do not claim to be unique,

Table 4.3 – Best fitting model, model without N_2, and model with 10% N_2 for (50000) Quaoar. From Dalle Ore et al. (2009).

	Best Model	No N_2 model	10% N_2 model	Reference[e]
RMS [a]	1.1×10^{-4}	1.8×10^{-4}	1.6×10^{-4}	–
Titan tholin [b]	0.12	0.09	0.11	(1)
Triton tholin [b]	0.06	0.05	0.04	(2)
Triton tholin [c]	0.03	0.05	0.04	(2)
H_2O amorph (40K) [d]	0.18(1.3 μm)	0.29(1.5 μm)	0.22(1.8 μm)	(3)
Titan tholin [d]	0.13(11.2 μm)	0.14(11.8 μm)	0.13(12.0 μm)	(1)
H_2O cryst (40K) [d]	0.18(14.6 μm)	0.24(11.0 μm)	0.23(11.4 μm)	(3)
C_2H_6 [d]	0.04(6.5 μm)	0.04(8.4 μm)	0.04(8.8 μm)	(4)
Triton tholin [d]	0.14(7.4 μm)	0.15(6.8 μm)	0.14(7.6 μm)	(2)
N_2 (36-60K) [d]	0.20(16.1 mm)	0(16.0 mm)	0.1(15.8 mm)	(5)
CH_4 (30-35K) [d]	0.13(9.4 μm)	0.14(7.1 μm)	0.16(8.4 μm)	(6),(7)

NOTE: All models were computed with a porosity of 0.1.
[a] RMS error of each model when compared to the data.
[b] Material mixed as inclusions in CH_4 ice.
[c] Material mixed as inclusions in crystalline H_2O ice.
[d] Material mixed intimately, with grain size in parenthesis. Temperature listed after the name of the component.
[e] References: (1) Imanaka et al. (2005); (2) Khare et al. (1994); (3) Mastrapa & Sandford (2008); (4) Mastrapa (private comm.); (5) Green et al. (1991); (6) Grundy et al. (2002); (7) Hudgins et al. (1993).

since many of the parameters (optical costants, temperature and dilution of molecules in a matrix, etc.) are not well established or completely unknown. Moreover, mixtures with different grain sizes or different mixing ratios of the constituents can give very similar fits to the data. Nevertheless, the used models are generally able to describe the spectral properties of the analyzed objects quite well, and to put strong constraints on their surface composition.

The best model

The best fitting (details in Table 4.3) for the spectrum of Quaoar consists of an intimate mixture of crystalline and amorphous H_2O, CH_4, N_2, and C_2H_6 ice, and of Triton and Titan tholins. Both crystalline H_2O and CH_4 ice are contaminated molecularly by Triton and Titan tholins as well.

Starting with a mix of crystalline H_2O and CH_4 ices with reddening materials (tholins), a satisfactory fit was obtained up to 2.5μm, but caused the model to be too dark at the wavelengths of the Spitzer/IRAC bands by about 40%. Several attempts have been made to raise the albedo in this region, using a variety of materials, but they resulted in poor fits at shorter wavelengths. The best fitting model was obtained introducing amorphous H_2O

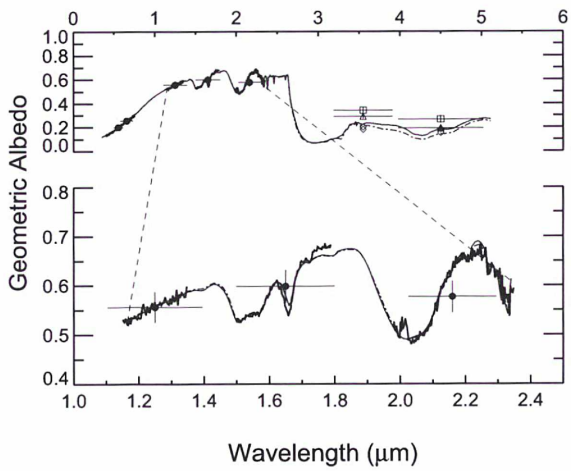

Figure 4.5 – Best fitting model (solid line) for Quaoar, compared to a model computed with the same components except amorphous H_2O (dot-dashed line). Open diamonds show the model convolved to the Spitzer filter response functions. Open triangles mark the first Spitzer exposure, open squares indicate the second. From Dalle Ore et al. (2009).

(brighter than crystalline H_2O ice at the IRAC wavelengths) in extremely small grains ($\sim$ 1 μm), improving the fit by about 20% at 4.5μm. Fig. 4.5 shows both the best model (solid line) and the same fit calculated with no amorphous H_2O ice (dot-dashed line).

Molecular nitrogen has been included in the model, despite of the fact that this component had never been detected on Quaoar before. N_2 ice improves the fit at 2.149 μm (Fig. 4.6), and also increases the albedo at 3.6 μm. Since the absorption bands of N_2 ice are intrinsically weak, this material could be present in relatively large amounts and escape direct spectroscopic detection.

Moreover, based on previous works suggesting that NH_4OH and C_2H_6 might be present on the surface of Quaoar (Jewitt & Luu 2004; Schaller & Brown 2007a), these have been introduced among the tentative components. While the presence of NH_4OH resulted to be unnecessary, a small amount of C_2H_6 improves the fit to the small absorption at $\simeq$ 2.27μm as shown in Fig. 4.7.

These results permit to put strong constraints on the surface composition of (50000) Quaoar, one of the largest TNOs with its diameter of 1260 $\pm$ 190 km (Brown & Trujillo 2004). In particular, the unexpected abundance of the

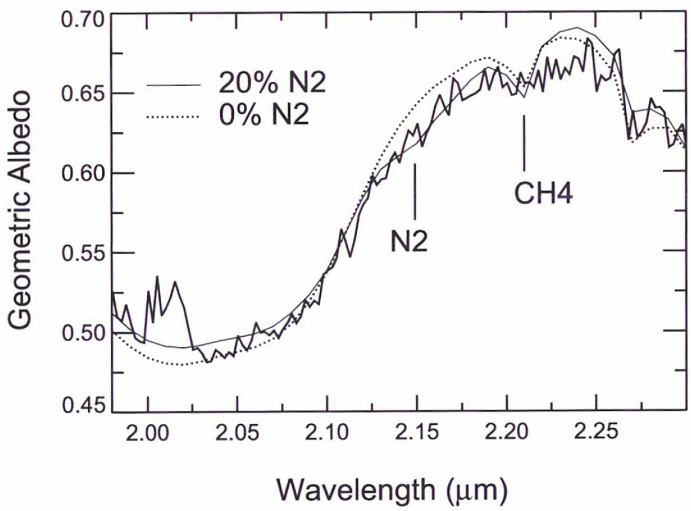

Figure 4.6 – Best fit (solid line) for Quaoar, and fit without N_2 (dotted line). The fit at 2.149 μm is moderately improved by the presence of 20% N_2 ice. From Dalle Ore et al. (2009).

highly volatile N_2 makes this object peculiar, in this sense similar to Pluto and Triton. Quaoar's spectrum is however dominated by H_2O ice, while CH_4 is the major absorber in the spectra of Pluto and Triton. Schaller & Brown (2007b) have shown that Quaoar's temperature and size put this object in a transition region between complete volatile loss and possible volatile retention. Its reduced capability to retain very volatile species (compared to the larger Pluto and Triton) could have led to a stronger presence of the H_2O ice, less volatile than CH_4.

It has to be noted that also the best fitting model is too dark at the Spitzer wavelengths, mainly because of the very absorbing crystalline H_2O ice. A possible solution could be found assuming a thin layer of amorphous H_2O ice covering the coarse mixture of the other components. This layer could be due to the irradiation of the underneath crystalline water ice, but further laboratory experiments on ices and more developed spectral models are needed to test this hypothesis.

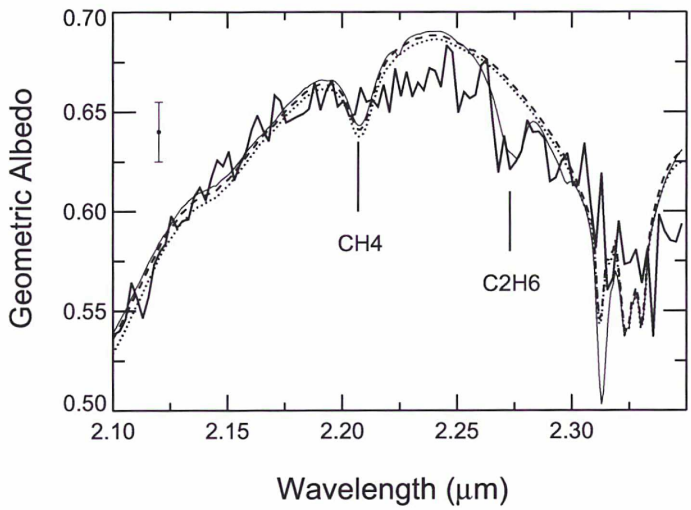

Figure 4.7 – Detail of the best fit for Quaoar (solid line), a fit without C_2H_6 (dashed), and a fit with NH_4OH in place of C_2H_6 (dotted). There is some evidence for C_2H_6 as shown by the fit to the 2.275μm band. NH_4OH on the other hand does not seem to contribute significantly (at this low concentration). From Dalle Ore et al. (2009).

4.2 Colors and taxonomy

Because of the faintness of Trans-Neptunian Objects and Centaurs, spectroscopic observations (which could provide the most detailed information about their surface compositions) are feasible only for a small number of them, even when using the largest ground-based telescopes (see Barucci et al. 2008a, for a recent review). Hence photometry is still the best tool to investigate the surface properties of a significant sample of these objects, allowing a global view of the whole known population.

Photometric surveys before the ESO-LP have observed about 200 objects. Statistical analyses were performed to search for possible correlations between colors and physical and orbital parameters (for recent reviews, see Doressoundiram et al. 2008; Tegler et al. 2008). As the major result, a clustering of "cold" (low eccentricity, low inclination) classical TNOs with very red colors was found (see section 1.1).

4.2.1 Observations and data reduction

In the framework of the ESO-LP, visible and NIR photometry of TNOs and Centaurs has been performed at the ESO-VLT (Paranal, Chile). The data have been acquired during several observing runs, between October 2006 and November 2008. The observational circumstances are reported in Table 4.4.

Visible photometry was performed with the two FORS instruments, using the broadband B, V, R, I filters, centered at 0.429, 0.554, 0.655 (or 0.657 in FORS2), and 0.768 μm, respectively.

NIR photometry was performed using the ISAAC instrument, with the J, H, Ks filters (central wavelength of 1.25, 1.65, and 2.16 μm, respectively).

The images were reduced using the procedures described in sections 2.1.1 and 2.1.2.

4.2.2 Results

Visible and NIR photometric measurements have been obtained for 45 objects, 19 of them have their colors reported for the first time ever.

Tables 4.5 and 4.6 list the resulting magnitude values, as well as the computed absolute magnitudes H of the targets, calculated as

$$H = V - 5\log(r\Delta) - \alpha\beta, \tag{4.3}$$

where V represents the visible magnitude, Δ, r and α are the topocentric and heliocentric distances and the phase angle, respectively, and β is the phase curve slope (the term $\alpha\beta$ is the correction for the opposition effect, e.g. Doressoundiram et al. 2008). For TNOs, it was assumed $\beta = 0.14 \pm 0.03$ mag/deg, the modal value of the measurements published by Sheppard & Jewitt (2002). For Centaurs and Jupiter-coupled objects, it was assumed $\beta = 0.11 \pm 0.01$ mag/deg, the result of a least squares fit by Doressoundiram et al. (2005) of the linear phase function $\phi(\alpha) = 10^{-\alpha\beta}$ of data from Bauer et al. (2003).

On the basis of the obtained color indices, the taxonomic classification of the targets was derived via the G-mode statistical method presented in Fulchignoni et al. (2000), using the taxonomy for TNOs and Centaurs introduced by Barucci et al. (2005a). As said in section 1.4.1, this taxonomy identifies four classes, that reasonably indicate different composition and/or evolutional history, with increasingly red colors: BB (neutral colors with respect to the Sun), BR, IR, RR (very red colors). The above-mentioned algorithm was applied to objects for which two or more color indices were available (i.e., to 41 out of the 45 observed TNOs and Centaurs).

Table 4.4 – Observational circumstances for Centaurs and TNOs whose colors have been obtained in the framework of the ESO-LP.

Object	Date	Δ (AU)	r (AU)	α (deg)
(5145) Pholus	12 Apr 2008	21.212	21.864	2.0
(10199) Chariklo	20 Mar 2007	12.496	13.276	2.8
	3 Feb 2008	13.311	13.395	4.2
	4 Feb 2008	13.296	13.395	4.2
(20000) Varuna	4 Dec 2007	42.605	43.391	0.8
(26375) 1999 DE_9	22 Jan 2007	34.767	35.435	1.2
(28978) Ixion	15 Jul 2007	41.241	42.019	0.9
(32532) Thereus	19 Sep 2007	10.345	11.006	4.1
(42301) 2001 UR_{163}	5 Dec 2007	49.625	50.308	0.8
(42355) Typhon	24 Jan 2007	16.713	17.542	1.8
	12 Apr 2008	16.892	17.650	2.2
(44594) 1999 OX_3	21 Sep 2008	22.025	22.889	1.3
	22 Sep 2008	22.033	22.888	1.3
(47171) 1999 TC_{36}	9 Nov 2006	29.988	30.820	1.0
(47932) 2000 GN_{171}	23 Jan 2007	28.378	28.352	2.0
	24 Mar 2007	27.492	28.345	1.1
(50000) Quaoar	15 Jul 2007	42.449	43.267	0.8
(52872) Okyrhoe	3 Feb 2008	4.883	5.800	3.9
	4 Feb 2008	4.877	5.800	3.7
(54598) Bienor	18 Sep 2007	17.127	18.116	0.6
(55565) 2002 AW_{197}	23 Jan 2007	45.860	46.796	0.4
(55576) Amycus	12 Apr 2008	15.205	16.056	1.9
(55637) 2002 UX_{25}	18 Sep 2007	41.188	42.004	0.8
	6 Dec 2007	41.263	41.975	0.9
(55638) 2002 VE_{95}	5 Dec 2007	27.297	28.248	0.5
	6 Dec 2007	27.301	28.249	0.6
	22 Nov 2008	27.379	28.341	0.5
	23 Nov 2008	27.378	28.341	0.4
(60558) Echeclus	14 May 2007	11.239	12.124	2.4
(73480) 2002 PN_{34}	10 Nov 2007	14.894	15.344	3.3
(83982) Crantor	14 Jul 2007	14.007	14.739	2.8
(90377) Sedna	21 Sep 2008	87.416	88.015	0.5
	22 Sep 2008	87.402	88.014	0.5
(90482) Orcus	3 Feb 2008	46.904	47.807	0.5
	4 Feb 2008	46.900	47.807	0.5
(90568) 2004 GV_9	13 May 2007	38.141	39.069	0.6
(119951) 2002 KX_{14}	13 Jul 2007	38.855	39.535	1.1
(120061) 2003 CO_1	4 Feb 2008	10.937	11.080	5.1
	12 Apr 2008	10.179	11.123	1.8
	13 Apr 2008	10.175	11.123	1.8
(120132) 2003 FY_{128}	22 Jan 2007	37.935	38.298	1.4
	12 Apr 2008	37.477	38.454	0.3
(120178) 2003 OP_{32}	21 Sep 2008	40.546	41.365	0.8
(120348) 2004 TY_{364}	22 Nov 2008	38.840	39.591	0.9
	23 Nov 2008	38.849	39.591	1.0
(136199) Eris	20 Oct 2006	95.837	96.798	0.2
	19 Sep 2007	95.923	96.803	0.3
	7 Dec 2007	96.226	96.792	0.5
(144897) 2004 UX_{10}	4 Dec 2007	38.145	38.837	1.0
	5 Dec 2007	38.158	38.837	1.1
	6 Dec 2007	38.170	38.837	1.1
	23 Nov 2008	38.059	38.879	0.8
(145451) 2005 RM_{43}	19 Sep 2007	34.670	35.183	1.4
	4 Dec 2007	34.298	35.195	0.7
	7 Dec 2007	34.316	35.196	0.7
(145452) 2005 RN_{43}	19 Sep 2007	39.837	40.714	0.7
(145453) 2005 RR_{43}	18 Sep 2007	37.982	38.492	1.3
	4 Dec 2007	37.623	38.511	0.6
	7 Dec 2007	37.642	38.512	0.7
(174567) 2003 MW_{12}	12 Apr 2008	47.314	47.968	0.9
	13 Apr 2008	47.302	47.968	0.9
(208996) 2003 AZ_{84}	24 Jan 2007	44.653	45.604	0.3
	22 Nov 2008	44.879	45.458	1.0
	23 Nov 2008	44.865	45.457	1.0
2002 KY_{14}	21 Sep 2008	7.802	8.649	3.8
	22 Sep 2008	7.810	8.649	3.8
2003 QW_{90}	9 Nov 2006	43.426	44.156	0.9
2003 UZ_{117}	25 Dec 2006	38.756	39.439	1.0
	22 Nov 2008	38.420	39.368	0.4
	23 Nov 2008	38.423	39.367	0.4
2003 UZ_{413}	4 Dec 2007	41.171	42.004	0.7
	21 Sep 2008	41.466	42.163	1.0
	22 Nov 2008	41.276	42.197	0.5
	23 Nov 2008	41.282	42.198	0.5
2007 UK_{126}	21 Sep 2008	45.131	45.618	1.1
	22 Sep 2008	45.117	45.617	1.1
2007 UM_{126}	21 Sep 2008	10.202	11.163	1.5
	22 Sep 2008	10.199	11.165	1.5
2007 VH_{305}	22 Nov 2008	7.854	8.638	4.2
	23 Nov 2008	7.863	8.636	4.3
2008 FC_{76}	20 Sep 2008	10.968	11.690	3.5
	21 Sep 2008	10.976	11.688	3.6
2008 SJ_{236}	22 Nov 2008	5.522	6.364	5.0
	23 Nov 2008	5.530	6.363	5.1

NOTE: Δ, r and α are the topocentric distance, the heliocentric distance, and the phase angle, respectively.

Table 4.5 – Observed magnitudes, first year of the ESO-LP (October 2006 - September 2007). From DeMeo et al. (2009b).

Object	Date	UT_{START}	B	V	R	I	J	H	K_s	H_V
(10199) Chariklo	20 Mar 2007	03:22	...	18.49±0.05	18.04±0.07	...	17.00±0.05	16.51±0.06	16.30±0.06	7.09±0.05
(26375) 1999 DE_9	22 Jan 2007	05:48	...	20.75±0.04	20.13±0.02	19.63±0.02	19.22±0.06	18.93±0.07	18.87±0.07	5.13±0.05
(28978) Ixion	15 Jul 2007	02:47	...	20.22±0.05	19.67±0.06	...	18.63±0.04	18.37±0.05	18.38±0.05	3.90±0.06
(32532) Thereus	19 Sep 2007	06:44	20.71±0.05	19.90±0.03	...	19.00±0.13	18.55±0.04	18.15±0.06	18.04±0.06	9.18±0.03
(42355) Typhon	24 Jan 2007	05:33	...	20.34±0.02	19.87±0.02	19.41±0.02	18.78±0.04	18.33±0.05	18.17±0.05	7.75±0.04
	24 Jan 2007	05:46	...	20.36±0.02	19.88±0.02	19.41±0.02	...	...	...	7.77±0.04
(47171) 1999 TC_{36}	9 Nov 2006	00:58	...	20.25±0.03	...	19.00±0.03	18.17±0.07	17.85±0.07	17.79±0.08	5.25±0.04
	9 Nov 2006	01:09	...	20.26±0.03	...	19.00±0.03	...	...	...	5.26±0.04
(47932) 2000 GN_{171}	23 Jan 2007	07:06	...	21.01±0.03	20.42±0.02	19.91±0.02	19.43±0.08	19.09±0.09	...	6.20±0.04
	23 Jan 2007	07:15	...	21.04±0.03	20.42±0.02	19.90±0.02	...	...	...	6.23±0.04
	24 Jan 2007	07:17	...	21.11±0.03	20.54±0.02	19.99±0.02	19.42±0.06	19.04±0.07	18.98±0.07	6.30±0.04
	24 Jan 2007	07:26	...	21.12±0.03	20.54±0.02	20.00±0.02	...	...	...	6.31±0.04
	24 Mar 2007	05:12	...	21.30±0.06	20.73±0.08	...	...	...	...	6.69±0.07
*(50000) Quaoar	15 Jul 2007	01:33	...	19.25±0.05	18.65±0.05	...	17.07±0.03	16.71±0.04	16.68±0.04	2.82±0.06
(54598) Bienor	18 Sep 2007	04:05	20.71±0.05	19.98±0.03	...	19.05±0.16	18.46±0.05	18.09±0.05	...	7.46±0.03
(55565) 2002 AW_{197}	23 Jan 2007	05:13	...	20.36±0.02	19.76±0.02	19.21±0.02	18.62±0.05	18.28±0.06	18.21±0.06	3.65±0.04
	23 Jan 2007	05:25	...	20.37±0.02	19.76±0.02	19.21±0.02	...	...	...	3.66±0.04
(55637) 2002 UX_{25}	18 Sep 2007	06:50	21.31±0.23	20.28±0.06	...	19.12±0.34	...	...	...	3.98±0.07
(60558) Echeclus	14 May 2007	00:51	...	20.61±0.06	20.12±0.07	...	19.13±0.04	18.76±0.06	18.42±0.09	9.67±0.06
(83982) Crantor	14 Jul 2007	01:32	...	21.00±0.07	20.27±0.08	...	...	...	...	9.12±0.07
	16 Jul 2007	01:03	...	20.91±0.02	20.17±0.03	...	...	...	...	9.01±0.02
*(90568) 2004 GV_9	13 May 2007	02:14	...	20.20±0.03	19.64±0.03	...	18.63±0.05	18.29±0.08	18.15±0.05	4.25±0.04
*(119951) 2002 KX_{14}	13 Jul 2007	01:29	...	20.95±0.08	20.34±0.04	...	...	...	...	4.86±0.09
*(120132) 2003 FY_{128}	22 Jan 2007	06:49	...	21.06±0.03	20.47±0.02	19.91±0.02	19.42±0.05	19.06±0.06	18.95±0.06	5.05±0.04
	22 Jan 2007	07:01	...	21.06±0.03	20.47±0.02	19.91±0.02	...	...	...	5.05±0.04
(136199) Eris	19 Sep 2007	05:24	19.59±0.06	18.74±0.04	...	18.01±0.12	17.96±0.04	17.88±0.06	18.16±0.06	-1.14±0.05
	20 Oct 2006	04:24	...	18.74±0.02	...	18.00±0.02	17.79±0.08	...	...	-1.13±0.04
	20 Oct 2006	05:49	...	18.75±0.02	...	17.99±0.02	...	...	...	-1.12±0.04
*(145451) 2005 RM_{43}	19 Sep 2007	09:17	20.88±0.06	20.18±0.03	...	19.48±0.18	19.27±0.06	19.07±0.06	18.79±0.07	4.55±0.04
*(145452) 2005 RN_{43}	19 Sep 2007	03:23	21.05±0.07	20.02±0.03	...	18.89±0.21	18.47±0.05	18.16±0.05	17.97±0.05	3.87±0.04
	19 Sep 2007	04:04	...	...	...	...	18.39±0.05	...	...	...
*(145453) 2005 RR_{43}	18 Sep 2007	06:50	20.79±0.12	20.08±0.03	...	19.32±0.16	19.06±0.06	...	...	4.07±0.04
	18 Sep 2007	07:33	...	...	...	...	19.12±0.06	...	...	...
(208996) 2003 AZ_{84}	24 Jan 2007	03:38	...	20.33±0.02	19.93±0.02	19.60±0.02	19.12±0.05	18.81±0.05	18.75±0.05	3.74±0.04
	24 Jan 2007	03:47	...	20.33±0.02	19.94±0.02	19.60±0.02	...	...	...	3.74±0.04
*2003 QW_{90}	9 Nov 2006	02:19	...	21.80±0.06	...	20.69±0.05	19.87±0.15	...	...	5.25±0.07
	9 Nov 2006	02:45	...	21.82±0.06	...	20.69±0.05	...	...	...	5.27±0.07
*2003 UZ_{117}	25 Dec 2006	01:02	...	21.25±0.04	...	20.58±0.03	...	...	...	5.16±0.05
	25 Dec 2006	02:18	...	21.26±0.04	...	20.59±0.04	...	...	...	5.17±0.05

* Objects that had their colors reported for the first time ever.

Table 4.6 – Observed magnitudes, second year of the ESO-LP (November 2007 - November 2008). From Perna et al. (2010a), and references therein.

Object	Date	UT_{START}	V	R	I	J	H	K_s	H_V
(5145) Pholus	12 Apr 2008	05:48	21.33 ± 0.09	20.64 ± 0.09	19.95 ± 0.15	...	...	...	7.78 ± 0.09
(10199) Chariklo	3 Feb 2008	07:41	...	...	...	17.11 ± 0.06	16.61 ± 0.05	16.38 ± 0.06	...
	4 Feb 2008	07:41	18.79 ± 0.02	18.34 ± 0.02	17.88 ± 0.03	...	...	...	7.07 ± 0.04
(20000) Varuna	4 Dec 2007	06:09	20.49 ± 0.03	19.88 ± 0.03	...	...	...	...	4.04 ± 0.04
	4 Dec 2007	06:12	20.46 ± 0.04	19.88 ± 0.03	...	...	...	...	4.01 ± 0.05
(42301) 2001 UR_{163}	5 Dec 2007	00:52	21.82 ± 0.06	20.98 ± 0.07	...	...	...	...	4.72 ± 0.06
	5 Dec 2007	00:55	21.81 ± 0.05	20.98 ± 0.07	...	...	...	...	4.71 ± 0.06
(42355) Typhon	12 Apr 2008	00:59	20.50 ± 0.08	20.00 ± 0.08	19.70 ± 0.08	...	...	...	7.77 ± 0.11
(44594) 1999 OX_3	21 Sep 2008	04:07	21.26 ± 0.05	20.54 ± 0.06	19.96 ± 0.07	...	...	...	7.57 ± 0.06
	22 Sep 2008	04:49	...	...	...	19.08 ± 0.12	18.75 ± 0.08	18.69 ± 0.08	...
(52872) Okyrhoe	3 Feb 2008	06:41	...	...	...	16.84 ± 0.06	16.39 ± 0.07	16.28 ± 0.05	...
	4 Feb 2008	06:18	18.63 ± 0.02	18.14 ± 0.02	17.64 ± 0.02	...	...	...	10.97 ± 0.04
(55576) Amycus	12 Apr 2008	03:33	20.42 ± 0.08	19.78 ± 0.08	19.20 ± 0.15	...	...	...	8.27 ± 0.08
(55637) 2002 UX_{25}	6 Dec 2007	01:19	...	...	...	18.55 ± 0.03	18.25 ± 0.04	18.21 ± 0.06	...
(55638) 2002 VE_{95}	5 Dec 2007	03:35	20.31 ± 0.03	19.59 ± 0.04	...	...	...	...	5.80 ± 0.03
	5 Dec 2007	03:38	20.31 ± 0.03	19.59 ± 0.04	...	...	...	...	5.80 ± 0.03
	6 Dec 2007	02:09	...	...	...	18.11 ± 0.04	17.78 ± 0.04	17.74 ± 0.04	...
	22 Nov 2008	05:36	20.28 ± 0.06	19.53 ± 0.08	18.77 ± 0.09	...	...	...	5.76 ± 0.06
	23 Nov 2008	05:57	...	...	...	18.04 ± 0.07	17.68 ± 0.07	17.63 ± 0.09	...
(73480) 2002 PN_{34}	10 Nov 2007	00:36	20.68 ± 0.03	20.25 ± 0.05	...	19.00 ± 0.05	18.49 ± 0.06	18.29 ± 0.05	8.42 ± 0.10
(90377) Sedna	21 Sep 2008	06:33	21.34 ± 0.04	20.57 ± 0.05	19.93 ± 0.05	...	...	...	1.84 ± 0.04
	22 Sep 2008	06:57	...	...	...	19.20 ± 0.04	18.78 ± 0.06	...	...
(90482) Orcus	3 Feb 2008	04:46	...	...	...	17.91 ± 0.05	17.72 ± 0.07	17.89 ± 0.05	...
	4 Feb 2008	05:04	19.12 ± 0.02	18.73 ± 0.02	18.37 ± 0.02	...	...	...	2.30 ± 0.03
(120061) 2003 CO_1	4 Feb 2008	08:17	19.93 ± 0.02	19.45 ± 0.03	19.01 ± 0.03	...	...	...	8.95 ± 0.05
	12 Apr 2008	04:40	19.63 ± 0.08	19.20 ± 0.09	18.82 ± 0.15	...	...	...	9.16 ± 0.08
(120132) 2003 FY_{128}	12 Apr 2008	02:22	20.93 ± 0.09	20.34 ± 0.09	19.86 ± 0.15	...	...	...	5.09 ± 0.09
*(120178) 2003 OP_{32}	21 Sep 2008	02:10	20.25 ± 0.03	19.86 ± 0.05	19.50 ± 0.05	...	...	...	4.02 ± 0.04
(120348) 2004 TY_{364}	22 Nov 2008	04:32	20.64 ± 0.03	20.04 ± 0.04	19.52 ± 0.04	...	...	...	4.58 ± 0.04
	23 Nov 2008	03:22	...	...	...	18.87 ± 0.03	18.42 ± 0.05	18.39 ± 0.08	...
(136199) Eris	7 Dec 2007	00:20	...	...	...	17.90 ± 0.06	17.85 ± 0.05	18.15 ± 0.06	...
*(144897) 2004 UX_{10}	4 Dec 2007	00:53	20.61 ± 0.04	20.04 ± 0.04	...	...	...	...	4.62 ± 0.05
	4 Dec 2007	00:56	20.63 ± 0.04	20.05 ± 0.04	...	...	...	...	4.64 ± 0.05
	5 Dec 2007	02:24	20.63 ± 0.03	20.06 ± 0.04	...	...	...	...	4.62 ± 0.04
	6 Dec 2007	00:39	...	...	...	18.97 ± 0.06	18.55 ± 0.08	18.55 ± 0.09	...
	23 Nov 2008	02:26	...	...	...	19.02 ± 0.03	18.60 ± 0.04	18.64 ± 0.06	...
(145451) 2005 RM_{43}	4 Dec 2007	03:22	20.04 ± 0.04	19.66 ± 0.03	...	...	...	...	4.53 ± 0.05
	4 Dec 2007	03:25	20.07 ± 0.04	19.66 ± 0.03	...	...	...	...	4.56 ± 0.05
	7 Dec 2007	03:14	...	...	...	18.95 ± 0.04	18.76 ± 0.05	18.71 ± 0.06	...
(145453) 2005 RR_{43}	4 Dec 2007	02:26	20.05 ± 0.03	19.66 ± 0.04	...	...	...	...	4.16 ± 0.03
	4 Dec 2007	02:29	20.08 ± 0.03	19.66 ± 0.04	...	...	...	...	4.19 ± 0.03
	7 Dec 2007	02:24	...	...	...	19.28 ± 0.04	19.47 ± 0.07	19.67 ± 0.15	...
*(174567) 2003 MW_{12}	12 Apr 2008	07:07	20.57 ± 0.08	19.99 ± 0.08	19.57 ± 0.15	...	...	...	3.66 ± 0.08
(208996) 2003 AZ_{84}	22 Nov 2008	06:07	20.46 ± 0.03	20.08 ± 0.04	19.71 ± 0.03	...	...	...	3.77 ± 0.04
	23 Nov 2008	07:10	...	...	...	19.26 ± 0.04	18.92 ± 0.07	...	...
*2002 KY_{14}	21 Sep 2008	00:56	19.93 ± 0.02	19.23 ± 0.03	18.58 ± 0.04	...	...	...	10.37 ± 0.04
	22 Sep 2008	02:27	...	...	...	17.85 ± 0.06	17.56 ± 0.07	17.54 ± 0.08	...
2003 UZ_{117}	22 Nov 2008	03:21	21.13 ± 0.03	20.77 ± 0.04	20.43 ± 0.04	...	...	...	5.18 ± 0.03
	23 Nov 2008	05:08	...	...	...	20.41 ± 0.09	20.63 ± 0.17	...	...
*2003 UZ_{413}	4 Dec 2007	04:28	20.70 ± 0.04	20.22 ± 0.04	...	...	...	...	4.41 ± 0.05
	4 Dec 2007	04:31	20.67 ± 0.04	20.22 ± 0.04	...	...	...	...	4.38 ± 0.05
	21 Sep 2008	05:31	20.71 ± 0.04	20.25 ± 0.05	19.88 ± 0.06	...	...	...	4.36 ± 0.05
	22 Nov 2008	03:33	20.63 ± 0.03	20.22 ± 0.04	19.82 ± 0.04	...	...	...	4.36 ± 0.03
	23 Nov 2008	04:03	...	...	...	19.29 ± 0.05	18.92 ± 0.09	18.77 ± 0.09	...
*2007 UK_{126}	21 Sep 2008	08:05	20.41 ± 0.03	19.79 ± 0.04	19.32 ± 0.04	...	...	...	3.69 ± 0.04
	22 Sep 2008	07:43	...	...	...	18.88 ± 0.07	18.52 ± 0.08	...	...
*2007 UM_{126}	21 Sep 2008	04:26	20.88 ± 0.03	20.44 ± 0.03	20.00 ± 0.03	...	...	...	10.43 ± 0.03
	22 Sep 2008	05:57	...	...	...	...	18.84 ± 0.13	18.50 ± 0.08	...
*2007 VH_{305}	22 Nov 2008	02:14	21.44 ± 0.04	20.96 ± 0.04	20.48 ± 0.05	...	...	...	11.82 ± 0.06
	23 Nov 2008	00:38	...	...	...	19.70 ± 0.10	19.06 ± 0.12	19.43 ± 0.15	...
*2008 FC_{76}	20 Sep 2008	23:55	20.38 ± 0.03	19.67 ± 0.05	19.04 ± 0.06	...	...	...	9.46 ± 0.05
	21 Sep 2008	23:53	...	...	...	18.40 ± 0.08	18.00 ± 0.08	17.88 ± 0.09	...
*2008 SJ_{236}	22 Nov 2008	00:24	20.75 ± 0.03	20.13 ± 0.03	19.63 ± 0.04	...	...	...	12.47 ± 0.06
	23 Nov 2008	01:28	...	...	...	19.01 ± 0.07	18.60 ± 0.11	18.83 ± 0.12	...

* Objects that had their colors reported for the first time ever.

Each object has been classified whenever its colors were within 3σ of the class' average values. Obviously, a higher number of available colors implies a better reliability of the class determination. In cases where more than one class is within 3σ, a multiple designation was assigned to the object, with taxonomic classes ordered by ascending deviation of its colors from the class' averages. The obtained taxonomic designations are reported in Table 4.7, along with the dynamical classification of the objects (according to Gladman et al. 2008). Thirty-eight objects have been classified: nine of them turned out to belong to the BB class, seven were BR, ten were RR. The remaining twelve targets got a multiple designation.

Three objects, 2007 UK_{126}, (26375) 1999 DE_9, and (145452) 2005 RN_{43}, did not fall within any class of the existing taxonomy. Indeed, according to their visible colors an IR, RR classification could be derived, while their infrared colors match those of a BB, BR object. This fact, as well as the presence of several multiple classifications, could support the idea that further groups could be found as the number of analysed objects increases, leading to a refinement of the current taxonomy.

Below, objects that showed a peculiar behavior are discussed in further detail.

(10199) Chariklo: Using five color indices, this Centaur has been classified as a BR object, as Fulchignoni et al. (2008) did on the basis of the mean colors published in literature. The results in Perna et al. (2010a), obtained in February 2008 (and already published in Guilbert et al. 2009), agree with these average measurements except for the $V - K$ color which is about 0.2 magnitudes redder in the 2008 dataset. Interestingly, Chariklo was already observed in the framework of the ESO-LP programme in March 2007 (DeMeo et al. 2009b, who assigned to Chariklo a BR, BB classification), but no match is found with these previous results (compare values in Tables 4.5 and 4.6). Since the acquisition and the reduction of the data were carried out in the same way in both observing runs, this is a probable indication of heterogeneity on the surface of this Centaur, as already proposed in previous works (see Guilbert et al. 2009, and references therein).

(90377) Sedna: The photometric colors and taxonomic classification (RR) derived for Sedna are in agreement with those published by Barucci et al. (2005b), except for the $V - J$ color which is approximately 0.2 magnitudes bluer in the ESO-LP dataset. Since images in different filters have not been acquired simultaneously, the observation of different rotational phases of the object could affect color determinations. Nevertheless the light curve

Table 4.7 – Taxonomic classification of Centaurs and TNOs obtained within the ESO Large Programme.

Object	Dyn. Class	Taxonomy			N
		Fulchignoni et al. (2008)	DeMeo et al. (2009b)	Perna et al. (2010a)	
(5145) Pholus	Centaur	RR	...	RR	2
(10199) Chariklo	Centaur	BR	BR,BB	BR	5
(42355) Typhon	Scattered	BR	BR	BR,BB	5[a]
(44594) 1999 OX_3	Scattered	RR	...	RR	5
(52872) Okyrhoe	Jupiter-coupled	BR	...	BR,IR	5
(55576) Amycus	Centaur	RR	...	RR,IR	2
(55637) 2002 UX_{25}	Classical	IR	RR,IR	RR	5[b]
(55638) 2002 VE_{95}	Resonant (3:2)	RR	...	RR	5
(73480) 2002 PN_{34}	Scattered	...	...	BR,BB	4
(90377) Sedna	Detached	RR	...	RR	4
(90482) Orcus	Resonant (3:2)	BB	...	BB	5
(120061) 2003 CO_1	Centaur	...	...	BR	2
(120132) 2003 FY_{128}	Detached	...	BR	BR	5[a]
(120178) 2003 OP_{32}	Classical	...	...	BB,BR	2
(120348) 2004 TY_{364}	Classical	...	...	IR,RR,BR	5
(136199) Eris	Detached	BB	BB	BB	5[b]
(144897) 2004 UX_{10}	Classical	...	...	BR	4
(145451) 2005 RM_{43}	Detached	...	BB	BB	4
(145453) 2005 RR_{43}	Classical	...	BB	BB	4
(174567) 2003 MW_{12}	Classical	...	...	IR,BR,RR	2
(208996) 2003 AZ_{84}	Resonant (3:2)	BB	BB	BB	4
2002 KY_{14}	Centaur	...	...	RR	5
2003 UZ_{117}	Classical	...	...	BB	4
2003 UZ_{413}	Resonant (3:2)	...	...	BB	5
2007 UM_{126}	Centaur	...	...	BR,BB	4
2007 VH_{305}	Centaur	...	...	BR	5
2008 FC_{76}	Centaur	...	...	RR	5
2008 SJ_{236}	Centaur	...	...	RR	5
(28978) Ixion	Resonant (3:2)	IR	BB		4
(32532) Thereus	Centaur	BR	BB		5
(47171) 1999 TC_{36}	Resonant (3:2)	RR	RR		4
(47932) 2000 GN_{171}	Resonant (3:2)	IR	BR,IR		5
(50000) Quaoar	Classical	...	RR		4
(54598) Bienor	Centaur	BR	BR		4
(55565) 2002 AW_{197}	Classical	IR	IR,RR		5
(60558) Echeclus	Jupiter-coupled	BR	BR,BB		4
(90568) 2004 GV_9	Classical	...	BR		4
2003 QW_{90}	Classical	...	IR,RR,BR		2

NOTE: In the statistical analysis of taxa, for the first 28 bodies the classification from Perna et al. (2010a) is taken into account. Last 10 objects come from DeMeo et al. (2009b). N is the number of colors used to classify each object, by Perna et al. (2010a) or DeMeo et al. (2009b).
[a] Using near-infrared data from DeMeo et al. (2009b).
[b] Using visible data from DeMeo et al. (2009b).

of Sedna has an amplitude of only 0.02 magnitudes (Gaudi et al. 2005), hence different observed silhouettes of the body cannot explain the found discrepancy, which could instead be attributed to surface heterogeneity.

(145451) 2005 RM_{43}: Both datasets obtained in the framework of the ESO-LP give a BB classification, even if both $V-J$ and $V-H$ colors are ~ 0.2 magnitudes redder in Perna et al. (2010a) than in DeMeo et al. (2009b), while the $V-K$ color is consistent. Observations with different filters have not been carried out simultaneously, but, as for Sedna, the amplitude of the light curve is smaller than the observed discrepancies ($\Delta m = 0.12 \pm 0.05$ magnitudes; Perna et al. 2009, see section 4.3), suggesting possible surface heterogeneity.

(145453) 2005 RR_{43}: Observed twice during the ESO-LP, Perna et al. (2010a) confirm that 2005 RR_{43} is a BB object, as classified by DeMeo et al. (2009b), but in the former work the $V-H$ color is 0.4 magnitudes bluer than published by the latter. Again, images with different filters have not been acquired at the same moment but the amplitude of the light curve is only $\Delta m = 0.12 \pm 0.03$ magnitudes (Perna et al. 2009, see section 4.3), so the observation of different compositions on the surface is a likely explanation for the reported discrepancy.

(26375) 1999 DE_9: Seven measurements combined in Fulchignoni et al. (2008) produced the previous classification (IR) of 1999 DE_9. Considering that light curve data do not indicate significant magnitude variations (Sheppard & Jewitt 2002), it appears that previous measurements were robust and stable. As said above, 1999 DE_9 did not fall within any taxon on the basis of the ESO-LP data (five color indices). While the obtained visible colors agree with published results, the $V-J$, $V-H$, $V-K$ colors are approximately 0.3 magnitudes bluer. The $J-H$ and $J-K$ colors, however, are in good agreement with previous works (Doressoundiram et al. 2007; Delsanti et al. 2006). Jewitt & Luu (2001) noted a spectral feature attributed to H_2O ice (abundance around 10%), which was also detected by Barkume et al. (2008). This feature was not seen by Doressoundiram et al. (2003), suggesting that there may be heterogeneity on the surface.

(29878) Ixion: Ixion had been classified by Fulchignoni et al. (2008) as an IR object, based on a set of six colors from Doressoundiram et al. (2007), while it is a BB-type according to the ESO-LP data (four colors). Obtained $V-J$ and $V-H$ colors were each almost 0.3 magnitudes lower than seen by Doressoundiram et al. (2007), which produced the significant classification change ($J-H$ color agrees with the above cited work, while the $J-K$ is slightly redder). This body does not have a significant light curve amplitude (Sheppard & Jewitt 2003; Ortiz et al. 2003), so the observed discrepancies may correspond to surface heterogeneity.

(32532) Thereus: The Centaur Thereus was previously classified as a BR object (Fulchignoni et al. 2008), while the ESO-LP data classify it as a BB-type. Though the obtained visible magnitudes agree with published results, the $V-J$, $V-H$, and $V-K$ colors are, respectively, more than 0.3, almost 0.4, and ~ 0.45 magnitudes bluer than the average values published by Fulchignoni et al. (2008). These differences are striking. Thereus has a double peaked light curve of amplitude 0.18 magnitudes. Moreover, the rotational period is of 8.34 hours (Farnham & Davies 2003), while ESO-LP visible and NIR measurements were taken only 11 minutes apart, so the difference cannot be attributed to observing different parts of the surface. Merlin et al. (2005) report significant spectral variation across the surface, which could rather account for the reported discrepancy.

(47932) 2000 GN_{171}: This object has been classified as a BR, IR, which is consistent with the previous result (IR) by Fulchignoni et al. (2008). Though a homogeneous surface composition has been suggested for 2000 GN_{171} (Merlin et al. 2005), the calculated absolute magnitude H_v ranges from 6.20 to 6.31 ± 0.04 depending on the night of observation, while Doressoundiram et al. (2007) reports $H_v = 6.71 \pm 0.05$ and McBride et al. (2003) found a similar value of 6.71 ± 0.04. Moreover, the $V-J$, $V-H$, and $V-K$ colors are, respectively, ~ 0.2, ~ 0.2, and ~ 0.3 magnitudes bluer than the averages computed by Fulchignoni et al. (2008). Nevertheless the observed discepancies are well within the amplitude of the light curve (~ 0.6 magnitudes, Sheppard & Jewitt 2002; Perna et al. 2009, see section 4.3).

(54598) Bienor: The calculated absolute magnitude H_v is 7.46 ± 0.03, while Doressoundiram et al. (2007) obtained $H_v = 8.04 \pm 0.02$. This large difference is still smaller than the light curve amplitude of 0.75 ± 0.09 magnitudes (while the period is 4.57 ± 0.02 hours, Ortiz et al. 2002). Visible and NIR observations were taken approximately 45 minutes apart, a time span during which the object rotated significantly, which could also account for the observed difference.

4.2.3 Statistical analysis

Before the ESO-LP, Fulchignoni et al. (2008) classified all of the 132 TNOs and Centaurs for which data from the literature were available (one more object, 1998 WU_{24}, was classified as BR; but it has an unusual orbit, it is not a Centaur, and therefore I do not consider it in the analysis). Of the 38 objects for which the taxonomy has been derived in the framework of the

ESO-LP, 19 of them have been classified for the first time (which constitutes about a 14% increase of the sample), while 4 targets were assigned different classes with respect to the results by Fulchignoni et al. (2008).

Considering the total sample of 151 objects, the average colors of each taxon were obtained. They are reported in Table 4.8 and represented in Fig. 4.8 as reflectance values normalized to the Sun and to the V colors. In the cases where multiple taxonomic classes were assigned to an object, only the first designation was taken into account. Then, the distribution of the four taxonomic groups with respect to the dynamical properties of the objects was analysed.

Table 4.8 – Average colors of the four TNO taxa.

Class	$B-V$	$V-R$	$V-I$	$V-J$	$V-H$	$V-K$
BB	0.68 ± 0.06	0.39 ± 0.05	0.75 ± 0.06	1.20 ± 0.25	1.28 ± 0.50	1.32 ± 0.60
BR	0.75 ± 0.06	0.49 ± 0.05	0.96 ± 0.08	1.68 ± 0.15	2.11 ± 0.14	2.26 ± 0.13
IR	0.92 ± 0.05	0.59 ± 0.04	1.15 ± 0.07	1.86 ± 0.06	2.20 ± 0.09	2.29 ± 0.10
RR	1.06 ± 0.10	0.69 ± 0.06	1.35 ± 0.10	2.22 ± 0.20	2.58 ± 0.25	2.59 ± 0.28

NOTE: All of the 151 Centaurs and TNOs that have been classified thus far are taken into account. In the cases where multiple taxonomic classes were assigned to an object, the first designation is considered.

First of all, the sampling of the taxa within each dynamical class (Fig. 4.9) was verified. The well-known color bimodality of Centaurs clearly emerges, since 13 out of 25 objects belong to the BR group, while 10 of them fall in the RR class. All of the four new IR-classified objects are classical TNOs, confirming the finding that IR objects seem to be concentrated in the resonant and classical dynamical classes, as stated by Fulchignoni et al. (2008). As reported by the same authors, RR objects dominate the classical TNOs. However, the classical TNOs in the objects constituting the ESO-LP sample do not conform to this behavior, as a quite equal division of the four taxa appears among them (check Table 4.7).

In Fig. 4.10 the distribution of taxonomical classes with respect to the semimajor axes a of the objects is presented. A 10 AU binning is adopted (nine objects are out of the scale). As already noted by Fulchignoni et al. (2008), the more distant TNOs belong to all the four taxa in a quite uniform way, while for $a \lesssim 30$ AU the BR and RR classes dominate the population.

Finally, Fig. 4.11 reports the distribution of the taxa with respect to the orbital inclination i. A 5° binning is adopted (two objects are out of the scale). Inclinations of RR-types are quite low, in agreement with the previously mentioned finding of a red dynamically "cold" population. On the

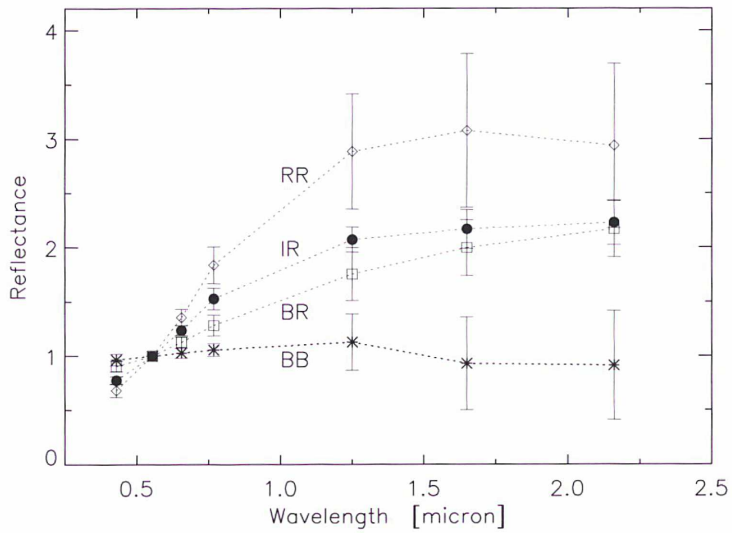

Figure 4.8 – Average reflectance values for each TNO taxon, normalized to the Sun and to the V colors. From Perna et al. (2010a).

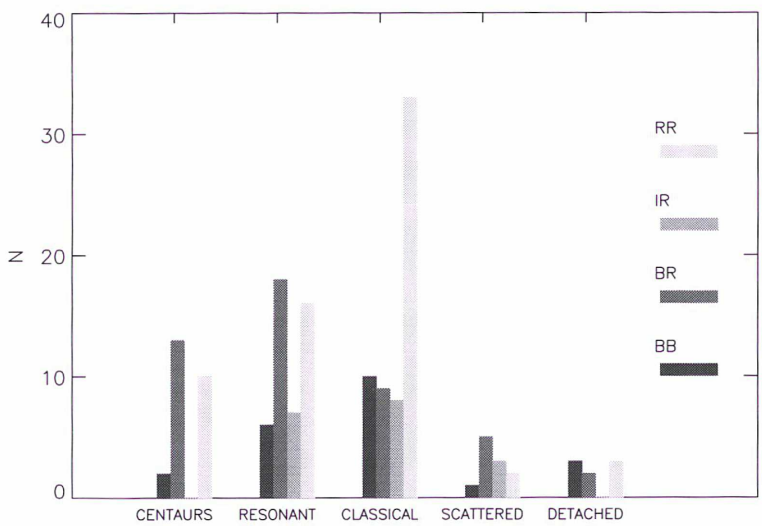

Figure 4.9 – Distribution of the TNO taxa within each dynamical class, as defined by Gladman et al. (2008). From Perna et al. (2010a).

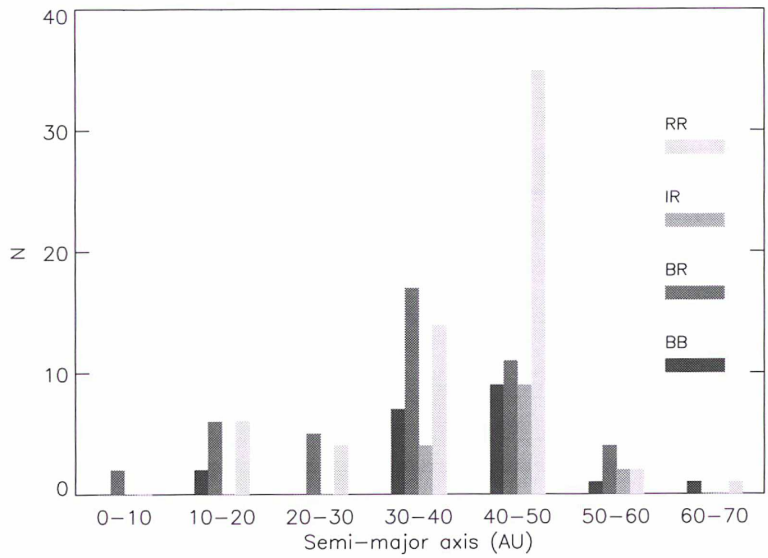

Figure 4.10 – Distribution of the TNO taxa with respect to the semimajor axis of the objects. A 10 AU binning is adopted. From Perna et al. (2010a).

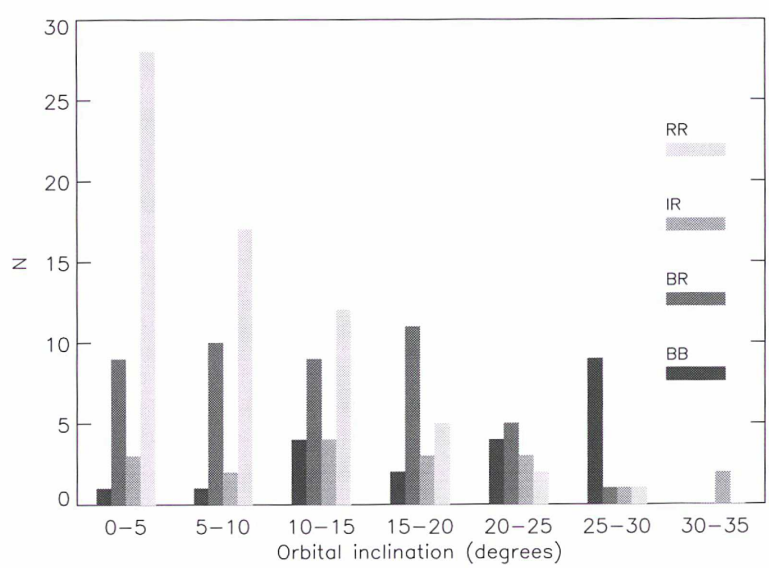

Figure 4.11 – Distribution of the TNO taxa with respect to the orbital inclination of the objects. A 5° binning is adopted. From Perna et al. (2010a).

contrary, BB-types seem to be concentrated at high inclinations, confirming the suggested association of these objects with the "hot" population.

As suggested by Fulchignoni et al. (2008), it is possible to interpret the different TNO taxa both in terms of evolution of the population and/or in terms of original differences in the composition of the objects.

In the former case, the "trend" connecting the BB taxon to the RR taxon would indicate the time during which an object has been exposed to different alteration processes (induced by collisions and/or space weathering), and each taxon represents a different stage in the evolution of the population.

In terms of original compositional differences, the dichotomy between the "hot" BB-types and the "cold" RR-types would be real. In this case, BR and IR objects would represent the space weathered evolution of BB and RR objects, respectively. As explained in section 1.2.2.2, the energetic particle bombardment of "dirty" icy surfaces induces the formation of dark, spectrally red hydrocarbons, which could be considered to be responsible for the BB $\rightarrow$ BR transition. Conversely, the induced loss of carbonaceous volatiles would result in objects being less red than they were previously, hence in the RR $\rightarrow$ IR transition.

4.3 Light curves and densities

The most useful tool for investigating the rotational properties of TNOs and for computing the axis ratios of the osculating ellipsoids approximating their shapes is the analysis of photometric light curves, which also allows us to retrieve useful information on the internal structure of each observed body (see section 1.4.3).

4.3.1 Observations and data reduction

To increase the still rather limited sample of TNOs with known rotational properties (few tens of objects, for a review see Sheppard et al. 2008), in the framework of the ESO-LP two observing runs (3 nights each) have been carried out in April 2007 and December 2007 at the ESO-NTT (La Silla, Chile).

The observations have been performed using the EMMI (ESO Multi-Mode Instrument) instrument in RILD ("red") mode. The R filter (centered on 641.0 nm) was used, adjusting the exposure time according to the object magnitude and sky conditions.

In April 2007 data have been obtained on 2 Centaurs, (12929) 1999 TZ_1 and (95626) 2002 GZ_{32}, and 5 Trans-Neptunian Objects: (42355) Typhon, (47932) 2000 GN_{171}, (65489) Ceto, (90568) 2004 GV_9, and (120132) 2003 FY_{128}. Five additional TNOs have been studied during the second run: (144897) 2004 UX_{10}, (145451) 2005 RM_{43}, (145453) 2005 RR_{43}, 2003 UZ_{117}, and 2003 UZ_{413}.

Table 4.9 reports the dynamical classification (according to Gladman et al. 2008) and the absolute magnitude H (reported by the Minor Planet Center) of each observed target.

Table 4.9 – TNOs and Centaurs whose light curves have been obtained in the framework of the ESO-LP.

Object	Dyn. class.	H
(12929) 1999 TZ_1	Trojan/Centaur	9.3
(42355) Typhon	Scattered TNO	7.2
(47932) 2000 GN_{171}	Resonant TNO	6.0
(65489) Ceto	Scattered TNO	6.3
(90568) 2004 GV_9	Classical TNO	4.0
(95626) 2002 GZ_{32}	Centaur	6.8
(120132) 2003 FY_{128}	Detached TNO	5.0
(144897) 2004 UX_{10}	Classical TNO	4.7
(145451) 2005 RM_{43}	Detached TNO	4.4
(145453) 2005 RR_{43}	Classical TNO	4.0
2003 UZ_{117}	Classical TNO	5.3
2003 UZ_{413}	Resonant TNO	4.3

The images were reduced using standard procedures (see section 2.1.1), but because of the non-photometric sky conditions, an absolute calibration of the magnitudes, by means of observing standard stars, was impossible. Therefore, differential photometry with bright (to minimize random errors) field stars was performed, typically using three of them within each image.

By visual inspection and radial profile analysis of the images, a search for possible signatures of a faint coma around the observed TNOs have been performed, but none were found.

The obtained (light-time corrected) single-night light curves are presented in Figs. 4.12 and 4.13.

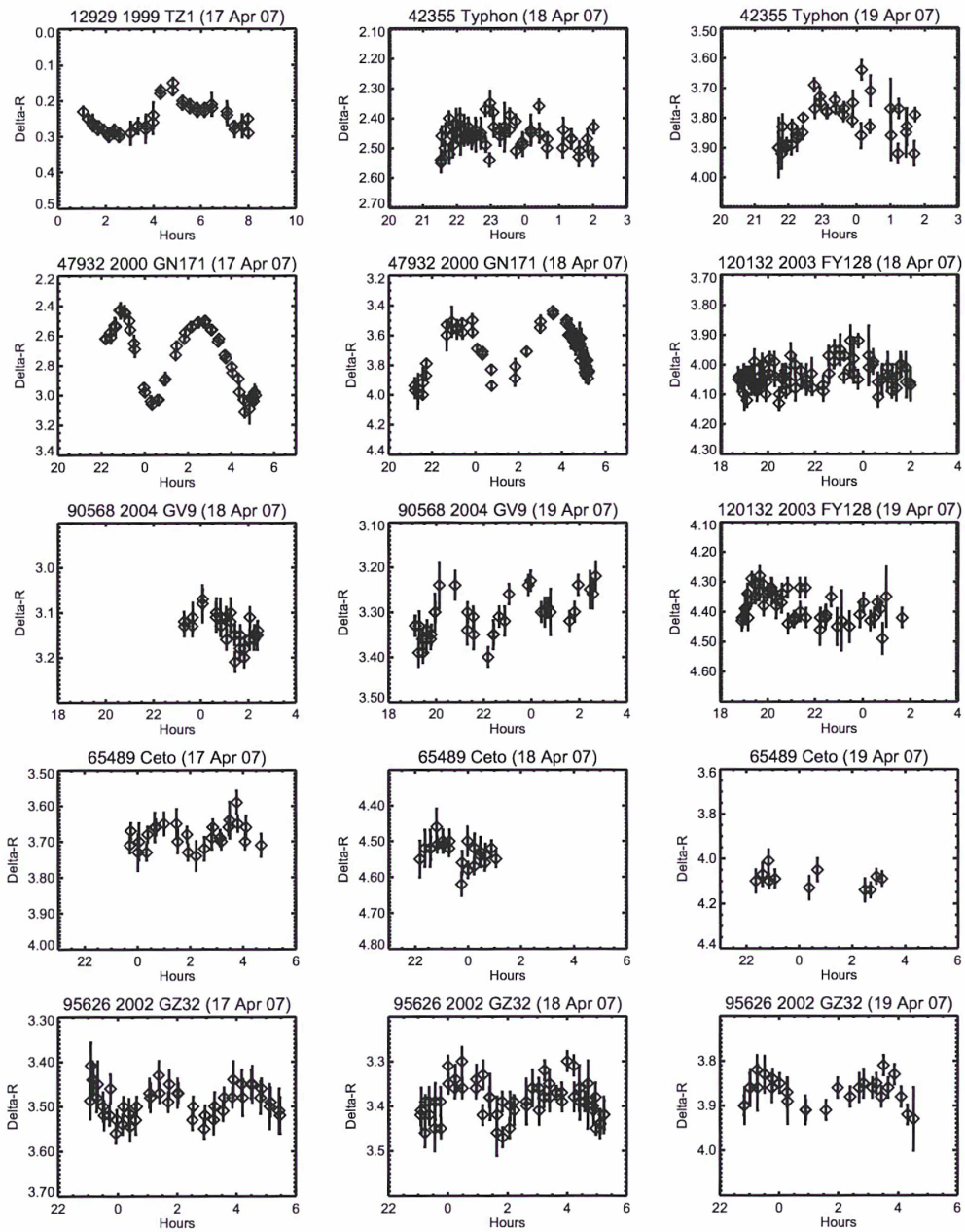

Figure 4.12 – Single-night light curves of the objects observed in April 2007. The name of the target and the night of observation (with respect to 0 UT) are reported above each plot. From Dotto et al. (2008).

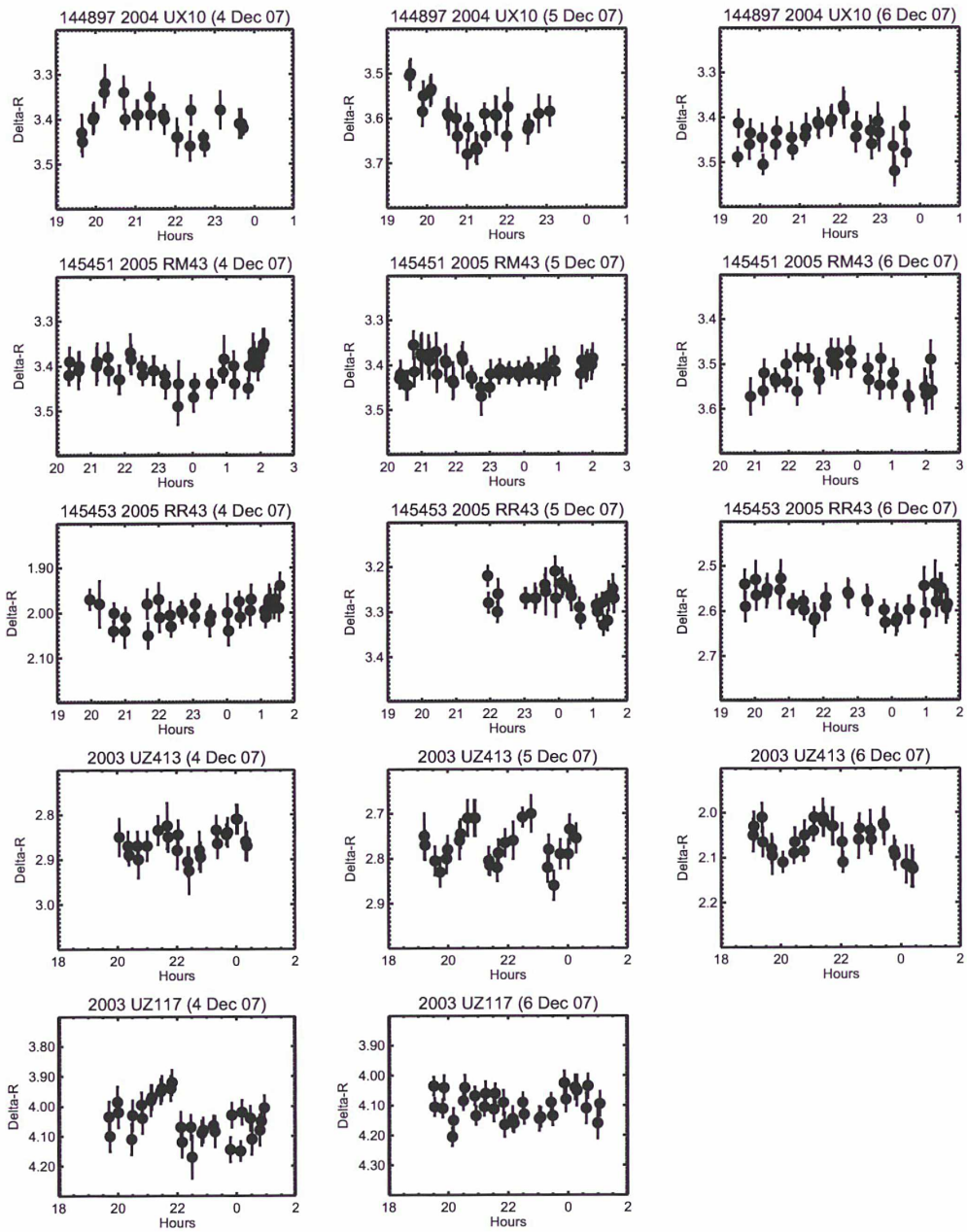

Figure 4.13 – Single-night light curves of the objects observed in December 2007. The name of the target and the night of observation (with respect to 0 UT) are reported above each plot. From Perna et al. (2009).

4.3.2 Results

A Fourier analysis of the light curves was performed following the method developed by Harris et al. (1989a) and described in section 1.2.1. For 9 out of the 12 observed TNOs, the synodic rotational period has been obtained, while the quality of the data points was not good enough to find an unambiguous solution for Typhon, 2003 FY_{128}, and 2003 UZ_{117}. The composite light curves are shown in Figs. 4.14-4.22.

A lower limit for the axis ratio a/b has been obtained from Eq. 1.10, while density estimations were derived as described in section 1.4.3.

The outcome of the above-quoted analysis on the observed objects is presented below.

(12929) 1999 TZ_1: at the time of the observations it was classified as a Centaur, however recent dynamical integrations seem to suggest that it is a Jupiter Trojan (Moullet et al. 2008). It has been observed during one night for more than 7 hours. The light curve amplitude is at least of 0.15 ± 0.02 mag, hence the axis ratio a/b is at least 1.15 ± 0.02. The data seem to suggest a single peaked periodicity of about 5 hours, in good agreement with the double peaked rotational period of 10.4 hours suggested by Moullet et al. (2008, see Fig. 4.14). From Eq. 1.11, the resulting lower limit to the density is 0.11 g cm^{-3}, while the Chandrasekhar (1987) table for rotationally stable Jacobi ellipsoids forecasts a density range of 0.36-0.47 g cm^{-3}.

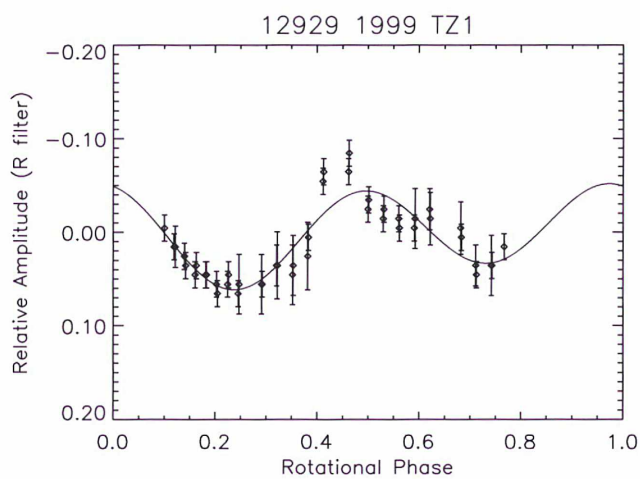

Figure 4.14 – Composite light curve of (12929) 1999 TZ_1, obtained with a synodic period of $P = 10.4$ hours. The zeropoint is at 0 UT on 17 April 2007. From Dotto et al. (2008).

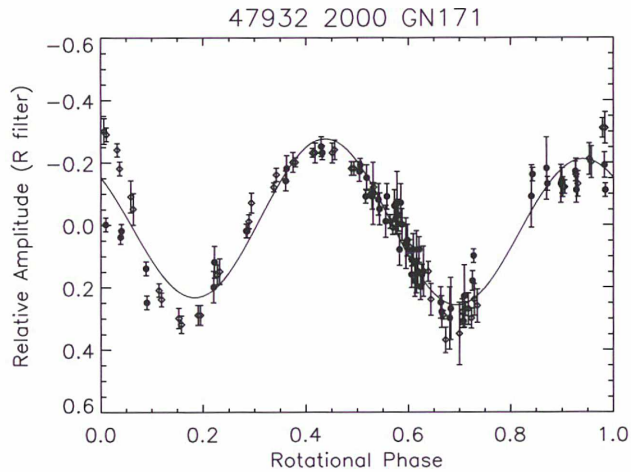

Figure 4.15 – Composite light curve of (47932) 2000 GN_{171}, obtained with a synodic period of $P = 8.329$ hours. The zeropoint is at 0 UT on 18 April 2007. From Dotto et al. (2008).

(42355) Typhon: it is a scattered object, whose binary nature has been recently shown by Noll et al. (2006). It has been observed during 2 nights for more than 8 hours. The data reported in Fig. 4.12 did not show any peculiar periodicity and were not enough to determine the rotational period, which must be longer than the 5 hours of continuous observation performed during each observing night.

(47932) 2000 GN_{171}: it is a resonant (3:2) TNO already observed by Sheppard & Jewitt (2002), who obtained a double peaked composite light curve with a rotational period of $P = 8.329 \pm 0.005$ hours. The ESO-LP observations, carried out during two different observing nights, confirm this period. The composite light curve (Fig. 4.15) presents a large amplitude of $\Delta m = 0.60 \pm 0.03$, which gives an axis ratio $a/b \geq 1.74 \pm 0.04$. 2000 GN_{171} is therefore one of the most elongated TNOs. Due to its large light curve amplitude, instead of Eq. 1.11, it has been adopted the contact spheres' model proposed by Jewitt & Sheppard (2002) for (20000) Varuna, which estimates the lower limit to the density as:

$$\rho = \frac{3\pi}{GP^2} \frac{[1 + (10^{0.4\Delta m} - 1)^{1/2}]^3}{1 + (10^{0.4\Delta m} - 1)^{3/2}} \tag{4.4}$$

where G is the gravitational constant. The obtained value is 0.62 g cm^{-3}, while, assuming the object to be a rotationally stable Jacobi ellipsoid, the density should be in the interval 0.56-0.74 g cm^{-3}.

(65489) Ceto: this scattered object has been observed during three different nights for a total of about 14 hours. The results, shown in Fig. 4.16, suggest a double peaked rotational period of 4.43 ± 0.03 hours. The lightcurve amplitude is of about 0.13 ± 0.02, hence the lower limit of the axis ratio a/b is 1.13 ± 0.02. On the basis of this result (65489) Ceto is a very fast rotator among TNOs, which is unexpected because Grundy et al. (2007), through Hubble Space Telescope observations, have revealed that this object is a close binary system, composed of two components of about 87 and 66 km, with a bulk density of $1.37^{+0.66}_{-0.32}$ g cm^{-3}. In particular, the derived rotation period implies that the system is clearly not completely spin locked (as for example the Pluto-Charon system), the rotation rate of the primary being much faster than the orbital period of the binary system, estimated at about 9.55 days by Grundy et al. (2007). The total angular momentum (orbital plus rotational) of the binary system is slightly in excess of the critical one for rotational fission (e.g., Descamps & Marchis 2008). These facts might suggest a recent tidal breakup origin for the Ceto/Phorcys system. The density lower limit from Eq. 1.11 and the density range from the Chandrasekhar (1987) table are 0.63 g cm^{-3} and 1.99-2.61 g cm^{-3}, respectively.

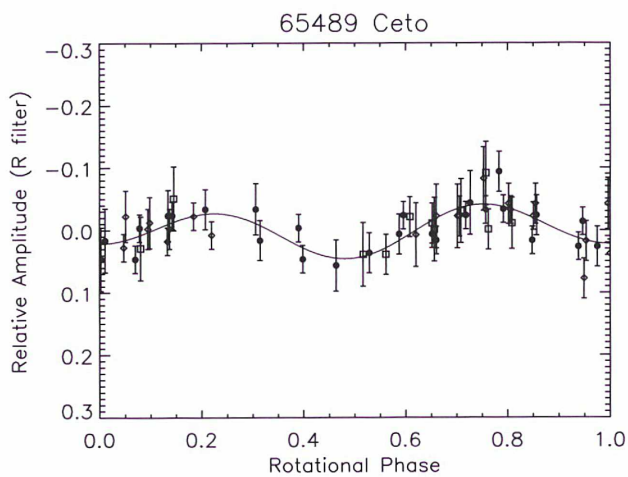

Figure 4.16 – Composite light curve of (65489) Ceto, obtained with a synodic period of $P = 4.43$ hours. The zeropoint is at 0 UT on 18 April 2007. From Dotto et al. (2008).

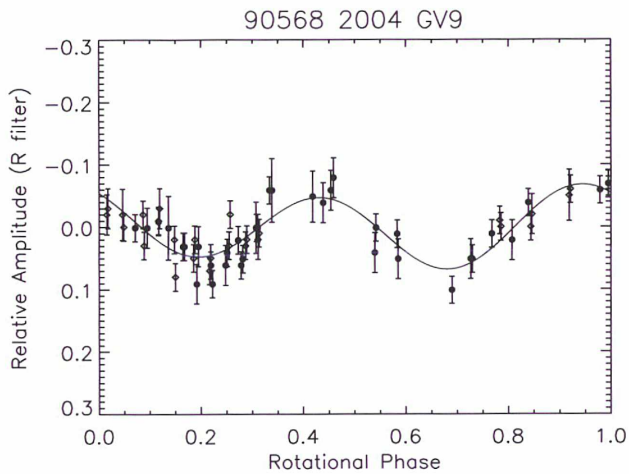

Figure 4.17 – Composite light curve of (90568) 2004 GV_9, obtained with a synodic period of $P = 5.86$ h. The zeropoint is at 0 UT on 19 April 2007. From Dotto et al. (2008).

(90568) 2004 GV_9: it is a classical TNO, observed during 2 nights for more than 11 hours. The composite light curve shown in Fig. 4.17 has been obtained with a rotational period of 5.86±0.03 hours. The light curve amplitude of 0.16 ± 0.03 gives $a/b \geq 1.16 \pm 0.03$. Making use of Eq. 1.11 a lower limit to the density of 0.37 g cm^{-3} is derived, while from the Chandrasekhar (1987) table for rotationally stable Jacobi ellipsoids forecasts a density in the range 1.14-1.49 g cm^{-3}.

(95626) 2002 GZ_{32}: this Centaur has been observed during three different nights for more than 18 hours. The double peaked composite light curve shown in Fig. 4.18 has been obtained with a synodic period of 5.80 ± 0.03 hours. The light curve amplitude of 0.15 ± 0.03 suggests an axis ratio a/b more than 1.15 ± 0.03. From Eq. 1.11 the lower limit to the density is 0.37 g cm^{-3}, while with the Chandrasekhar (1987) model a density range of 1.16-1.52 g cm^{-3} is obtained.

(120132) 2003 FY_{128}: is a detached TNO observed during 2 different nights for more than 13 hours. The single night light curves shown in Fig. 4.12 did not allow determination of the rotational period of this object, which is likely longer than the 7 hours of continuous observation performed during the first night.

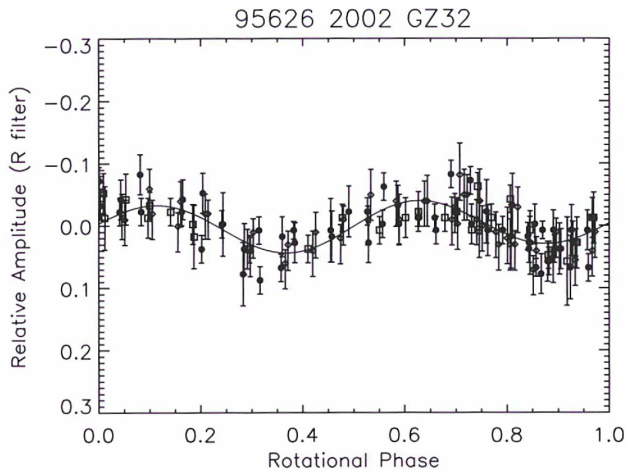

Figure 4.18 – Composite light curve of (95626) 2002 GZ_{32}, obtained with a synodic period of$P = 5.80$ h. The zeropoint is at 0 UT on 18 April 2007. From Dotto et al. (2008).

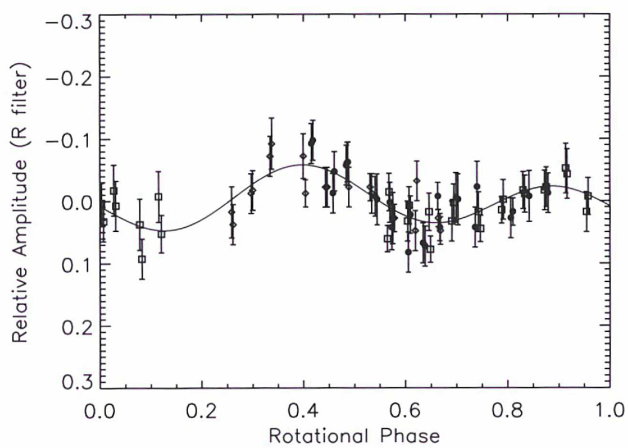

Figure 4.19 – Composite light curve of (144897) 2004 UX_{10}, obtained with a synodic period of $P = 7.58$ h. The zeropoint is at 0 UT on 5 December 2007. From Perna et al. (2009).

(144897) 2004 UX_{10}: this object has been observed during three nights for about 12 h. The composite light curve (Fig. 4.19) exhibits a double peaked periodicity of 7.58±0.05 h and an amplitude of 0.14±0.04 mag, which implies

an axis ratio $a/b \geq 1.14 \pm 0.04$. From Eq. 1.11, the resulting lower limit to the density is 0.22 g cm^{-3}, while the Chandrasekhar (1987) table forecasts a density range of 0.68-0.89 g cm^{-3}.

(145451) 2005 RM$_{43}$: its double peaked composite light curve (Fig. 4.20), of amplitude $\Delta m = 0.12 \pm 0.05$ mag, was obtained on the basis of data collected during three different nights for a total observing time of about 17 h. A synodic rotational period of $P = 9.00 \pm 0.06$ h and a lower limit to the axis ratio of $a/b = 1.12 \pm 0.05$ were found. From Eq. 1.11 the lower limit to the density is 0.15 g cm^{-3}, while, assuming the object to be a rotationally stable Jacobi ellipsoid, the density should be in the interval 0.48-0.63 g cm^{-3}.

(145453) 2005 RR$_{43}$: from the analysis of the light curve (15 h of observations during three nights) a double peaked periodicity of 5.08 ± 0.04 h emerged (Fig. 4.21). The amplitude is 0.12 ± 0.03 mag, which leads to an axis ratio $a/b \geq 1.12 \pm 0.03$. The density lower limit from Eq. 1.11 and the density range from the Chandrasekhar (1987) table are 0.47 g cm^{-3} and 1.51-1.98 g cm^{-3}, respectively.

2003 UZ$_{117}$: this object was observed for about 10.5 h during two nights. Although the light curve periodicity seems to be compatible with a rotational period of about 6 h, no clear solutions were found and different values are plausible.

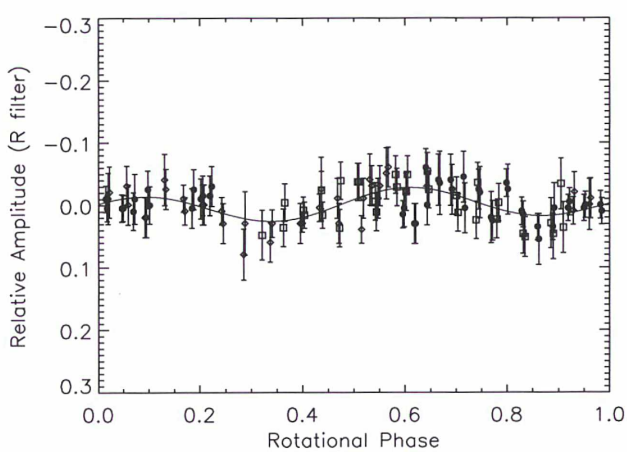

Figure 4.20 – Composite light curve of (145451) 2005 RM$_{43}$, obtained with a synodic period of $P = 9.00$ h. The zeropoint is at 0 UT on 5 December 2007. From Perna et al. (2009).

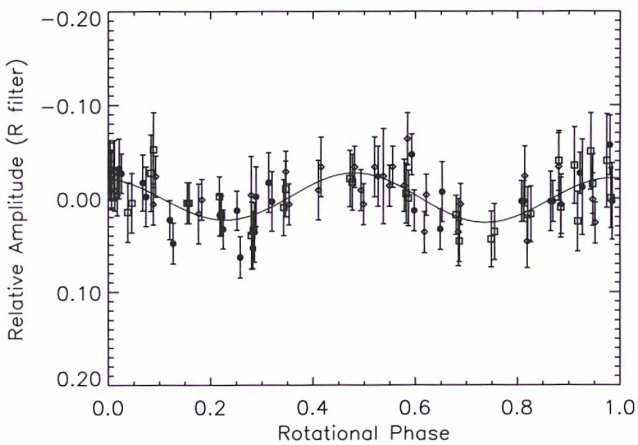

Figure 4.21 – Composite light curve of (145453) 2005 RR_{43}, obtained with a synodic period of $P = 5.08$ h. The zeropoint is at 0 UT on 5 December 2007. From Perna et al. (2009).

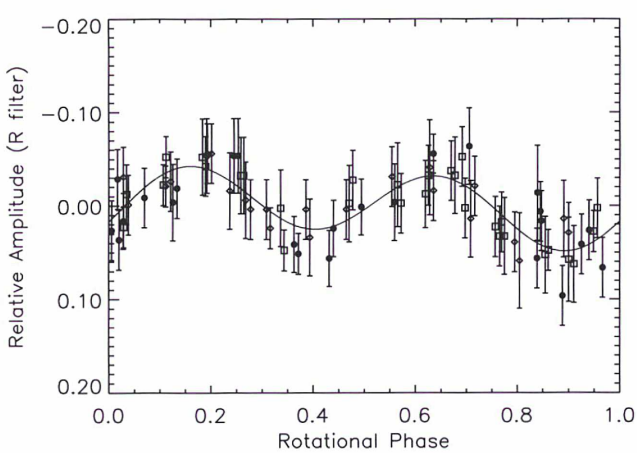

Figure 4.22 – Composite light curve of 2003 UZ_{413}, obtained with a synodic period of $P = 4.13$ h. The zeropoint is at 0 UT on 5 December 2007. From Perna et al. (2009).

2003 UZ_{413}: the data collected in about 14.5 h of observing time during three nights suggest, for this resonant (3:2) TNO, a double peaked periodicity of 4.13±0.05 h (Fig. 4.22). The light curve amplitude is $\Delta m = 0.13 \pm 0.03$ mag, which yields an axis ratio $a/b \geq 1.13 \pm 0.03$. Making use of Eq. 1.11 a lower limit to the density of 0.72 g cm^{-3} is derived, while from the Chandrasekhar (1987) table for rotationally stable Jacobi ellipsoids forecasts a density in the range 2.29-3.00 g cm^{-3}. These results indicate that 2003 UZ_{413} is a quite peculiar, very rapidly rotating TNO (the second fastest rotator after (136108) Haumea), and further studies of this body are required.

4.3.3 Discussion

For each object, Table 4.10 reports the computed rotational period, the light curve amplitude, the lower limit to the axis ratio a/b, the lower limit to the density (from Eq. 1.11, and Eq. 4.4 for 2000 GN_{171}), and the density range obtained from the Chandrasekhar (1987) table for rotationally stable Jacobi ellipsoids.

In Fig. 4.23, these latter density values are plotted versus H, together with literature data (Sheppard et al. 2008, and references therein). Only objects with absolute magnitude ≤ 7 (i.e., radius $\gtrsim 100$ km assuming moderate albedos) are taken into account.

Table 4.10 – Results from the analysis of the light curves of TNOs and Centaurs.

Object	Rot. Period (h)	Δm (mag)	a/b (lower limit)	ρ_{min} (g cm^{-3})	ρ_{Jacobi} (g cm^{-3})
(12929) 1999 TZ_1	10.4[a]	0.15±0.02	1.15±0.02	0.11	0.36-0.47
(42355) Typhon	>5				
(47932) 2000 GN_{171}	8.329±0.005[b]	0.60±0.03	1.74±0.04	0.62	0.56-0.74
(65489) Ceto	4.43±0.03	0.13±0.02	1.13±0.02	0.63	1.99-2.61
(90568) 2004 GV_9	5.86±0.03	0.16±0.03	1.16±0.03	0.37	1.14-1.49
(95626) 2002 GZ_{32}	5.80±0.03	0.15±0.03	1.15±0.03	0.37	1.16-1.52
(120132) 2003 FY_{128}	>7				
(144897) 2004 UX_{10}	7.58 ± 0.05	0.14 ± 0.04	1.14 ± 0.04	0.22	0.68–0.89
(145451) 2005 RM_{43}	9.00 ± 0.06	0.12 ± 0.05	1.12 ± 0.05	0.15	0.48–0.63
(145453) 2005 RR_{43}	5.08 ± 0.04	0.12 ± 0.03	1.12 ± 0.03	0.47	1.51–1.98
2003 UZ_{117}	∼ 6 ?				
2003 UZ_{413}	4.13 ± 0.05	0.13 ± 0.03	1.13 ± 0.03	0.72	2.29–3.00

[a] by Moullet et al. (2008)
[b] by Sheppard & Jewitt (2002)

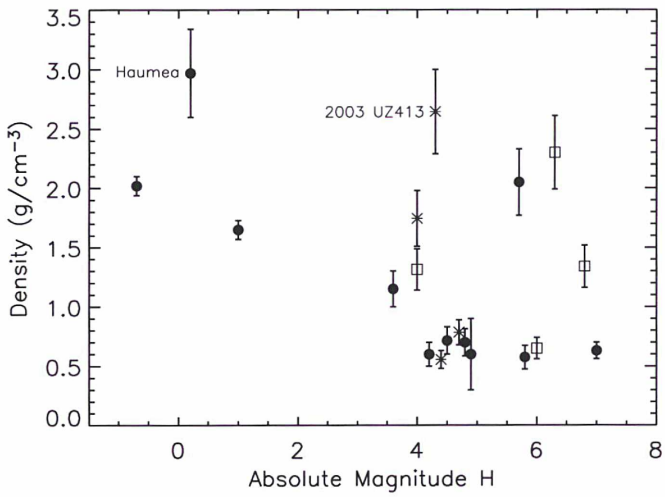

Figure 4.23 – Estimated density ranges of TNOs (including Centaur (95626) 2002 GZ_{32}) as a function of their absolute magnitude H. Data from Perna et al. (2009, asterisks), Dotto et al. (2008, open squares), and Sheppard et al. (2008) and references therein, filled circles.

As mentioned in section 1.4.3, Sheppard et al. (2008) proposed, based on available data before this thesis, the existence of a size/density trend for TNOs, with larger (brighter) objects being denser than smaller (fainter) ones. The authors suggested that it could be due to different porosity and/or different rock/ice mass fraction for bodies of different dimensions. I investigated such a relationship on the basis of the results presented in this thesis.

Employing the entire sample (19 objects) shown in Fig. 4.23, the Pearson correlation coefficient (see Eq. 4.2) between densities and absolute magnitudes has been computed, deriving a value of $r = -0.46$. From the formula (e.g., Taylor 1997):

$$P(|r| \geq r_0) = \frac{2\,\Gamma\,\frac{(N-1)}{2}}{\sqrt{\pi}\,\Gamma\,\frac{(N-2)}{2}} \int_{|r_0|}^{1} (1-r^2)^{\frac{(N-4)}{2}}\,dr \qquad (4.5)$$

where Γ is the Gamma function, it is possible to calculate that the probability that N=19 measurements of two uncorrelated variables would yield $|r| \geq r_0 = 0.46$ is about 4.8%, so the trend can be considered statistically significant. Nevertheless, it is evident that the sample includes several objects with similar absolute magnitudes but very different estimated densities. This may be due to dissimilar internal structures of TNOs with comparable

dimensions, or alternatively to differences in size among TNOs of similar absolute magnitude. The small sample of TNO albedo measurements presently available in the literature does not allow us to solve the ambiguity between brightness and dimensions, but the latter case is unlikely since albedos and sizes of TNOs seem to be correlated, with larger bodies having higher albedos (Stansberry et al. 2008). The hypothesized dimension/density relationship is also strongly influenced by a single object, (136108) Haumea: disregarding this, the correlation coefficient drops to -0.29.

Increasing the available sample of reliable albedo measurements (to reduce the ambiguity between brightness and size) and, especially, of density estimations, seem to be necessary to investigate the existence of a relationship between TNO densities and dimensions. Moreover, as already pointed out in section 1.4.3, TNO density estimations, although reasonable given the current knowledge and understanding of the physical nature of these bodies, should be improved by replacing the fluid assumption with a more complex picture including internal stresses. This is one of my objectives for the near future.

Conclusions and perspectives

In the framework of my PhD thesis work, I investigated the asteroid targets of the Rosetta space mission, (2867) Steins and (21) Lutetia, and the minor bodies of the outer Solar System, namely Centaurs and Trans-Neptunian Objects.

For what concerns Steins, I acquired (April 2008, TNG telescope), reduced, and analysed low phase angle visible photometric and spectroscopic data. Further photometric data from an observational campaign of Steins carried out in Spring 2008 by collaborators have been combined in the analysis.

Several results have been derived:

- from the analysis of V-band and R-band light curves, a synodical rotational period of 6.057 ± 0.003 hours was computed, while the lower limit to the axis ratio a/b resulted to be 1.20 ± 0.02. A $V - R$ color index of 0.51 ± 0.03 mag was computed.

- according to the Bowell et al. (1989) formalism, the magnitude-phase dependence was investigated, computing the slope parameter $G_R = 0.42 \pm 0.02$ (a value typical of E-type asteroids) and the absolute magnitude $H_R = 12.81 \pm 0.03$.

- eight visible spectra were acquired at different rotational phases, covering about 30% of the light curve. All of them are almost flat and exhibit an absorption feature centered on about 0.49 μm, which is usually attributed to sulfides. The similarity between all of the spectra suggests that the surface is quite homogeneous. The spectral behavior of Steins is confirmed to be that typical of E-type asteroids, and its surface composition is similar to enstatite achondrite meteorites enriched in oldhamite.

These results constituted the last ground-based dataset for Steins prior to the Rosetta fly-by (September 2008), providing a fundamental basis for the

calibration, analysis, and interpretation of imaging and spectroscopic data acquired by the instruments OSIRIS and VIRTIS onboard the spacecraft.

As for Lutetia, I acquired (November 2008, TNG telescope), reduced, and analysed thirteen visible spectra, covering the whole rotational period of this main belt asteroid.

All of them exhibit absorption features centered at about 0.47-0.48 μm and around 0.6 μm. Spectral slopes evidence a variation through the rotational phase, suggesting that some inhomogeneities must be present in a portion up to 20% of the observed surface of Lutetia. These inhomogeneities can be due to differences in the chemical/mineralogical composition, as well as to the (already suggested) presence of craters in the northern hemisphere of Lutetia.

These results are important to improve our physical knowledge of this very interesting object, and will represent a basis for the calibration and interpretation of the data acquired by the instruments onboard Rosetta, which will fly-by Lutetia on July 2010.

I took part in a two-year Large Programme started in October 2006 at ESO to study Centaurs and Trans-Neptunian Objects. I carried out four observing runs; I reduced and analysed visible and near-infrared photometric data, and ISAAC spectroscopic observations; I contributed to the interpretation of the spectra, and I took in charge the analysis and interpretation of the visible and near-infrared photometric dataset (colors and light curves).

Hereafter the obtained results:

- visible spectra for 18 TNOs and 10 Centaurs were obtained, confirming that diverse surface compositions are present among these populations, with spectral slopes in the range $\sim$ 1 to 51 % / 10^3 Å. All of the objects showed a featureless visible spectrum, with the exceptions of Chariklo and Typhon which present faint features at 0.62-0.65 μm, attributed to aqueously altered material. Also the spectrum of plutino 2003 AZ_{84} appears featureless, while a faint broad feature centered around 0.7 μm and attributed to aqueous alteration was seen in two previously published spectra of this object (Fornasier et al. 2004; Alvarez-Candal et al. 2008), suggesting possible surface heterogeneity.

- the obtained visible spectra have been combined with literature data (for a total sample of 20 Centaurs and 53 TNOs) to analyse their spectral slope distribution. Resonant, scattered and detached TNOs, as

well as Centaurs, resulted very similar from this point of view, while a lack of very red objects is evident among classical TNOs. Nevertheless observational bias effects cannot be excluded, because of the smaller mean size of the cold (red) population with respect to the bluer hot population in the classical belt.

- performing a Spearman rank analysis some correlations between visible spectral slope and orbital elements have been found, the strongest being for scattered TNOs, which show lower slope values with increasing eccentricity. It has to be noted that in this case the used sample is not statistically significant, but this trend confirms the results from Santos-Sanz et al. 2009, based on visible color indices. Classical TNOs present lower slope values with increasing inclination, but no correlation is found for inclinations below about 12°, in agreement with Peixinho et al. 2008. A weaker anticorrelation between slope and eccentricity is also found for classical TNOs. Resonant TNOs present a positive correlation between slope and eccentricity, as well as Centaurs do. This supports the suggestion by Peixinho et al. (2004) that the Centaur population could originate from Plutinos, and not from scattered TNOs (the two best candidate sources from a dynamical point of view), considering the above-mentioned strong anticorrelation between slope and eccentricity found for SDOs.

- based on visible to near-infrared spectra, the surface composition of TNOs and Centaurs has been modeled using the radiative transfer formulations by Hapke (1981, 1993) and Shkuratov et al. (1999). In this thesis I report the case of (50000) Quaoar, for whose surface molecular nitrogen was unexpectedly found to be an important ($\sim$ 20%) constituent. The modelling of six further objects is currently ongoing.

- visible and near-infrared photometric colors of 45 objects were obtained within the ESO Large Programme, 19 of them have their colors reported for the first time ever. From the comparison with previous works, hints of heterogeneous surfaces have been found for seven objects.

- for 38 out of the 45 observed objects the taxomomic classification (Barucci et al. 2005a) was derived. Nineteen objects are classified for the first time ever, which constitutes about a 14% increase of the sample of 132 objects analysed by Fulchignoni et al. (2008) using the available literature before the ESO-LP.

- taking into account all of these 151 objects an analysis of the taxa distribution with respect to dynamical properties has been performed. Centaurs clearly show their already known color bimodality (BR, RR), IR-types are concentrated in the resonant and classical dynamical classes, while RR-types dominate the classical TNOs. BR and RR classes dominate the population up to semimajor axis $\sim$ 30 AU, while all the four taxa are well represented at greater distances from the Sun. RR and BB classes are more abundant at low and high orbital inclinations, respectively, which associates these objects with the dynamically "cold" and "hot" populations.

- light curves of 12 objects were acquired. For 9 of them the rotational period and the lower limit to the axis ratio a/b were estimated. 2003 UZ_{413} emerged as the second most rapid rotator among TNOs, after (136108) Haumea.

- an estimation of the density of these nine objects has been attempted, assuming to deal with cohesionless and strengthless bodies. The density/dimension relationship for TNOs suggested by Sheppard et al. (2008) was investigated adding these new results to literature data. The trend could be considered statistically significant, but the limited sample and the presence of objects of similar absolute magnitude with completely different estimated densities prevent from assessing its validity. Increasing the sample of reliable albedo measurements (to reduce the ambiguity between brightness and size) and of density estimations seem to be necessary to investigate the existence of such a relationship. Moreover, the fluid assumption should be replaced with a more complex picture including internal stresses.

Future perspectives

Several research projects which started during my PhD are still going on. Among them:

- I am the Principal Investigator (P.I.) of the programme "Rotations and densities of the icy bodies of the outer Solar System", performed at the TNG. This project has been already awarded with 10 nights, during which the light curves of 10 Centaurs and TNOs have been acquired. The obtained data are presently under reduction, and their analysis will permit to further investigate the density statistics of the minor bodies of the outer Solar System.

- I am involved in a programme performing visible photometry of Centaurs and TNOs at the TNG, in support of a Key Program at the Herschel Space Telescope. To date, 17 objects have been observed during the 13 awarded nights, and 4 further nights have been allocated on June 2010. Besides being fundamental to retrieve the albedo and size of the selected targets in combination with thermal measurements, these data are important *per se*, since the obtained colors will give hints on their surface composition and will be used to classify them in the 4 TNO taxa defined by the Barucci scheme.

- I will work on data of the asteroid (4) Vesta, obtained with the NACO instrument at the VLT. Making use of the adaptive optics system, high resolution imaging and spectroscopy of different parts of the asteroid surface have been performed. These data are particularly important in view of the visit of the NASA-Dawn space mission, which will orbit Vesta in the period October 2011 - May 2012.

- I am involved in a programme at the TNG performing NIR spectroscopy of V-type asteroids not belonging to the Vesta dynamical family. The aim of the study (to date, 2.5 awarded nights, 3 observed objects) is to investigate the spectral properties of the targets, looking for possible parent bodies for V-types alternative of Vesta, and to study in an extended way the effects of space weathering processes on V-type asteroid surfaces, through a comparison with new laboratory experiments we are currently performing on basaltic achondrite meteorites.

In the middle term, I want to profit of X-Shooter, the new spectrograph of the ESO-VLT, to characterize the minor bodies of the Solar System. X-Shooter is presently the only available instrument which cover in a single exposure the spectral range from the ultraviolet to the near-infrared, which is particularly useful in the assessment of the surface composition of atmosphereless bodies.

I want to extend my research interests to the mid- and far-infrared, e.g. studying the thermal emission of TNOs with the Herschel Space Telescope.

Moreover, I will give my contribution to projects regarding the next space missions to the minor bodies, e.g. sample return missions from primitive asteroids, which could allow us to study with unprecedented detail unaltered material in terrestrial laboratories, casting further light on the formation and early evolution of the Solar System.

Appendix A

The G-mode technique

The G-mode method (Coradini et al. 1977) allows the user to obtain an automatic clustering of a statistical sample containing N objects described by M variables (for a total of $M \times N$ degrees of freedom, which must be > 100) in terms of homogeneous taxonomic groups with no a priori grouping criteria and taking into account the instrumental errors in measuring each variable. The method also gives indications on the relative importance of the variables in separating the groups. The original multivariate sample is collapsed into an univariate sample through successive transformations. The new variable (g) is normalized to a quasi-Gaussian distribution with a mean equal to 0 and a variance equal to 1; N' out of the N elements are selected on the basis of a test of the hypothesis of membership in the first group, which comes out through an automatic choice once a starter is selected. The starter is defined as the set of the three elements having the minimum reciprocal distance. The selection procedure is iterated using as starter all the selected elements until their number N' does not change. The method is then iterated on the $N - N'$ elements left, in order to identify the second group, composed of N'' elements. The iteration proceeds on $N - (N' + N'')$ elements, and so on, until all the elements are classified into homogeneous groups. Homogeneous means that each group belongs to the same statistical population characterized by mean values of variables and relative standard deviations. The membership of an element in a given group, or the selection criteria, is based on the statistical inference rules, the only a priori choice in the decision process being that of the confidence level defined as the probability of accepting the tested hypothesis. The user selects the confidence level that corresponds to a given critical value Q.

The G-mode analysis has been extended (Fulchignoni et al. 2000) to assign to one of the already defined taxonomic groups any object for which the same set of variables becomes available. Moreover, even if a subset of the

variables used in the initial development of the taxonomy is known for an object, the algorithm allows the user to assign a preliminary indication of its likely group. The lack of information on a variable is reflected by the fact that an object could be assigned to two different classes when that variable is the one that discriminates between these classes.

Appendix B

List of publications

Refereed papers:

1. **Perna, D.**, Dotto, E. Lazzarin, M., Magrin, S., Fulchignoni M., Barucci, M.A., Fornasier, S., Marchi, S., Barbieri, C. 2010. *Inhomogeneities on the surface of 21 Lutetia, asteroid target of the Rosetta mission.* Submitted to A&A.

2. De Luise, F., Dotto, E., Fornasier, S., Barucci, M.A., Pinilla-Alonso, N., **Perna, D.**, Marzari, F. 2010. *A Peculiar Family of Jupiter Trojans: the Eurybates.* Submitted to Icarus.

3. Merlin, F., Barucci, M.A., de Bergh, C., Fornasier, S., Doressoundiram, A., **Perna, D.**, Protopapa, S. 2010. *Surface composition and physical properties of several Trans-Neptunian objects from the Hapke scattering theory and Shkuratov model.* Submitted to Icarus.

4. **Perna, D.**, Barucci, M.A., Fornasier, S., DeMeo, F.E., Alvarez-Candal, A., Merlin, F., Dotto, E., Doressoundiram, A., de Bergh, C. 2010. *Colors and taxonomy of Centaurs and Trans-Neptunian Objects.* A&A, 510, A53.

5. **Perna, D.**, Dotto, E., Barucci, M.A., Rossi A., Fornasier S., de Bergh, C. 2009. *Rotations and densities of Trans-Neptunian Objects.* A&A, 508,451.

6. Fornasier, S., Barucci, M.A., de Bergh, C., Alvarez-Candal, A., DeMeo, F., Merlin, F., **Perna, D.**, Guilbert, A., Delsanti, A., Dotto, E., Doressoundiram, A. 2009. *Visible spectroscopy of the new ESO Large Program on Trans-Neptunian Objects and Centaurs: final results.* A&A, 508, 457.

7. Dalle Ore, C.M., Barucci, M.A., Emery, J.P., Cruikshank, D.P., Dalle Ore, L.V., Merlin, F., Alvarez-Candal, A., de Bergh, C., Trilling, D.E., **Perna, D.**, Fornasier, S., Mastrapa, R.M.E., Dotto, E. 2009. *Composition of KBO (50000) Quaoar*. A&A, 501, 349.

8. Dotto, E., **Perna, D.**, Fornasier, S., Belskaya, I.N., Barucci, M.A., Shevchenko, V.G., Krugly, Yu.N., Gaftonyuk, N.M., Tereschenko, I.A., Scipioni, F., De Luise, F. 2009. *Photometric and spectroscopic investigation of 2867 Steins, target of the Rosetta mission. Ground-based results prior to the Rosetta fly-by*. A&A, 494, L29.

9. DeMeo, F.E., Fornasier, S., Barucci, M.A., **Perna, D.**, Protopapa, S., Alvarez-Candal, A., Delsanti, A., Doressoundiram, A., Merlin, F., de Bergh, C. 2009. *Visible and near-infrared colors of Transneptunian objects and Centaurs from the second ESO large program*. A&A, 493, 283.

10. Dotto, E., **Perna, D.**, Barucci, M.A., Rossi, A., de Bergh, C., Doressoundiram, A., Fornasier, S. 2008. *Rotational properties of Centaurs and TransNeptunian Objects. Lightcurves and densities*. A&A, 490, 829.

Abstracts & proceedings:

1. **Perna, D.**, Fornasier, S., Barucci, M.A., DeMeo, F., Merlin, F., Alvarez-Candal, A., Guilbert, A., Delsanti, A., Dotto, E., Doressoundiram, A., Protopapa, S., de Bergh, C. 2009. *Colors and Taxonomy of Tnos and Centaurs*. Bulletin of the American Astronomical Society, 41, 65.10.

2. Dalle Ore, C.M., Barucci, M.A., Emery, J.P., Cruikshank, D.P., Dalle Ore, L.V., Merlin, F., Alvarez-Candal, A., de Bergh, C., **Perna, D.**, Fornasier, S., Mastrapa, R.M.E., Dotto, E. 2009. *Composition of KBO (50000) Quaoar*. Bulletin of the American Astronomical Society, 41, 663.

3. **Perna, D.**, Dotto, E., Barucci, A., Rossi, A., de Bergh, C., Doressoundiram, A., Fornasier, S. 2009. *Light Curves and Densities of Centaurs and Trans-Neptunian Objects from the ESO Large Program*. Bulletin of the American Astronomical Society, 40, 483.

4. Merlin, F., Barucci, M., Fornasier, S., de Bergh, C., **Perna, D.**, Doressoundiram, A., Delsanti, A. 2008. *Surface Analyses Of The Centaur Echeclus And Trans-neptunian Objects.*. Bulletin of the American Astronomical Society, 40, 482.

5. DeMeo, F.E., Fornasier, S., Barucci, M.A., **Perna, D.**, Protopapa, S., Alvarez-Candal, A., Delsanti, A., Doressoundiram, A., Merlin, F., de Bergh, C. 2008. *Visible and Near-infrared Colors of TNOs from the Second ESO Large Program.* Bulletin of the American Astronomical Society, 40, 482.

6. De Luise, F., Dotto, E., Fornasier, S., Barucci, M.A., **Perna, D.**, Marzari, F. 2008. *The Nature of the Eurybates Family.* Bulletin of the American Astronomical Society, 40, 438.

7. **Perna, D.**, De Luise, F., Dotto, E., Boubin, G., Fratto, L. 2008. *Physical characterization of asteroid targets of space missions.* Memorie della Società Astronomica Italiana Suppl., 12 , 83.

8. DeMeo, F.E., Fornasier, S., Barucci, M.A., Protopapa, S., **Perna, D.**, Alvarez-Candal, A., Delsanti, A., Doressoundiram, A., Merlin, F., de Bergh, C. 2008. *Visible and Near-Infrared Colors of KBOs and Centaurs from the Second ESO Large Program.* LPI, 1405, 8189.

9. **Perna, D.**, Dotto, E., Barucci, M.A., Rossi, A., de Bergh, C., Doressoundiram, A., Fornasier, S. 2008. *Rotational Properties of Centaurs and Trans-Neptunian Objects: Results from the ESO Large Program.* LPI, 1405, 8110.

10. Barucci, M.A., Merlin, F., Guilbert, A., Fornasier, S., de Bergh, C., Doressoundiram, A., Alvarez, A., Dumas, C., Hainaut, O., Belskaya, I., Bagnulo, S., Delsanti, A., Protopapa, S., Tozzi, G., Muinonen, K., **Perna, D.**, Peixinho, N. 2007. *Characterization of TNOs' Surface Properties: Preliminary Results of a Large VLT Programme.* Bulletin of the American Astronomical Society, 39, 509.

11. Dotto, E., **Perna, D.**, Barucci, M.A., de Bergh, C., Doressoundiram, A., Fornasier, S. 2007. *Rotational Properties of Centaurs and KBOs.* Bulletin of the American Astronomical Society, 39, 492.

12. **Perna, D.**, Dotto, E., De Luise, F., Barucci, M.A., Fulchignoni, M., Fornasier, S. 2007. *Physical Properties of 21 Lutetia, Target of the Esa Space Mission Rosetta.* Bulletin of the American Astronomical Society, 39, 448.

Annexe C

Résumé en français

Les petits corps du Système Solaire sont les derniers vestiges des planétésimaux qui ont formé les planètes et leurs satellites. Leur étude peut fournir d'importantes informations sur les processus qui ont gouverné la formation et l'évolution du système solaire aux différentes distances héliocentriques.

Pendant ma thèse j'ai concentré mes recherches sur les astéroïdes qui sont cibles de la mission spatiale Rosetta, c'est-à-dire (2867) Steins et (21) Lutetia, et sur les Centaures et les Objets transneptuniens (Trans-Neptunian Objects, TNOs).

Au sujet des astéroïdes cibles de Rosetta, la connaissance de leur propriétés physiques est indispensable que ce soit pour l'interprétation des données acquises par la sonde, ou bien pour la "calibration" des données sol concernant tous les petits corps qui ne seront jamais visités par des missions spatiales. J'ai donc participé à deux campagnes d'observation conduites au télescope TNG (Telescopio Nazionale Galileo) pour améliorer la caractérisation physique de Steins et Lutetia avant le rendez-vous avec la sonde Rosetta. Les données de photométrie et spectroscopie acquises sur Steins ont permis d'obtenir des informations sur la taille, la forme, la période de rotation, et la composition de la surface de l'astéroïde. Pour ce qui concerne Lutetia, les résultats obtenus indiquent que sa surface n'est pas totalement homogène dans l'hémisphère Nord. Ce pourrait être du à des compositions différentes et/ou à la présence de structures sur la surface.

J'ai participé au "Large Programme" conduit à l'ESO (European Southern Observatory) par M.A. Barucci pour l'étude de Centaures et TNOs, avec l'acquisition, la réduction, et l'analyse de données photométriques et spectroscopiques, dans les régions du visible et du proche infrarouge. La composition de surface des objets examinés a été étudiée et modélisée par une comparaison avec des spectres synthétiques. Sur la base des mesures de photométrie, la taxonomie des objets a pu être établie, et une analyse statistique a été

réalisée en utilisant la littérature disponible, à la recherche de liaisons entre taxonomie et propriétés dynamiques des petits corps du Systeme Solaire externe. Des données photométriques supplémentaires ont été acquises et analysées pour examiner les propriétés rotationnelles de 12 objets, et donc obtenir des informations sur leur forme et leur structure interne. Ces données ont permis de mettre en doute une corrélation qui avait été suggérée entre la taille et la densité des TNOs.

Chapitre 1 : les petits corps

L'étude des petits corps nous permet de lever le voile sur l'origine et l'évolution primordiale du Système Solaire, puisque, selon la théorie (Safronov 1979) la plus généralement admise, ils représentent "les vestiges" des planetesimaux existant dans le disque proto-planétaire. Bien que les petits corps aient été affectés par une évolution thermique et dynamique, et par des collisions, ils gardent la memoire des conditions initiales qui ont existé dans la nébuleuse solaire il y a environ 4.6 milliards d'années. Ainsi, interpréter leurs propriétés physiques et orbitales actuelles peut nous dire beaucoup du gradient de la composition de la nébuleuse et des processus qui ont gouverné les premières phases du Système Solaire aux différentes distances héliocentriques.

Les petits corps sont divisés dans des "groupes" basés sur leurs propriétés orbitales et physiques actuelles :

- Objet transneptuniens (TNOs) : après la découverte de Pluton, le premier objet ayant une orbite complètement transneptunienne a été découvert en septembre 1992 (Jewitt et al. 1992; Jewitt & Luu 1993). De nos jours on connaît plus de 1350 objets transneptuniens, et leur étude représente un des sujets les plus remarquables dans la science planétaire contemporaine, puisque ces corps éloignés et glacés conservent le matériel le plus vierge qui peut actuellement être observé. D'un point de vue dynamique, ils sont à leur tour classifiés comme (Fig. 1.1) : *resonant* (en résonance orbitale avec Neptune), *scattered* (objets "épars" sous l'effet de la gravité de Neptune), *detached* (des objets trop éloignés pour pouvoir être affectés par Neptune), et *classical* (la plupart des TNOs, pas en résonance mais avec des orbites stables). Les objet transneptuniens de type "classical" sont habituellement divisés entre une population "froide" (avec des orbites peu inclinées et couleur rouge) et une population "chaude" (avec des orbites fortement inclinées et couleur gris/bleu) (Levison & Stern 2001; Brown 2001; Doressoundiram et al. 2002). Levison & Stern (2001) ont suggéré

que la population chaude s'est formée plus proche au Soleil et a été transportée vers l'extérieur pendant les étapes finales de la formation planètaire.

- Centaures : ce sont des objets qui gravitent autour du Soleil entre Jupiter et Neptune. Les orbites des Centaures sont instables, à l'échelle de $\sim 10^6 - 10^7$ ans : on croit largement qu'ils proviennent des régions transneptuniennes comme conséquence de perturbations gravitationnelles et de collisions (Levison & Duncan 1997; Durda & Stern 2000). L'existence de deux groupes distincts parmi les Centaures a été suggérée (par exemple, Peixinho et al. 2003; Tegler et al. 2008) : un très rouge (comme Pholus) et un avec couleurs neutres (comme Chiron).

- Satellites des planètes : ils peuvent être *irréguliers* (sur une orbite distante, inclinée et souvent rétrograde), qu'on croit avoir été capturés, et *réguliers* (orbitant relativement proche de la planète, sur une orbite prograde), qui se sont formés "in situ".

- Troyens : ils sont situés autour des points de Lagrange du système planète-Soleil. On connait environ 3700 Troyens de Jupiter, 4 Troyens de Mars, et 6 troyens de Neptune.

- Astéroïdes de la ceinture principale : ils represent le principal groupement, avec plusieurs centaines de milliers d'astéroïdes connus. Dans cette zone la formation planétaire a été empêchée par les perturbations gravitationnelles de Jupiter.

- Objets géocroiseurs (Near Earth Objects, NEOs) : évoluant à proximité de la Terre, avec périhélie à moins de 1.3 UA. Ils proviennent de la ceinture principale (Morbidelli et al. 2002).

La variété présentée par les petits corps aux différentes distances héliocentriques est en raison directe du gradient de composition de la nébuleuse primordiale avec la distance du Soleil. Dans le disque interne, chauffé par le Soleil, les glaces et les gaz ne pouvaient pas condenser, en conséquence aujourd'hui on trouve ici principalement des minéraux rocheux et métalliques. Au contraire, dans le disque externe, les glaces et les gaz, aussi bien que les silicates et les composés métalliques, pouvaient condenser. La compréhension des propriétés physiques (aussi bien que dynamiques) des populations de petits corps peut donc fournir des informations cruciales pour enquêter sur la structure et l'évolution primordiale du Système Solaire aux différentes distances du Soleil.

Des techniques d'observation différentes peuvent être adoptées pour caractériser la nature physique des petits corps. Parmi eux, les plus largement utilisées sont *la photométrie* et *la spectroscopie de réflectance.*

Pour ce qui concerne la photométrie, les indices de couleur fournissent une première estimation des propriétés de la surface. L'étude de la courbe de phase (c'est-à-dire de la relation entre la magnitude et l'angle de phase) permet d'avoir des renseignements sur la taille et l'albédo de l'objet. L'analyse des courbes de lumière apporte des informations sur la période et l'orientation de l'axe de rotation, la forme, et la structure à grande échelle de la surface de l'objet.

La spectroscopie dans les domaines du visible et de l'infrarouge proche constitue la technique la plus sensible et largement appliquée pour la caractérisation de la surface des petits corps. Les paramètres spectraux (par exemple, la position, la profondeur, la forme de la bande) de ces absorptions sont liés à la composition chimique spécifique de la surface, toutefois l'interprétation est difficile, puisque les différent éléments se combinent de façon non linéaire. La manière la plus simple pour indentifier les éléments superficiels sur le petits corps est la comparaison avec des spectres de laboratoire de météorites, minéraux, et glaces (Fig. 1.6). Une image plus détaillée des compositions de surface peut être obtenue avec la *modélisation spectrale*, c'est à dire le calcul de spectres synthétiques basés sur des théories de transfert radiatif et des mesures en laboratoire des constantes optiques (Fig. 1.7). Les deux principales théories qui sont utilisées pour modéliser les surfaces des petits corps ont été développées par Hapke (1981, 1993) et Shkuratov et al. (1999).

Parmi les processus qui peuvent modifier les propriétés spectrales, on cite l'*altération aqueuse*, qui est une modification chimique d'un matériau par son interaction avec de l'eau liquide, et le *"space weathering"*, c'est-à-dire le rayonnement cosmique, les impacts de grains interstellaires, le rayonnement UV, le vent solaire, ainsi que les collisions, qui engendrent un changement de la surface, donc du spectre.

Le Système Solaire interne : jusqu'à Jupiter

Dans le Système Solaire interne, nous trouvons des astéroïdes appartenant à différentes populations : NEOs, objets de la ceinture principale, Troyens de Jupiter. Comme déjà dit, leur surfaces présentent principalement des minéraux métalliques et rocailleux.

Depuis les années 1970, plusieurs auteurs ont tenté de définir des schémas taxonomiques basés sur les propriétés d'observation (spectre, couleurs, albédo, etc) des astéroïdes. L'intention commune de ces taxonomies est de grouper les astéroïdes dans différentes classes que l'on pense correspondre à une com-

position de surface et/ou évolution thermique similaire. Il est à noter que, bien que l'appartenance à différentes classes est probablement un signe d'une différence substantielle de la composition, l'inverse n'est pas forcément vrai. A savoir, deux petits corps appartenant au même taxon pourraient ne pas avoir la même composition minéralogique. Néanmoins, les membres des groupes sont censés être composés d'un nombre limité "d'assemblages". Une taxonomie très robuste est celle proposée par Tholen (1984, 1989), basée sur les couleurs spectrophotométriques obtenues au cours des la *survey* ECAS (Zellner et al. 1985), qui a observé 589 astéroïdes dans la gamme de longueur d'onde de 0.3 à 1.1 μm (tableau 1.1).

On croit que les météorites appartenant au même groupe proviennent du même objet ou de plusieurs objets "similaires", et des analogues météoritiques ont été évalués pour les différentes classes taxonomiques des astéroïdes (tableau 1.1). Les différentes histoires thermiques sont censées avoir produit les différents types pétrologiques (fig. 1.10) : les chondrites ordinaires (semblables aux astéroïdes de type Q) ont subi une évolution thermique modeste pendant l'âge du système solaire, tandis que les chondrites carbonées (similaires aux astéroïdes de type C) sont plus primitives. Dans certains cas, une relation forte a été trouvée entre un groupe de météorites et un objet candidat parent. Par exemple, sur la base de contraintes dynamiques et spectroscopiques, il a été suggéré que (6) Hebe pourrait être une source importante des chondrites ordinaires (Migliorini et al. 1997; Gaffey & Gilbert 1998).

À ce jour, plusieurs astéroïdes ont été étudiés par les missions spatiales. L'étude *in situ* des astéroïdes fournit des informations essentielles, indisponibles à partir des observations au sol, et a grandement amélioré nos connaissances sur la nature de ces corps. Les objets visités ont été étudiés en détail, en obtenant des données sur leur taille, forme, rotation, et propriétés de surface. Les survols pouvent aussi nous donner la masse de l'astéroïde, avec une détermination de la densité moyenne après une estimation fiable du volume. Toutes ces informations peuvent conduire à des indications importantes sur la physique de l'astéroïde étudié, et la comparaison des résultats obtenus de la Terre et ceux obtenus "in situ", fournira l'étalonnage (*ground truth*) pour les données sol des astéroïdes qui ne seront jamais visités par une mission spatiale.

Le Système Solaire externe : loin du Soleil

Dans les régions externes du Système Solaire, les températures de formation étaient suffisamment froides pour permettre aux glaces de condenser et rester stables, et ainsi les Centaures et TNOs observables de nos jours sont un mélange de roches et de glaces.

Un système de taxonomie fondé sur des indices de couleur a été récemment mis au point pour les TNOs et Centaures par Barucci et al. (2005a), en utilisant l'analyse "G-mode" (Coradini et al. 1977, voir Annexe A). Comme il a déjà été fait dans le passé pour les astéroïdes (voir la section 1.3.1), l'analyse des couleurs des petits corps du Système Solaire externe, éloignés et faibles, fournit une première indication sur leur différences de compositions et/ou d'histoires possibles. Une désignation à deux lettres pour les groupes identifiés est introduite (RR, IR, BR, BB) pour distinguer la taxonomie des TNOs de la taxonomie des astéroïdes (figure 1.14).

Même si seulement les TNO les plus brillants ont été étudiés par spectroscopie, en raison de la faiblesse de ces corps, des résultats intéressants ont été obtenus sur la composition de leur surfaces. Une variété remarquable apparaît, avec la présence de glaces sur plusieurs objets appartenant à l'ensemble des quatre classes taxonomiques. Barucci et al. (2008a) ont identifié quatre différents types spectraux de TNOs : dominés par le méthane ; dominés par la glace d'eau ; objets qui presentent bandes d'absorption de la glace d'eau et du méthanol ; sans traits marquants.

Les TNOs les plus grands ont atteint des formes d'équilibre réguliéres en conséquence de pressions internes élevées (Rabinowitz et al. 2006). En supposant un TNO comme un corps "fluide", sa densité peut être évaluée par des considérations sur la stabilité rotationnelle. Donc l'analyse de sa courbe de lumière permet d'obtenir des indications sur sa structure interne. En utilisant les données disponibles avant cette thèse, Sheppard et al. (2008) ont proposé l'existence d'une relation entre la dimension et la densité, avec les TNOs les plus grands (lumineux) étant plus denses que les plus petits (faibles). Ils a été suggéré que cela pourrait être causé par différentes porosités et/ou rapport roche/glace pour les corps de différentes tailles (fig. 1.16).

Chapitre 2 : acquisition/réduction des données

Dans le cadre de mon doctorat, j'ai surtout étudié les astéroïdes cibles de la mission spatiale Rosetta (Steins et Lutetia), et les petits corps du Système Solaire externe (Centaures et Objets transneptuniens). J'ai effectué plusieurs observations, avec le New Technology Telescope (NTT) et le Very Large Telescope (VLT) de l'Observatoire Européen Austral (European Southern Observatory, ESO), et avec le Telescopio Nazionale Galileo (TNG). J'ai réduit et analysé celles-ci et d'autres données afin de caractériser les objets observés.

En particulier :

- J'ai acquis, réduit, et analysé des données photométriques et spectroscopiques dans le domaine du visible sur (2867) Steins, le premier

astéroïde objectif de la mission spatiale Rosetta. Les observations ont été effectuées au TNG en avril 2008, en utilisant l'instrument DOLORES. Des données supplémentaires provenant de collaborateurs ukrainiens ont été combinées dans l'analyse. Tous les détails sur la campagne d'observation de Steins, ainsi que les résultats obtenus, sont donnés dans la section 3.1.

- J'ai acquis, réduit, et analysé des données spectroscopiques dans le domaine du visible sur (21) Lutetia, le deuxième astéroïde cible de la mission spatiale Rosetta. Les observations ont été effectuées avec le Telescopio Nazionale Galileo (TNG) en novembre 2008, en utilisant l'instrument DOLORES. Ce travail est présenté dans la section 3.2.

- J'ai été (et je suis encore) fortement impliqué dans un grand programme à l'ESO sur les Centaures et les TNOs (que je noterai par la suite ESO-LP), pendant lequel des données sur 50 objets ont été obtenues pour un total de 500 heures d'observation couvrant les années 2006-2008. J'ai effectué deux observations au VLT, avec les instruments FORS2 et ISAAC, et deux avec l'instrument EMMI au NTT. J'ai réduit et analysé toutes les données EMMI et la plupart des données ISAAC obtenues dans le cadre de l'ESO-LP. J'ai contribué à l'interprétation des données spectroscopiques, et, en particulier, j'ai pris en charge l'analyse et l'interprétation des données photométriques dans le visible et proche infrarouge. Les résultats obtenus sont présentés dans le chapitre 4.

Toutes les données visibles photométriques et spectroscopiques présentées dans cette thèse ont été réduites en utilisant le progiciel ESO-MIDAS. Les données de l'infrarouge proche ont été réduites en utilisant aussi le *pipeline* développé par l'ESO pour ISAAC. Les étapes de la réduction des données ont suivi des procédures standard ; le lecteur est invité à se référer à la version en anglais pour plus de détails.

Chapitre 3 : les astéroïdes cibles de Rosetta

Au cours de son voyage de 10 ans vers la comète 67P/Churyumov-Gerasimenko, la sonde ESA-Rosetta effectue également le survol de deux astéroïdes de la ceinture principale, (2867) Steins et (21) Lutetia. Le survol de Steins a eu lieu en septembre 2008, tandis que celui avec Lutetia est prévu en juillet 2010.

(2867) Steins

Steins est un petit (quelques kilomètres) astéroïde de la ceinture principale, et son étude n'a commencé qu'en début 2004, quand il a été inclus dans la liste des cibles possibles de Rosetta. Lamy et al. (2008b) ont calculé une période sidérale de 6.04681±0.00002 heures. Des observations spectroscopiques dans les domaines du visible et du proche infrarouge obtenues par Barucci et al. (2005c) ont révélé un comportement spectral similaire à celui des astéroïdes de type E (considérés comme corps différenciés qui ont connu un chauffage important). En particulier, son spectre ressemble à ceux du sous-type E[II] (d'après la classification par Gaffey & Kelley 2004 et Clark et al. 2004), avec la présence d'une absorption très forte à $\sim$ 0.5 μm, une absorption plus faible à environ 0.96 μm, et un comportement plat et sans de caractéristiques au-delà de 1 μm. Ces bandes d'absorption sont caractéristiques de l'oldhamite, un mineral de sulfure de calcium qui n'est présent que dans des assemblages résultant d'un processus chimique de réduction très fort, tels que les aubrites (météorites achondrites enstatitiques). Les caractéristiques d'absorption résultent probablement de la présence de traces de fer bivalent dans le sulfure. L'albédo de Steins a été mesuré comme p_V=0.45±0.10 (Fornasier et al. 2006) et p_V=0.34±0.06 (Lamy et al. 2008a), une valeur élevée cohérente avec la classification de type E proposée par le comportement spectroscopique. Le spectre d'émissivité entre 5.2 et 38 μm mésuré par Spitzer est également conforme à celui des aubrites et des minéraux à enstatite (Barucci et al. 2008b), et confirme le classement E.

Jusqu'en avril 2008, aucune observation photométrique ni courbe de lumière de Steins n'étaient disponibles pour des angles de phase $\alpha < 7°$, bien que cette région soit particulièrement importante pour la détermination de la magnitude absolue H et du paramètre de pente G des astéroïdes (voir la section 1.2.1).

Pour étudier et évaluer les propriétés physiques de Steins avant la rencontre avec Rosetta, j'ai participé à une campagne d'observation (printemps 2008) au cours de laquelle ont été effectuées de la spectroscopie visible et de la photométrie visible de l'astéroïde à petits angles de phase. Ces observations étaient importantes pour compléter l'ensemble des données sol, et pour calculer les paramètres physiques de Steins qui sont fondamentaux pour calibrer correctement l'imagerie et les données spectroscopiques acquises par les instruments embarqués sur Rosetta.

Les observations photométriques ont été effectuées à l'Institut d'Astronomie de l'Université Nationale de Kharkiv Karazin (réflecteur de 70 cm), au Département Simeiz de l'Observatoire Astrophysique de Crimée (réflecteur

de 1 m), et au TNG (réflecteur de 3.6 m). Au TNG des spectres visibles ont également été acquis au moyen de DOLORES.

Les courbes de lumière dans les filtres V et R sont cohérentes dans les barres d'erreur, et caractérisées par une forme plutôt symétrique (Fig. 3.2). Une période synodique de rotation de $P_{syn} = 6.057 \pm 0.003$ et une limite inférieure au rapport des axes $a/b \geq 1.20 \pm 0.02$ ont été calculées. La couleur résultante est de $V - R = 0.51 \pm 0.03$ mag.

En utilisant aussi des observations publiées antérieurement, obtenues en 2004 - 2008 (Hicks et al. 2004; Weissman et al. 2007; Jorda et al. 2008; Lamy et al. 2008b), la relation entre magnitude et angle de phase a été étudiée selon le formalisme développé par Bowell et al. (1989) pour calculer la magnitude absolue et le paramètre de pente en bande R, résultant dans des valeurs de $H_R = 12.81 \pm 0.03$ and $G_R = 0.42 \pm 0.02$ (une valeur typique des astéroïdes de type E ; Fig. 3.3 et Fig. 3.4).

Les spectres obtenus (Fig. 3.5) présentent le comportement typique des astéroïdes E[II] : tous sont presque plats et sans bandes entre 0.55 et 0.9 μm, et avec la signature d'absorption à 0.49 μm déjà discutée. Il est possible de soutenir que Steins a une composition de surface très homogène.

En utilisant un modèle de transfert radiatif (basé sur la théorie de Hapke), nous avons trouvé que le meilleur spectre synthétique pour reproduire la surface de Steins vient d'un mélange composé de 55% d'aubrite Mayo Belwa et 45% d'oldhamite (ce mélange a un albédo de 0.35 ; Fig. 3.6).

Les résultats présentés dans cette thèse, découlant des dernières données sol obtenues avant le survol de Rosetta (5 septembre 2008), sont particulièrement importantes pour l'étalonnage et l'interprétation des données acquises par la sonde. L'analyse de ces dernières est toujours en cours, mais en général il semble que les données de Rosetta sont bien comparables à celles obtenues au sol, en renforçant le *ground truth*.

(21) Lutetia

Bien que plusieurs observations de (21) Lutetia soient disponibles depuis une vingtaine d'années, la nature de cet astéroïde est encore controversée.

Les observations de Lutetia avec IRAS (InfraRed Astronomical Satellite) ont fourni un diamètre d'environ 96 km et un albédo de 0.22. En raison de la grande valeur d'albédo, confirmée ultérieurement par Mueller et al. (2006), qui ont trouvé une valeur de 0.208 ± 0.025, Lutetia a été classé comme un astéroïde de type M par Barucci et al. (1987) et Tholen (1989). Considérant que les types M ont des propriétés spectrales et des valeurs de l'albédo compatibles avec le métal Fe-Ni, et sont généralement considérés comme les noyaux métalliques d'astéroïdes différenciés exposés après des perturbations catastrophiques, Lutetia était censé être un objet évolué qui a subi une forte

altération thermique. Néanmoins, des observations complémentaires n'ont pas confirmé la nature métallique de Lutetia, en suggèrant plutôt une composition primitive de la surface. Howell et al. (1994) et Burbine & Binzel (2002) ont montré que le spectre infrarouge de Lutetia est exceptionnellement plat par rapport à d'autres astéroïdes de type M. En outre, les observations obtenues par Barucci et al. (2005c) et Birlan et al. (2004) ont suggéré une similitude avec les spectres des chondrites carbonées qui caractérisent les astéroïdes de type C. Aussi les propriétés polarimétriques (Belskaya & Lagerkvist 1996) et les observations avec Spitzer entre 5.2 et 38 μm (Barucci et al. 2008b), ont révélé une analogie aux chondrites carbonées. Plus récemment, Vernazza et al. (2009) ont obtenu des spectres de Lutètia qui semblent indiquer que la composition de la surface de cet objet peut avoir un certain lien avec les chondrites enstatitiques, qui sont cependant plus évoluées.

Par conséquent, même si la plupart des auteurs s'accordent sur la composition primitive de Lutetia, sur la base des données d'observation cet astéroïde semble être un objet énigmatique, atypique, dont la nature est encore loin d'être pleinement comprise.

Afin de renforcer la connaissance de Lutetia avant le survol de Rosetta, j'ai contribué à un étude spectroscopique de cet objet. Des observations ont été menées en Novembre 2008 au TNG, en utilisant l'instrument DOLORES.

Le comportement spectral est similaire dans tous les treize spectres obtenus, mais certaines différences sont évidentes.

Tous les spectres présentent deux caractéristiques spectrales à environ 0.47-0.48 μm et à $\sim$0.6 μm. Ces deux caractéristiques spectrales ont déjà été vues sur les spectres de (21) Lutetia par Lazzarin et al. (2009) et Lazzarin et al. (2004). La profondeur des bandes, par rapport au continuum, est d'environ 1% dans tous les spectres, et ne présente pas de variation évidente.

À l'inverse, comme indiqué dans le tableau 3.6 et montré dans la Fig. 3.9, les pentes spectrales calculées entre 0.6 et 0.75 μm montrent une variation périodique (en particulier, un manque d'homogénéité net qui correspond au spectre # 9). Cette variation de la pente spectrale de Lutetia au cours de la phase de rotation, peut être interprétée comme étant dû à la présence d'inhomogénéités (différente composition minéralogique, ou présence de cratères ou taches d'albédo) sur la partie observée de la surface de l'astéroïde, dans l'hémisphère nord (Carvano et al. 2008 ont suggéré que un ou plusieurs cratères/inhomogénéités peuvent être présents sur la surface de Lutetia).

Ces données sont utiles dans l'évaluation de la nature physique de Lutetia, et constitueront un bon départ pour l'étalonnage, l'analyse, et l'interprétation des données acquises par les instruments à bord de Rosetta.

Chapitre 4 : Centaures et TNOs

Les Objets transneptuniens et les Centaures sont les vestiges les plus vierges du disque proto-planétaire, dans lequel l'accrétion des planétésimaux s'est produite. Par conséquent, leur étude est fondamentale pour la compréhension des conditions existantes dans le Système Solaire primordial, et des processus d'accrétion qui régissent la formation des planètes aux grandes distances héliocentriques.

En octobre 2006, un grand programme (d'une durée de deux ans) a débuté à l'ESO pour étudier les Centaures et les TNOs (ESO-LP).

Dans le cadre de mon travail de thèse, j'ai contribué à ce programme :

- J'ai effectué deux observations (1 nuit chacune) au VLT, en acquérant 8 spectres visibles et 3 spectres en bande J avec les instruments FORS2 et ISAAC, respectivement. J'ai réduit la plupart des données spectroscopiques obtenues avec ISAAC au cours de l'ESO-LP, et j'ai contribué à l'analyse et à l'interprétation des spectres.

- Au cours des observations avec FORS2 et ISAAC mentionnées ci-dessus, j'ai aussi acquis des données photométriques visibles (8 objets, filtres VRI) et dans le proche infrarouge (6 objets, filtres JHK_s). J'ai réduit la plupart des données photométriques infrarouges obtenues dans le cadre de l'ESO-LP, et j'ai pris en charge l'analyse et l'interprétation de l'ensemble des données photométriques V-NIR.

- J'ai effectué deux observations (3 nuits chacune) au NTT, en acquérant les courbes de lumière de 12 Centaures et TNOs avec l'instrument EMMI. J'ai pris en charge la réduction, l'analyse et l'interprétation de l'ensemble des données.

Spectroscopie et modélisation

Dans le cadre de l'ESO-LP, la spectroscopie visible et proche infrarouge a été réalisée au cours de plusieurs observations entre octobre 2006 et novembre 2008. La spectroscopie visible a été réalisée avec les deux instruments FORS (FORS1 jusqu'en septembre 2007, FORS2 plus tard), pour l'infrarouge ISAAC (grille J) et SINFONI (grille $H + K$) ont été utilisés.

Il a été obtenu 31 spectres visibles (Fig. 4.1) pour 28 corps (6 "classical", 5 "resonant", 5 "scattered" , 2 "detached", et 10 Centaures), dont 15 ont été spectroscopiquement observés pour la première fois (Fornasier et al. 2009).

Nous avons trouvé que le spectre visible du TNO (208996) 2003 AZ_{84}, acquis en novembre 2008, apparaît sans caractéristiques (Fig. 4.2), alors qu'une faible bande attribuée à la présence de silicates hydratés, centrée autour de 0.7 μm, avait été identifiée sur un spectre acquis en janvier 2007 (Alvarez-Candal et al. 2008) et dans un précédent travail par Fornasier et al. (2004), en suggerant une surface hétérogène.

Pour une meilleure analyse de la distribution de la pente spectrale dans le visible, toutes les mesures disponibles dans la littérature ont été prises en compte (Fornasier et al. 2009, et références), pour un échantillon total de 20 Centaures et 53 TNOs (14 "resonant", 29 "classical", 6 "scattered", et 4 "detached"). Toutes les populations montrent un comportement similaire de ce point de vue, sauf que l'absence d'objets très rouges est évidente chez les TNOs classiques (Fig. 4.3 et Table 4.1). Cependant les observations peuvent être biaisées, en raison de la taille moyenne plus petite de la population froide (rouge) par rapport à la population chaude (plus bleu) dans la ceinture classique.

Des corrélations possibles ont été recherchées entre les valeurs de la pente spectrale et les éléments orbitaux (inclinaison, excentricité, demi-grand-axe, et aphélie) ou la magnitude absolue H pour les différentes classes dynamiques (Fig. 4.4). La corrélation la plus forte a été trouvée pour les "scattered TNOs", qui montrent des valeurs plus faibles de la pente avec l'excentricité qui augmente. Avec cette étude, il a été possible d'appuyer la suggestion faite par Peixinho et al. (2004) que la population des Centaures pourrait provenir des "Plutinos", et non des "scattered TNOs".

Sur la base des spectres visible et proche infrarouge, la composition de surface des TNOs et des Centaures a été modélisée en utilisant les formulations de transfert radiatif par Hapke (1981, 1993) et Shkuratov et al. (1999). Dans cette thèse, je fais un compte-rendu sur le cas de (50000) Quaoar. Les résultats obtenus (Table 4.3 et Fig. 4.5) ont permis de mettre des contraintes fortes sur la composition de la surface de cet objet, l'un des plus grands TNOs : de façon inattendue l'azote moléculaire a été trouvé en concentration importante ($\sim$ 20 %), tandis que la présence d'une fine couche de glace d'eau amorphe couvrant le mélange des autres composants a été jugée plausible. La modélisation des six objets supplémentaires est actuellement en cours.

Couleurs et taxonomie

Au cours de l'ESO-LP, des mesures photométriques dans le visible ($BVRI$, avec FORS1 et FORS 2) et le proche infrarouge (JHK_S, avec ISAAC) ont été obtenues pour 45 objets, 19 d'entre eux ont leurs couleurs rapportées

pour la première fois. Les Tables 4.5 et 4.6 présentent la liste des magnitudes calculées, y compris la magnitude absolue H.

Sur la base des indices de couleur obtenus, la classification taxonomique (Barucci et al. 2005a) des objets a été dérivée (Table 4.7) en utilisant la technique du "G-mode", présentée dans Fulchignoni et al. (2000).

Trois objets n'entrent dans aucune catégorie de la taxonomie. Ce fait, ainsi que la présence de plusieurs classifications multiples, pourrait appuyer l'idée que d'autres groupes pourraient être trouvés avec le nombre des objets analysés qui augmente, conduisant à un affinement de la taxonomie actuelle.

En comparant avec des travaux précédents, des indications de surfaces hétérogènes ont été trouvées pour sept objets (Chariklo, Sedna, Ixion, Thereus, 2005 RM_{43}, 2005 RR_{43}, 1999 DE_9).

En prenant en compte l'ensemble des 151 Centaures et TNOs dont la taxonomie existe, la répartition des taxons en fonction des propriétés dynamiques a été étudiée (Figs. 4.9, 4.10, et 4.11). Les Centaures manifestent clairement leur bimodalité de couleur (BR, RR) déjà connue; les types IR sont concentrés dans les classes dynamiques classique et résonant, alors que les types RR dominent les TNOs classiques. Les classes BR et RR dominent la population avec demi-grand-axe jusqu'à $\sim$ 30 UA, tandis que tous les quatre taxons sont bien représentés à plus grande distance du Soleil. Les classes RR et BB sont plus abondantes à basse et à forte inclinaison orbitale, respectivement, ce qui associe ces objets avec les populations dynamiques "froide" et "chaude".

Courbes de lumière et densités

Afin d'accroître l'échantillon assez limité de Centaures et TNOs avec propriétés de rotation connues (quelques dizaines d'objets, pour une revue voir Sheppard et al. 2008), dans le cadre de l'ESO-LP j'ai mené deux observations (3 nuits chacune) à l'ESO-NTT en avril 2007 et décembre 2007. Les observations ont été effectuées avec l'instrument EMMI, en bande R, en obtenant des données sur 12 objets (Figs. 4.12 et 4.13).

Une analyse de Fourier des courbes de lumière a été réalisée suivant la méthode développée par Harris et al. (1989a). Pour 9 des 12 TNO observés, la période de rotation synodique a été obtenue (Figs. 4.14-4.22), alors que la qualité des données des 3 objets restant (Typhon, 2003 FY_{128}, et 2003 UZ_{117}) n'était pas suffisante pour trouver une solution sans équivoque. De cette étude ressort la rotation rapide de 2003 UZ_{413}, qui apparait être le deuxième TNO le plus rapide après (136108) Haumea. Une limite inférieure pour le rapport des axes a/b a été obtenue à partir de l'équation 1.10, alors que les estimations de densité ont été obtenues comme décrit dans la section 1.4.3 (Table 4.10).

J'ai étudié la relation entre la taille et la densité proposée par Sheppard et al. (2008) (chapitre 1), sur la base des résultats présentés dans cette thèse. Cette relation pourrait être considérée comme statistiquement significative, mais l'échantillon est limité, et la présence d'objets de magnitude absolue similaire mais de densités estimées complètement différentes empêche l'évaluation de sa validité. L'augmentation de l'échantillon de mesures fiables de l'albédo (pour réduire l'ambiguïté entre la luminosité et la taille) et des estimations de la densité semblent être nécessaires pour enquêter sur l'existence d'une telle relation. En outre, l'hypothèse fluide parfait (bien que raisonnable compte tenu des connaissances actuelles sur la nature physique de ces corps) doit être remplacée par un tableau plus complexe, y compris les tensions internes.

Conclusions

Dans le cadre de mon travail de thèse, j'ai étudié les astéroïdes cibles de la mission spatiale Rosetta, (2867) Steins et (21) Lutetia, et les petits corps du Système Solaire externe (Centaures et Objets transneptuniens).

Les résultats obtenus pour Steins et Lutetia, avant leur survol par Rosetta, ont fourni une base fondamentale pour l'étalonnage, l'analyse, et l'interprétation de l'imagerie et des données spectroscopiques acquises (ou qui seront acquises) par les instruments VIRTIS et OSIRIS à bord de la sonde.

Un important corpus de données physiques sur les Centaures et les TNOs a été présenté. En particulier, cet ensemble de données comprend des spectres et des couleurs photométriques, dans le domaines du visible et du proche infrarouge, qui ont été utilisés pour déduire des informations sur les propriétés des surfaces des objets observés, à la recherche aussi d'éventuelles corrélations avec les différents types dynamiques. En outre, l'analyse des courbes de lumière de 12 objets a permir d'obtenir des informations sur leur rotation, forme, et densité.

Bibliography

Albarède, F. 2009, Nature, 461, 1227

Alvarez-Candal, A., Fornasier, S., Barucci, M. A., de Bergh, C., & Merlin, F. 2008, Astronomy & Astrophysics, 487, 741

Andronico, G., Baratta, G. A., Spinella, F., & Strazzulla, G. 1987, Astronomy & Astrophysics, 184, 333

Barkume, K. M., Brown, M. E., & Schaller, E. L. 2008, The Astronomical Journal, 135, 55

Barucci, M. A., Belskaya, I. N., Fulchignoni, M., & Birlan, M. 2005a, The Astronomical Journal, 130, 1291

Barucci, M. A., Brown, M. E., Emery, J. P., & Merlin, F. 2008a, in The Solar System Beyond Neptune, ed. Barucci, M. A., Boehnhardt, H., Cruikshank, D. P., & Morbidelli, A., 143–160

Barucci, M. A., Capria, M. T., Coradini, A., & Fulchignoni, M. 1987, Icarus, 72, 304

Barucci, M. A., Cruikshank, D. P., Dotto, E., et al. 2005b, Astronomy & Astrophysics, 439, L1

Barucci, M. A., Cruikshank, D. P., Mottola, S., & Lazzarin, M. 2002, in Asteroids III, ed. W. F. Bottke, P. Paolicchi, R. P. Binzel, & A. Cellino, 273–287

Barucci, M. A., Fornasier, S., Dotto, E., et al. 2008b, Astronomy & Astrophysics, 477, 665

Barucci, M. A., Fulchignoni, M., Fornasier, S., et al. 2005c, Astronomy & Astrophysics, 430, 313

Barucci, M. A., Merlin, F., Dotto, E., Doressoundiram, A., & de Bergh, C. 2006, Astronomy & Astrophysics, 455, 725

Bauer, J. M., Meech, K. J., Fernández, Y. R., et al. 2003, Icarus, 166, 195

Bell, J. F., Davis, D. R., Hartmann, W. K., & Gaffey, M. J. 1989, in Asteroids II, ed. R. P. Binzel, T. Gehrels, & M. S. Matthews, 921–945

Belskaya, I. N. & Lagerkvist, C. 1996, Planetary and Space Science, 44, 783

Belskaya, I. N. & Shevchenko, V. G. 1999, in Lunar and Planetary Institute Science Conference Abstracts, Vol. 30, 1374

Belskaya, I. N. & Shevchenko, V. G. 2000, Icarus, 147, 94

Belskaya, I. N., Shevchenko, V. G., Kiselev, N. N., et al. 2003, Icarus, 166, 276

Belton, M. J. S., Chapman, C. R., Klaasen, K. P., et al. 1996, Icarus, 120, 1

Belton, M. J. S., Veverka, J., Thomas, P., et al. 1992, Science, 257, 1647

Binzel, R. P., Bus, S. J., Burbine, T. H., & Sunshine, J. M. 1996, Science, 273, 946

Binzel, R. P., Farinella, P., Zappala, V., & Cellino, A. 1989, in Asteroids II, ed. R. P. Binzel, T. Gehrels, & M. S. Matthews, 416–441

Binzel, R. P., Rivkin, A. S., Stuart, J. S., et al. 2004, Icarus, 170, 259

Birlan, M., Barucci, M. A., Vernazza, P., et al. 2004, New Astronomy, 9, 343

Birlan, M., Vernazza, P., Fulchignoni, M., et al. 2006, Astronomy & Astrophysics, 454, 677

Bowell, E., Hapke, B., Domingue, D., et al. 1989, in Asteroids II, ed. R. P. Binzel, T. Gehrels, & M. S. Matthews, 524–556

Brown, M. E. 2001, The Astronomical Journal, 121, 2804

Brown, M. E., Barkume, K. M., Ragozzine, D., & Schaller, E. L. 2007, Nature, 446, 294

Brown, M. E. & Trujillo, C. A. 2004, The Astronomical Journal, 127, 2413

Brunetto, R. 2009, Earth Moon and Planets, 105, 249

Brunetto, R., Barucci, M. A., Dotto, E., & Strazzulla, G. 2006, The Astrophysical Journal, 644, 646

Brunetto, R. & Strazzulla, G. 2005, Icarus, 179, 265

Burbine, T. H. & Binzel, R. P. 2002, Icarus, 159, 468

Burbine, T. H., Cloutis, E. A., Bus, S. J., Meibom, A., & Binzel, R. P. 1998, in Bulletin of the American Astronomical Society, Vol. 30, 1025

Burns, R. G., Parkin, K. M., Loeffler, B. M., Leung, I. S., & Abu-Eid, R. M. 1976, in Lunar and Planetary Science Conference Proceedings, Vol. 7, 2561–2578

Bus, S. J. & Binzel, R. P. 2002a, Icarus, 158, 146

Bus, S. J. & Binzel, R. P. 2002b, Icarus, 158, 106

Carvano, J. M. 2008, Astronomy & Astrophysics, 486, 1031

Carvano, J. M., Barucci, M. A., Delbó, M., et al. 2008, Astronomy & Astrophysics, 479, 241

Cellino, A., Bus, S. J., Doressoundiram, A., & Lazzaro, D. 2002, in Asteroids III, ed. W. F. Bottke, P. Paolicchi, R. P. Binzel, & A. Cellino, 633–643

Cellino, A., Hutton, R. G., di Martino, M., et al. 2005, Icarus, 179, 304

Cellino, A., Hutton, R. G., Tedesco, E. F., di Martino, M., & Brunini, A. 1999a, Icarus, 138, 129

Cellino, A., Michel, P., Tanga, P., et al. 1999b, Icarus, 141, 79

Chandrasekhar, S. 1987, Ellipsoidal figures of equilibrium, ed. Dover (New York)

Chapman, C. R. 2004, Annual Review of Earth and Planetary Sciences, 32, 539

Chapman, C. R., Merline, W. J., Thomas, P. C., et al. 2002, Icarus, 155, 104

Chapman, C. R., Morrison, D., & Zellner, B. 1975, Icarus, 25, 104

Chapman, C. R., Veverka, J., Belton, M. J. S., Neukum, G., & Morrison, D. 1996, Icarus, 120, 231

Cheng, A. F. 2004, Advances in Space Research, 33, 1558

Clark, B. E., Bus, S. J., Rivkin, A. S., et al. 2004, Journal of Geophysical Research (Planets), 109, E02001

Clark, R. N. & Lucey, P. G. 1984, Journal of Geophysical Research, 89, 6341

Conel, J. E. & Nash, D. B. 1970, Geochimica et Cosmochimica Acta Supplement, 1, 2013

Coradini, A., Fulchignoni, M., Fanucci, O., & Gavrishin, A. 1977, Computers & Geosciences, 3, 85

Cruikshank, D. P., Dalle Ore, C. M., Roush, T. L., et al. 2001, Icarus, 153, 348

Cruikshank, D. P., Imanaka, H., & Dalle Ore, C. M. 2005, Advances in Space Research, 36, 178

Dalle Ore, C. M., Barucci, M. A., Emery, J. P., et al. 2009, Astronomy & Astrophysics, 501, 349

Davis, D. R., Chapman, C. R., Durda, D. D., Farinella, P., & Marzari, F. 1996, Icarus, 120, 220

Davis, D. R. & Farinella, P. 1997, Icarus, 125, 50

de Bergh, C., Boehnhardt, H., Barucci, M. A., et al. 2004, Astronomy & Astrophysics, 416, 791

Delsanti, A. & Jewitt, D. 2006, in Solar System Update, ed. J. Blondel, P. & Mason (Springer), 267–294

Delsanti, A., Peixinho, N., Boehnhardt, H., et al. 2006, The Astronomical Journal, 131, 1851

DeMeo, F. & Binzel, R. P. 2008, Icarus, 194, 436

DeMeo, F. E., Binzel, R. P., Slivan, S. M., & Bus, S. J. 2009a, Icarus, 202, 160

DeMeo, F. E., Fornasier, S., Barucci, M. A., et al. 2009b, Astronomy & Astrophysics, 493, 283

Descamps, P. & Marchis, F. 2008, Icarus, 193, 74

Doressoundiram, A., Barucci, M. A., Fulchignoni, M., & Florczak, M. 1998, Icarus, 131, 15

Doressoundiram, A., Boehnhardt, H., Tegler, S. C., & Trujillo, C. 2008, in The Solar System Beyond Neptune, ed. Barucci, M. A., Boehnhardt, H., Cruikshank, D. P., & Morbidelli, A. , 91–104

Doressoundiram, A., Peixinho, N., de Bergh, C., et al. 2002, The Astronomical Journal, 124, 2279

Doressoundiram, A., Peixinho, N., Doucet, C., et al. 2005, Icarus, 174, 90

Doressoundiram, A., Peixinho, N., Moullet, A., et al. 2007, The Astronomical Journal, 134, 2186

Doressoundiram, A., Tozzi, G. P., Barucci, M. A., et al. 2003, The Astronomical Journal, 125, 2721

Dotto, E., Barucci, M. A., Boehnhardt, H., et al. 2003, Icarus, 162, 408

Dotto, E., Fornasier, S., Barucci, M. A., et al. 2006, Icarus, 183, 420

Dotto, E., Perna, D., Barucci, M. A., et al. 2008, Astronomy & Astrophysics, 490, 829

Dotto, E., Perna, D., Fornasier, S., et al. 2009, Astronomy & Astrophysics, 494, L29

Durda, D. D. & Stern, S. A. 2000, Icarus, 145, 220

Farinella, P., Milani, A., Nobili, A. M., & Valsecchi, G. B. 1980, Icarus, 44, 810

Farinella, P., Paolicchi, P., & Zappala, V. 1982, Icarus, 52, 409

Farnham, T. L. & Davies, J. K. 2003, Icarus, 164, 418

Fornasier, S., Barucci, M. A., de Bergh, C., et al. 2009, Astronomy & Astrophysics, 508, 457

Fornasier, S., Belskaya, I., Fulchignoni, M., Barucci, M. A., & Barbieri, C. 2006, Astronomy & Astrophysics, 449, L9

Fornasier, S., Doressoundiram, A., Tozzi, G. P., et al. 2004, Astronomy & Astrophysics, 421, 353

Fornasier, S., Marzari, F., Dotto, E., Barucci, M. A., & Migliorini, A. 2007, Astronomy & Astrophysics, 474, L29

Fornasier, S., Migliorini, A., Dotto, E., & Barucci, M. A. 2008, Icarus, 196, 119

Froeschle, C. & Morbidelli, A. 1994, in IAU Symposium, Vol. 160, Asteroids, Comets, Meteors 1993, ed. A. Milani, M. di Martino, & A. Cellino, 189–204

Fujiwara, A., Kawaguchi, J., Yeomans, D. K., et al. 2006, Science, 312, 1330

Fulchignoni, M., Belskaya, I., Barucci, M. A., de Sanctis, M. C., & Doressoundiram, A. 2008, in The Solar System Beyond Neptune, ed. Barucci, M. A., Boehnhardt, H., Cruikshank, D. P., & Morbidelli, A., 181–192

Fulchignoni, M., Birlan, M., & Antonietta Barucci, M. 2000, Icarus, 146, 204

Gaffey, M. J. 1999, in Lunar and Planetary Institute Science Conference Abstracts, Vol. 30, 1375

Gaffey, M. J., Burbine, T. H., & Binzel, R. P. 1993, Meteoritics, 28, 161

Gaffey, M. J., Cloutis, E. A., Kelley, M. S., & Reed, K. L. 2002, in Asteroids III, ed. W. F. Bottke, P. Paolicchi, R. P. Binzel, & A. Cellino, 183–204

Gaffey, M. J. & Gilbert, S. L. 1998, Meteoritics and Planetary Science, 33, 1281

Gaffey, M. J. & Kelley, M. S. 2004, in Lunar and Planetary Institute Science Conference Abstracts, Vol. 35, 1812

Gaudi, B. S., Stanek, K. Z., Hartman, J. D., Holman, M. J., & McLeod, B. A. 2005, The Astrophysical Journal Letters, 629, L49

Gladman, B., Marsden, B. G., & Vanlaerhoven, C. 2008, in The Solar System Beyond Neptune, ed. Barucci, M. A., Boehnhardt, H., Cruikshank, D. P., & Morbidelli, A., 43–57

Gomes, R., Levison, H. F., Tsiganis, K., & Morbidelli, A. 2005, Nature, 435, 466

Gomes, R. S. 2003, Icarus, 161, 404

Gradie, J. C., Chapman, C. R., & Tedesco, E. F. 1989, in Asteroids II, ed. R. P. Binzel, T. Gehrels, & M. S. Matthews, 316–335

Green, J. R., Brown, R. H., Cruikshank, D. P., & Anicich, V. 1991, in Bulletin of the American Astronomical Society, Vol. 23, 1208

Grundy, W. M. & Schmitt, B. 1998, Journal of Geophysical Research, 103, 25809

Grundy, W. M., Schmitt, B., & Quirico, E. 2002, Icarus, 155, 486

Grundy, W. M., Stansberry, J. A., Noll, K. S., et al. 2007, Icarus, 191, 286

Guilbert, A., Barucci, M. A., Brunetto, R., et al. 2009, Astronomy & Astrophysics, 501, 777

Hapke, B. 1981, Journal of Geophysical Research, 86, 3039

Hapke, B. 1993, Theory of reflectance and emittance spectroscopy, ed. Cambridge University Press (Cambridge, UK)

Harris, A. W., Young, J. W., Bowell, E., et al. 1989a, Icarus, 77, 171

Harris, A. W., Young, J. W., Contreiras, L., et al. 1989b, Icarus, 81, 365

Hawarden, T. G., Leggett, S. K., Letawsky, M. B., Ballantyne, D. R., & Casali, M. M. 2001, Royal Astronomical Society, Monthly Notices, 325, 563

Hazen, R. M., Bell, P. M., & Mao, H. K. 1978, in Lunar and Planetary Science Conference Proceedings, Vol. 9, 2919–2934

Hicks, M. D., Bauer, J. M., & Tokunaga, A. T. 2004, IAU Circular, 8315, 3

Hiroi, T., Vilas, F., & Sunshine, J. M. 1996, Icarus, 119, 202

Holsapple, K. A. 2001, Icarus, 154, 432

Holsapple, K. A. 2004, Icarus, 172, 272

Holsapple, K. A. 2007, Icarus, 187, 500

Horner, J., Evans, N. W., & Bailey, M. E. 2004, Royal Astronomical Society, Monthly Notices, 354, 798

Howell, E. S., Merenyi, E., & Lebofsky, L. A. 1994, Journal of Geophysical Research, 99, 10847

Hsieh, H. H. & Jewitt, D. 2006, Science, 312, 561

Hsieh, H. H., Jewitt, D. C., & Fernández, Y. R. 2004, The Astronomical Journal, 127, 2997

Hudgins, D. M., Sandford, S. A., Allamandola, L. J., & Tielens, A. G. G. M. 1993, The Astrophysical Journal Supplement Series, 86, 713

Imanaka, H., Khare, B. N., McKay, C. P., & Cruikshank, D. P. 2005, in Bulletin of the American Astronomical Society, Vol. 37, 772

Ishiguro, M., Hiroi, T., Tholen, D. J., et al. 2007, Meteoritics and Planetary Science, 42, 1791

Jeans, J. H. 1919, Problems of cosmogony and stellar dynamics, ed. Cambridge University Press (Cambridge, UK)

Jewitt, D. & Luu, J. 1993, Nature, 362, 730

Jewitt, D., Luu, J., & Marsden, B. G. 1992, IAU Circular 5611

Jewitt, D., Yang, B., & Haghighipour, N. 2009, The Astronomical Journal, 137, 4313

Jewitt, D. C. & Luu, J. 2004, Nature, 432, 731

Jewitt, D. C. & Luu, J. X. 2001, The Astronomical Journal, 122, 2099

Jewitt, D. C. & Sheppard, S. S. 2002, The Astronomical Journal, 123, 2110

Jones, T. D., Lebofsky, L. A., Lewis, J. S., & Marley, M. S. 1990, Icarus, 88, 172

Jorda, L., Lamy, P. L., Faury, G., et al. 2008, Astronomy & Astrophysics, 487, 1171

Keller, H. U., Coradini, A., Barbieri, C., et al. 2009, in Bulletin of the American Astronomical Society, Vol. 41, 564

Kerridge, J. F. & Bunch, T. E. 1979, in Asteroids, ed. Gehrels, T., 745–764

Khare, B. N., Sagan, C., Heinrich, M., et al. 1994, in Bulletin of the American Astronomical Society, Vol. 26, 1176

Küppers, M., Fornasier, S., Schroder, S., et al. 2009, in AAS/Division for Planetary Sciences Meeting Abstracts, Vol. 41, 59.04

Küppers, M., Mottola, S., Lowry, S. C., et al. 2007, Astronomy & Astrophysics, 462, L13

Lamy, P. L., Jorda, L., Fornasier, S., et al. 2008a, Astronomy & Astrophysics, 487, 1187

Lamy, P. L., Kaasalainen, M., Lowry, S., et al. 2008b, Astronomy & Astrophysics, 487, 1179

Landolt, A. U. 1992, The Astronomical Journal, 104, 340

Lazzarin, M., Marchi, S., Magrin, S., & Barbieri, C. 2004, Astronomy & Astrophysics, 425, L25

Lazzarin, M., Marchi, S., Moroz, L. V., & Magrin, S. 2009, Astronomy & Astrophysics, 498, 307

Levison, H. F. & Duncan, M. J. 1997, Icarus, 127, 13

Levison, H. F. & Stern, S. A. 2001, The Astronomical Journal, 121, 1730

Luu, J. X. & Jewitt, D. C. 2002, Annu. Rev. Astron. Astrophys., 40, 63

Magni, G., Coradini, A., Cerroni, P., & Federico, C. 1990, Advances in Space Research, 10, 145

Magri, C., Ostro, S. J., Rosema, K. D., et al. 1999, Icarus, 140, 379

Mastrapa, R. M. E. & Sandford, S. A. 2008, in Bulletin of the American Astronomical Society, Vol. 40, 496

McBride, N., Green, S. F., Davies, J. K., et al. 2003, Icarus, 161, 501

McKinnon, W. B. 1991, Nature, 354, 431

Merlin, F., Barucci, M. A., de Bergh, C., et al. 2010, Submitted to Icarus

Merlin, F., Barucci, M. A., Dotto, E., de Bergh, C., & Lo Curto, G. 2005, Astronomy & Astrophysics, 444, 977

Migliorini, F., Manara, A., Scaltriti, F., et al. 1997, Icarus, 128, 104

Morbidelli, A., Bottke, Jr., W. F., Froeschlé, C., & Michel, P. 2002, in Asteroids III, ed. W. F. Bottke, P. Paolicchi, R. P. Binzel, & A. Cellino, 409–422

Morbidelli, A., Chambers, J., Lunine, J. I., et al. 2000, Meteoritics and Planetary Science, 35, 1309

Morbidelli, A., Levison, H. F., & Gomes, R. 2008, in The Solar System Beyond Neptune, ed. Barucci, M. A., Boehnhardt, H., Cruikshank, D. P., & Morbidelli, A., 275–292

Morbidelli, A., Levison, H. F., Tsiganis, K., & Gomes, R. 2005, Nature, 435, 462

Moroz, L., Baratta, G., Strazzulla, G., et al. 2004, Icarus, 170, 214

Mothé-Diniz, T. & Carvano, J. M. 2005, Astronomy & Astrophysics, 442, 727

Moullet, A., Lellouch, E., Doressoundiram, A., et al. 2008, Astronomy & Astrophysics, 483, L17

Mueller, M., Harris, A. W., Bus, S. J., et al. 2006, Astronomy & Astrophysics, 447, 1153

Nelder, J. A. & Mead, R. 1965, Computer Journal, 7, 308

Nesvorný, D. & Morbidelli, A. 1998, Celestial Mechanics and Dynamical Astronomy, 71, 243

Nicholson, P. D., Cuk, M., Sheppard, S. S., Nesvorny, D., & Johnson, T. V. 2008, in The Solar System Beyond Neptune, ed. Barucci, M. A., Boehnhardt, H., Cruikshank, D. P., & Morbidelli, A. , 411–424

Noll, K. S., Levison, H. F., Grundy, W. M., & Stephens, D. C. 2006, Icarus, 184, 611

Ortiz, J. L., Baumont, S., Gutiérrez, P. J., & Roos-Serote, M. 2002, Astronomy & Astrophysics, 388, 661

Ortiz, J. L., Gutiérrez, P. J., Casanova, V., & Sota, A. 2003, Astronomy & Astrophysics, 407, 1149

Peixinho, N., Boehnhardt, H., Belskaya, I., et al. 2004, Icarus, 170, 153

Peixinho, N., Doressoundiram, A., Delsanti, A., et al. 2003, Astronomy & Astrophysics, 410, L29

Peixinho, N., Lacerda, P., & Jewitt, D. 2008, The Astronomical Journal, 136, 1837

Perna, D., Barucci, M. A., Fornasier, S., et al. 2010a, Astronomy & Astrophysics, 510, A53

Perna, D., Dotto, E., Barucci, M. A., et al. 2009, Astronomy & Astrophysics, 508, 451

Perna, D., Dotto, E., Lazzarin, M., et al. 2010b, Submitted to Astronomy & Astrophysics

Perron, C. & Zanda, B. 2005, Comptes Rendus Physique, 6, 345

Persson, S. E., Murphy, D. C., Krzeminski, W., Roth, M., & Rieke, M. J. 1998, The Astronomical Journal, 116, 2475

Poulet, F., Cuzzi, J. N., Cruikshank, D. P., Roush, T., & Dalle Ore, C. M. 2002, Icarus, 160, 313

Pravec, P. & Harris, A. W. 2000, Icarus, 148, 12

Rabinowitz, D. L., Barkume, K., Brown, M. E., et al. 2006, The Astrophysical Journal, 639, 1238

Rivkin, A. S., Binzel, R. P., & Bus, S. J. 2005, Icarus, 175, 175

Rivkin, A. S., Howell, E. S., Lebofsky, L. A., Clark, B. E., & Britt, D. T. 2000, Icarus, 145, 351

Rivkin, A. S., Howell, E. S., Vilas, F., & Lebofsky, L. A. 2002, in Asteroids III, ed. W. F. Bottke, P. Paolicchi, R. P. Binzel, & A. Cellino, 235–253

Roush, T. L. & Cruikshank, D. P. 2004, in Astrobiology: Future Perspectives, ed. Ehrenfreund, P., Irvine, W. M., Owen, T., Becker, L., Blank, J., Brucato, J. R., Colangeli, L., Derenne, S., Dutrey, A., Despois, D., Lazcano, A., & Robert, F., 149

Safronov, V. S. 1979, in Asteroids, ed. Gehrels, T., 975–991

Santos-Sanz, P., Ortiz, J. L., Barrera, L., & Boehnhardt, H. 2009, Astronomy & Astrophysics, 494, 693

Schaller, E. L. & Brown, M. E. 2007a, The Astrophysical Journal Letters, 670, L49

Schaller, E. L. & Brown, M. E. 2007b, The Astrophysical Journal Letters, 659, L61

Sheppard, S. S. & Jewitt, D. C. 2002, The Astronomical Journal, 124, 1757

Sheppard, S. S. & Jewitt, D. C. 2003, Earth Moon and Planets, 92, 207

Sheppard, S. S., Lacerda, P., & Ortiz, J. L. 2008, in The Solar System Beyond Neptune, ed. Barucci, M. A., Boehnhardt, H., Cruikshank, D. P., & Morbidelli, A., 129–142

Shkuratov, Y., Starukhina, L., Hoffmann, H., & Arnold, G. 1999, Icarus, 137, 235

Shkuratov, Y. G. & Helfenstein, P. 2001, Icarus, 152, 96

Spearman, C. 1904, American Journal of Psychology, 15, 72

Stansberry, J., Grundy, W., Brown, M., et al. 2008, in The Solar System Beyond Neptune, ed. Barucci, M. A., Boehnhardt, H., Cruikshank, D. P., & Morbidelli, A. , 161–179

Stooke, P. J. 1996, Earth Moon and Planets, 74, 131

Strazzulla, G., Dotto, E., Binzel, R., et al. 2005, Icarus, 174, 31

Taylor, J. R. 1997, An introduction to error analysis - 2nd edition, ed. University Science Book (Sausalito, California)

Tedesco, E. F. 1989, in Asteroids II, ed. R. P. Binzel, T. Gehrels, & M. S. Matthews, 1090–1138

Tedesco, E. F., Veeder, G. J., Fowler, J. W., & Chillemi, J. R. 1992, The IRAS Minor Planet Survey, Tech. rep.

Tegler, S. C., Bauer, J. M., Romanishin, W., & Peixinho, N. 2008, in The Solar System Beyond Neptune, ed. Barucci, M. A., Boehnhardt, H., Cruikshank, D. P., & Morbidelli, A. , 105–114

Tholen, D. J. 1984, PhD thesis, (Arizona Univ., Tucson.)

Tholen, D. J. 1989, in Asteroids II, ed. R. P. Binzel, T. Gehrels, & M. S. Matthews, 1139–1150

Torppa, J., Kaasalainen, M., Michalowski, T., et al. 2003, Icarus, 164, 346

Trombka, J. I., Squyres, S. W., Brückner, J., et al. 2000, Science, 289, 2101

Tsiganis, K., Gomes, R., Morbidelli, A., & Levison, H. F. 2005, Nature, 435, 459

Vernazza, P., Brunetto, R., Binzel, R. P., et al. 2009, Icarus, 202, 477

Vilas, F., Jarvis, K. S., & Gaffey, M. J. 1994, Icarus, 109, 274

Warner, B. D. 2004, Minor Planet Bulletin, 31, 67

Weissman, P. R., Lowry, S. C., & Choi, Y. 2007, Astronomy & Astrophysics, 466, 737

Wisdom, J. 1983, Icarus, 56, 51

Wisdom, J. 1987, Icarus, 72, 241

Yeomans, D. K., Barriot, J., Dunham, D. W., et al. 1997, Science, 278, 2106

Zappala, V., di Martino, M., Knezevic, Z., & Djurasevic, G. 1984, Astronomy & Astrophysics, 130, 208

Zellner, B., Tholen, D. J., & Tedesco, E. F. 1985, Icarus, 61, 355